A Spatial Analysis of the Nansen Ice Shelf Basal Channel, Using Ice Penetrating Radar

by

Peter Leslie Danylo Wray

A thesis
presented to the University of Waterloo
in fulfilment of the
thesis requirement for the degree of
Master of Science
in
Geography and Environmental Management

Waterloo, Ontario, Canada, 2019

Author's declaration

I hereby declare that I am the sole author of this thesis. This is a true copy of the thesis, including any required final revisions, as accepted by my examiners.

I understand that my thesis may be made electronically available to the public.

Abstract

The stability of floating ice shelves in the Antarctic is of great concern as their current thinning and future collapse will release mass from grounded ice sheets into the ocean, contributing to sea level rise. The study of sub-ice shelf environments is essential for understanding ice-ocean interactions, where warming ocean temperatures have already begun to reduce the mass of Antarctic ice shelves through enhanced melt. Obtaining direct measurements of the sub-ice shelf cavity remains challenging. This thesis demonstrates that ground-based and airborne Ice Penetrating Radar (IPR) can deliver high resolution geospatial data of sub-ice shelf features, which can be used to observe: ice draft and surface morphology, vertical melt rates, and hydrostatic balance of the ice shelf.

In November 2016 and January/February 2017, IPR surveys were completed over the Nansen Ice Shelf in Terra Nova Bay, Antarctica. Surveys examined an ocean-sourced basal channel incised into the bottom of the ice shelf. Results reveal a 6 - 10 km wide, 90 m high basal channel, with 20 m high sub-channels. Data from 2011 and 2014 airborne IPR surveys are compared to the November 2016 ground based IPR to calculate a dozen direct measurements of vertical melt rate values within the channel. Melt was focused more on one channel flank, away from the channel center in local apexes. Many of the detected features were not in hydrostatic equilibrium as calculated from surface elevations, indicating the need for more radar determined ice thickness measurements to fully characterize basal channel morphology and monitor future melt.

Acknowledgments

I would like to first and foremost thank my supervisor, Dr. Christine Dow for the help she provided with this project and thesis during my M.Sc. I received much assistance from Christine with direction, processing and exploring the data in this project as well as many helpful edits and suggestions during the writing of this thesis. Secondly I would like to thank Dr. Derek Mueller for his countless edits, guidance and advice. Together Christine and Derek funded, planned and collected the ground-based radar data during the 2016 Antarctic field season that started this project. They both also provided me with invaluable field assistant opportunities in the Canadian Arctic and the Kluane Icecap. In addition, I would like to thank the collaborators at the University of Texas Institute for Geophysics for collecting and providing me with the airborne data as well as facilitating my travel and accommodations in Austin Texas, where I was able to process and use their radar data.

Financial and logistical support for both Antarctic field seasons was provided by Dr. Won Sang, and the Korean Polar Research Institute, and I gratefully acknowledge their support.

Many people have assisted in the completion of this thesis. In particular, I had several very helpful conversations with Dr. Stefan Jendersie, Dr. Tony Endres, and Chad Greene during this project. In addition, Don Blankenship, Jamin Greenbaum, Duncan Young, and Gregory Ng, all contributed useful discussions and/or help with this project.

I would also like to thank my Committee: Dr. Chris Fletcher, Dr. Tony Endres, and Dr. Derek Mueller for taking the time to review this document.

Dedication

This thesis is dedicated to all of my friends who surrounded me over the last two and a half years. From the Crawfords, to the Winchester family, and those who lent me rooms to stay in during the last few months of my degree, the camping crew, to all the GEMs and the Environment graduate students at large: thanks you for the support and company in all the times I was not working on my studies. Without all the other aspects of my life, which my friends constitute, I surely would have never finished this work.

Table of Contents

List of Figures

List of Abbreviations

CDW – Circumpolar Deep Water

DEM – Digital Elevation Model

DIT – Drygalski Ice Tongue

DITM – Digital Ice Thickness Model

EAIS – Eastern Antarctic Ice Shelf

EPU – Embedded Processing Unit

GIMBL - Geophysical Investigations of Marie Byrd Land

Go-LIVE – Global Land Ice Velocity Extraction

GPR – Ground Penetrating Radar

GPS – Global Positioning System

HDF – Hierarchical Data Format

HE – Hydrostatic Equilibrium

ICECAP - International Collaborative Exploration of the Cryosphere through Aerogeophysical Profiling

IPR – Ice Penetrating Radar

KOPRI – Korean Polar Research Institute

MMR – Meteoric Marine-ice Reflection

NIS – Nansen Ice Shelf

OTL – Ocean Tidal Loading

PIG – Pine Island Glacier

PPP – Precise Point Positioning

PSU – Practical Salinity Unit

RES – Radio Echo Sounding

Rx – Receiver Antenna

Tx – Transmitter Antenna

UTIG – University of Texas Institute for Geophysics

VLCC- Victoria Land Coastal Current

WAIS – Western Antarctic Ice Sheet

List of Symbols

B	Magnetic induction or flux density	Wb m^{-2}
E	Electric field intensity	V m^{-1}
HB	Hydrostatic balance	m
M	Vertical melt	m
R	Reflection Coefficient	unitless
S	Surface elevation	m (above GL04C)
T	Ice thickness	m
V	Surface ice velocity	m a^{-1}
du	Velocity change in principle x axis	m a^{-1}
dv	Velocity change in principle y axis	m a^{-1}
c	Speed of light in a vaccum	3.00 x10^{8} m s^{-1}
e_{ID}	Greatest possible error of ice draft	|m|
e_{geoid}	Large scale error of GL04C geoid	|m|
e_{SM}	Greatest possible error of ice draft	|m|
e_{TM}	Greatest possible error of ice thickness	|m|
e_{TR}	Greatest possible error from measured tidal range	|m|
$e_{\Delta T}$	Greatest possible error of ice thickness difference	|m|
i	Imaginary phase component of radar wave	unitless
k	Dielectric constant	unitless

f	Electromagnetic field frequency	Hz
t_x	Two-way travel time	s
t_0	Zero-offset travel time	s
v	Wave velocity	m s^{-1}
x	Antennae offset	m
ε	Dielectric permittivity	F m^{-1}
ε_0	Dielectric permittivity of a vacuum	8.8542 x 10^{-12} F m^{-1}
$\dot{\varepsilon}_1$	Net strain rate of ice	0
$\dot{\varepsilon}_{xx}$	Net strain in the principle x axis	unitless
$\dot{\varepsilon}_{yy}$	Net strain in the principle y axis	unitless
$\dot{\varepsilon}_{zz}$	Net strain in the principle z axis	unitless
μ	Magnetic permeability	H m^{-1}
π	Pi	3.14159
ρ_i	Glacial ice density	917 kg m^{-3}
ρ_{sw}	Sea water density	1025 kg m^{-3}
σ	Electric conductivity	S m^{-1}

Chapter 1

Introduction

1.1 Overview

Ice shelves currently play an important role in preventing large portions of the Antarctic Ice Sheet from destabilizing and discharging large volumes of ice into the ocean. An ice shelf is the floating portion of an ice sheet; they provide a crucial buttressing force, acting as retaining walls holding grounded ice mass on land, greatly slowing the flow of ice sheets into the ocean (Dupont and Alley, 2005). Reconstructions of sea level from 3-million-years ago when the Earth had similar CO_2 concentrations to present day, suggests that the Eastern Antarctic Ice Sheet (EAIS) could partially retreat and the Western Antarctic Ice Sheet (WAIS) could fully retreat by the year 2500 (Deconto and Pollard, 2016). The collapse of the WAIS alone is capable of generating 3.4 m of sea level rise over the next few hundred years (Pollard and Deconto, 2015). Trusel et al. (2015) indicated that after 2050, projected anthropogenic climate forcing will have significant impacts on the magnitude of Antarctic ice mass loss. Understanding the dynamic systems that affect the stability of ice sheets, and the ice shelves that help to hold them on land, is thus of great importance for more accurately predicting the rise of global sea level.

Glaciers transition into ice shelves when they flow over the grounding line and begin to float on ocean water (Cuffey and Paterson, 2011). Grounding lines on retrograde slopes (i.e., the glacier basin deepens up-glacier of the grounding line) have been theorized to be conditionally unstable and potentially susceptible to large scale break up (Weertman, 1974). When retrograde grounding lines retreat, they do so into deeper water and portions of previously grounded ice begin to float, which exacerbates the retreat of the grounding line into deeper water. Ice masses that exist in sub-sea level basins are termed marine-type ice sheets (Weertman, 1974) and rely on their respective ice shelves to maintain their ice thickness and protect their retrograde grounding lines from warming ocean conditions (Pollard and Deconto, 2015). The majority of the WAIS is a marine-type ice sheet and concern about its stability has driven research into ice shelf processes and their stability.

Ice shelves exist in a dynamic relationship with the surrounding environment and are susceptible to thinning, retreat and disintegration from contact with both the ocean and the atmosphere. It has been hypothesized that some critical ocean and atmospheric temperature thresholds likely exist, beyond which the majority of Antarctic ice shelves will no longer be stable (Trusel et al. 2015). The rapid nature of recent climate change could be outpacing the ability of the Antarctic ice shelves to arrive at a new equilibrium state as atmospheric temperatures continue to warm, ocean circulation dynamics shift, and mass balances changes around the continent such that the critical thermal limit of stability for some ice shelves may already be exceeded, and the limit for more ice shelves might be exceeded in the near future (Trusel et al. 2015).

Ice shelves discussed in this thesis are the classic ice shelves found around the coast of the Antarctic, which are different from ice-tongues found in Greenland, or sea-ice ice shelves found in the Arctic (Dowdeswell and Jeffries, 2017). Classic ice shelves are fed by grounded ice and expand laterally after crossing the grounding line to fill wide bays. Antarctic ice shelves are typically confined at their lateral boundaries by contact with land (Benn and Evans, 2014), fringe 61% of Antarctica’s coast (Bindschadler et al., 2011) and cover more than 1.561 million km^2 (Rignot et al. 2013; Figure 1.1). Ice shelves experience significant mass loss in three ways: calving at the ice shelf edge, basal melt underneath the ice shelf, and, to a lesser degree, surface ablation (Rignot et al., 2013).

Similar to an ice cube in a glass of water, the melting of an ice shelf does not raise sea level, as it has already displaced an equivalent mass of water upon entering the ocean (Scambos et al., 2004). For a regularly shaped ice mass, this displacement of water by ice is dictated by the ratio between solid and liquid water densities (~917 kg m^{-3} and 1025 kg m^{-3} in this thesis respectively). Based on the ratio of these densities, hydrostatic equilibrium is often assumed, where the height of floating ice above the water surface (surface elevation) is ~11% of the total ice thickness and ~89% of ice thickness remains below the sea level as ice draft.

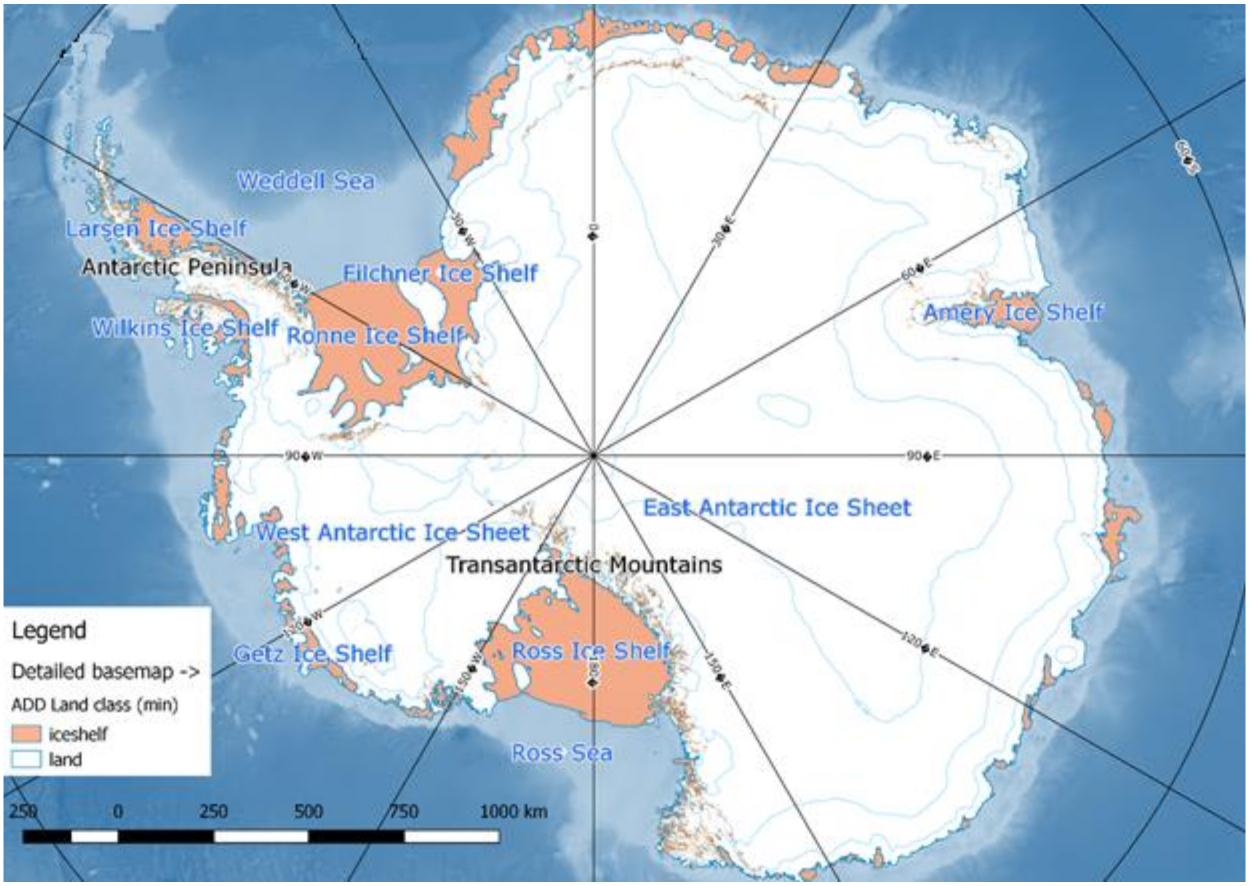

Figure 1.1: Map of the Antarctic showing the spatial extent of major ice shelves (in orange). Data from QGIS Quantarctica database.

The environment beneath ice shelves (hereafter called the ice shelf cavity), and specifically the interface of the ice draft topography and the ocean in the ice shelf cavity (where melting occurs) is inaccessible and difficult to observe. Radio Echo Sounding (RES) was one of the earliest methods used to examine the ice-ocean interface (Steenson, 1951). RES makes use of electromagnetic radiation in the radio frequency range through the use of transmitting and receiving antennas (hereafter Tx and Rx respectively). RES is also referred to as Ground Penetrating Radar (GPR), or in the case of glaciological investigations, Ice Penetrating Radar

(IPR). IPR utilizes the very low conductivity of glacial ice to penetrate through hundreds of metres of ice using frequencies ranging between 2-150 MHz (Arcone, 2009).

Processes at the ice-ocean interface are controlled by: water temperature and salinity, the shape of the ice shelf cavity, and ocean circulation (Holland and Jenkins, 1999). Warmer ocean water provides a greater heat flux to promote melting at depth, while the shape of the ice shelf cavity plays a large role in either sheltering or exposing ice shelves to warmer water, whereas ocean circulation dictates where warm water masses are delivered along the Antarctic coast. In the Amundsen Sea, for example, these factors all contribute to enhanced melt from upwelling warm currents, called Circumpolar Deep Water (CDW), which infiltrates underneath the ice shelves in that location, greatly increasing the available heat (Dutrieux et al., 2014). Increased heat delivery at the base of ice shelves is becoming more common as the ocean and atmosphere warms (Pritchard et al., 2012).

A common feature observed in the ice shelf cavity are inverted channels incised into the ice-ocean interface, called 'basal channels'. Basal channels appear to form when a source of relatively warm, upwelling water preferentially enhances vertical melt along a linear path over many kilometres (Rignot and Steffen, 2008) as illustrated in Figure 1.2. Documented basal channels range from 1-5 km wide, 50-250 m high, and 15 to upwards of 300 km long (Alley et al., 2016). Basal channels can exist parallel to one another on large ice shelves and cause topographical ice surface depressions as thinner ice subsides to maintain hydrostatic equilibrium

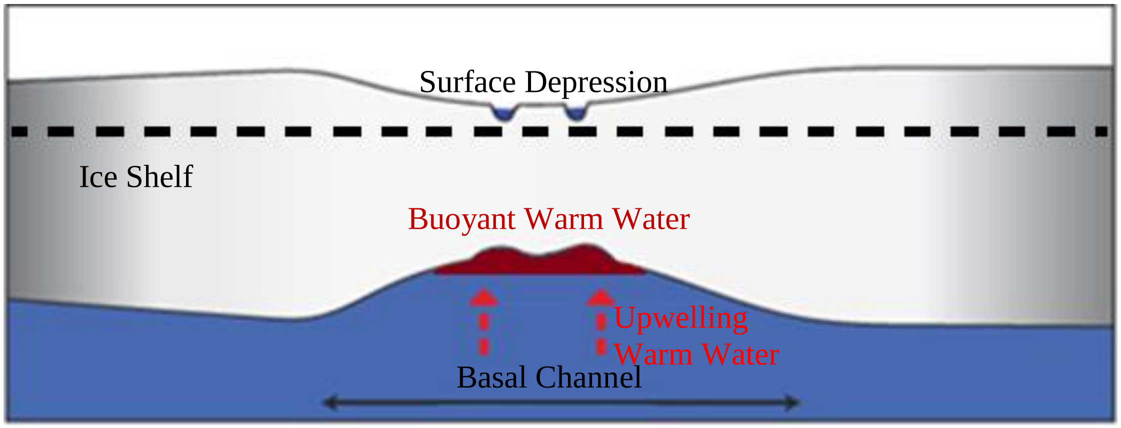

Figure 1.2: Simplified basal channel model showing a cross section of an ice shelf with a source of upwelling warm water leading to area of enhanced melt and a subsequent basal channel. The dashed line indicates sea level. Modified from Dow et al. (2018).

(Vaughan et al., 2012; Dow et al, 2018). Recent basal channel research has attempted to quantify: melt variations within basal channels and their growth over time (Gladish et al., 2012; Vaughan et al., 2012); the relationship between channel formation and ice shelf strain (Dow et al., 2018; Sergienko, 2013; Vaughan et al., 2012); and how well small scale basal channel features are represented through hydrostatic equilibrium (Drews, 2015; Dutriex et al., 2013; Gladish et al., 2012).

A possible basal channel was identified by a surface depression on the Nansen Ice Shelf (hereafter NIS) by Alley et al. (2016) and confirmed with preliminary radar surveys by Dow et al. (2018). The NIS is a small ice shelf with an area of ~1800 km^2. This ice shelf, which is located in Terra Nova Bay, Antarctica, is part of the Victoria Land Coast of the western Ross Sea and drains a portion of the EAIS. Recent studies of the NIS examined a surface river (Bell et al., 2017) that was observed flowing into a transverse crevasse located across the width of the basal channel, which subsequently widened until a 204 km^2 section of the ice shelf calved into Terra Nova Bay in April 2016 (Dow et al., 2018). The interaction between the surface river and the transverse crevasse over the NIS basal channel illustrated a previously undocumented interaction between basal channel enhanced melting, concentrated surface drainage formation, and large calving events over areas of relatively thin ice (Dow et al., 2018). The size and morphology of the NIS basal channel, its rate of growth, the effect the channel has on ice shelf strain rates, its hydrostatic balance, and its mechanism of formation constitutes current knowledge gaps in relation to the stability of the NIS that remains to be addressed

1.2 Research objectives

The objective of this research is to examine the NIS and its basal channel using airborne and ground-based IPR systems to contribute to the current understanding of how basal channels might affect the stability of an Antarctic ice shelf. In this thesis, ~1000 km of IPR are analysed to determine ice thickness and surface elevations across the NIS, which, combined with the Global Land Ice Velocity Extraction (Go-LIVE) database, are used to display, analyze and document the ice shelf and the basal channel present within it.

Specifically, the research objectives are to:

1. Create Digital Elevation and Digital Ice Thickness Models (DEM and DITM respectively) for the NIS
2. Describe the shape and size of the NIS basal channel
3. Determine the accuracy of hydrostatic equilibrium calculations for predicting the ice thickness of the NIS and its basal channel area
4. Analyze the spatial continuity of small scale sub-channel morphology and compare it to Go-LIVE derived surface strain rates
5. Determine vertical melt rates in the channel, illustrate their spatial variability, and investigate possible mechanisms of channel formation using these data

Detailed DEMs and DITMs provide a description of the NIS and its basal channel, and contribute to quantifying the relationship between channel shape and ice shelf strain from Go-LIVE data. This analysis also provides insight into melt patterns within the NIS basal channel, and demonstrates the capability of repeat, high resolution, gridded IPR surveys to characterize and model changes in basal channels elsewhere. Hydrostatic equilibrium is often used in mass balance studies of the Antarctic's ice shelves to approximate ice thickness (Rignot et al., 2013), or to identify basal channels (Alley et al., 2016) using satellite derived surface elevations. In this thesis, comparing measured ice thickness to ice thickness derived from hydrostatic calculations allows the validity of this assumption to be examined across the NIS and its basal channel.

1.3 Thesis structure

This thesis is organized into seven chapters. Chapter 2 reviews the relevant literature of ice shelves and the technology used to measure them. The stability of ice shelves, their role in regulating ice mass flow into the ocean and interaction at the ice-ocean interface is explained. The current body of work related to measuring, and describing Antarctic basal channels is summarized through physical descriptions, classifications, and potential roles in ice shelf stability. Background knowledge of electromagnetic theory, IPR, and velocity derived strain rates are described.

Chapter 3 introduces the field site, the Nansen Ice Shelf, on the Victoria Land Coast of the East Antarctic. This introduction includes a physical description of the field site and the surrounding ocean.

Chapter 4 details the methods used in this thesis. Field methods included ground-based and airborne IPR systems, and precise surface elevation measurements. Custom software for picking radar data were used to produce ice thickness values. Geoid models and precise point positioning (PPP) services were utilized together to generate accurate surface elevations and to calculate ice draft relative to sea level. Computational methods used for the analysis of the processed data are also described. Finally, uncertainty associated with ice thickness, surface elevation, and ice draft values from both the ground-based and airborne radar systems are discussed.

Chapter 5 presents the results including the NIS DEMs and DITMs, strain rates calculated from Landsat-derived surface ice velocities, melt rates, and an examination of the hydrostatic balance across the NIS.

Chapter 6 discusses the results in order to characterize the behaviour of the NIS basal channel in the context of the larger NIS environment. Basal channel morphology, melt rates, and strain regimes are compared to basal channels described elsewhere in the Antarctic. The complex morphology revealed by the dense grid of IPR and how it relates to local strain rates and hydrostatic imbalances is also discussed in comparison to other work. The future stability of the NIS is discussed using historic information for context and observed patterns between basal channel formation and ice shelf behaviour.

Chapter 7 lays out the conclusions of the NIS and reports on the outcome of each of the thesis objectives. Future work is recommended to explore possible driving factors that may drive the NIS's dynamics.

Chapter 2

Ice Shelf Processes and Measurement Techniques

Variables that affect ice shelf stability and their role in ice sheet mass loss include ice shelf buttressing, the stress and strain experienced by ice shelves, and interactions at the ice-ocean interface. The current state of knowledge of ice shelves, as well as the glaciological techniques used to study them, provides the essential background knowledge that is relevant to this thesis.

2.1 Ice shelf processes

Figure 2.1 shows an along flow cross section of a typical ice shelf advecting over a grounding line and the changes in its ice thickness with distance from land. Ice shelves are typically thinner at the ice shelf edge where they ultimately calve. Following this trend of ice thickness, hydrostatic equilibrium dictates that surface elevations near the grounding line are typically higher than at the ice shelf edge, producing a net-downward slope.

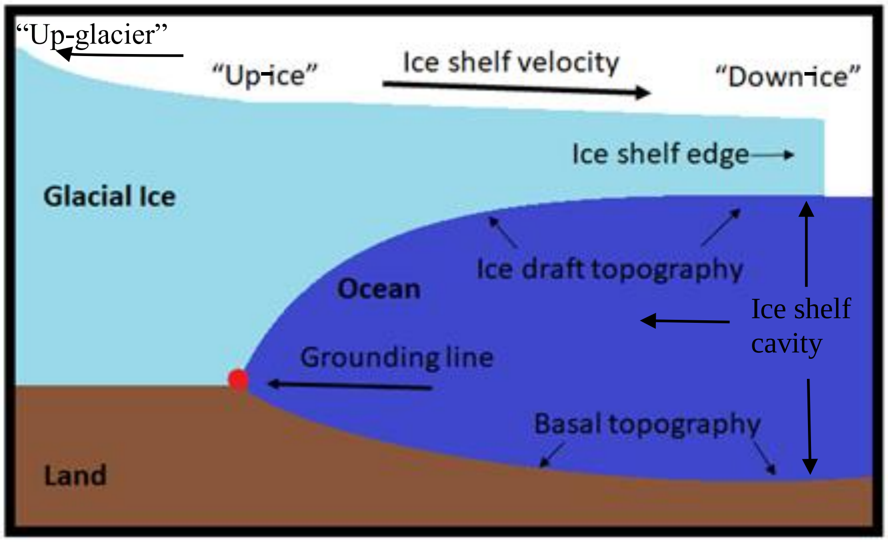

Figure 2.1: Schematic of a typical ice shelf labeled with terminology used in this thesis. Quotation marks denotes terminology used for relative positioning.

2.1.1 Ice shelf buttressing

Ice shelf buttressing is defined as the backwards directed stress that ice shelves apply on the grounding line of glaciers and ice sheets (Dupont and Alley, 2005). Buttressing forces greatly reduce the centerline velocity of grounded glaciers into the ocean (Scambos et al., 2004, Furst et al., 2016). Back-stress is derived from the drag forces experienced by the sides of the ice shelf that are in contact with the coast or pinning points. Pinning points are land masses that ice shelves come in contact with down-ice from the grounding line which are surrounded by floating ice. They have a large mitigating effect on discharge rates of tributary glaciers (Favier et al., 2012), and loss of contact with them (e.g. from basal melting) increases ice discharge rate significantly. Ice shelves that are not in contact with the coast or pinning points (an unconfined ice shelf) provide little buttressing force in comparison to confined ice shelves (Massom et al., 2015).

A draw-down of ice surface elevation has been observed in many Antarctic grounded glaciers as a result of reductions in buttressing forces from thinning or collapse of ice shelves (Shepard et al., 2004; Dutriex et al., 2014; Dupont and Alley, 2005; Greenbaum et al., 2015). After the disintegration of the Larsen B ice shelf on the Antartcic Peninusla, the resulting reduction in buttressing caused an acceleration of up-glacier grounded ice by a factor of 2 - 6 (Scambos et al. 2004). The retreat of ice shelves on the Antarctic Peninsula has resulted in large mass balance changes of grounded ice with 60% of mass loss directly attributed to a reduction of ice shelf buttressing forces there (Scambos et al. 2014).

The thinning and retreat of ice shelves in the Amundsen Sea (WAIS) has caused up-glacier grounded ice surface elevations to draw down by up to 5.5 m yr^{-1} (Shepard et al. 2004). Of particular interest is the thinning of Pine Island Glacier (PIG) and Thwaites Glacier of the WAIS, which has been attributed to the thinning of their ice shelves from CDW intrusion (Dutrieux et al. 2013, Dutrieux et al. 2014, Joughin et al. 2014). Unique basal topography allowing for warm ocean water intrusion under the Totten Glacier Ice Shelf has also made the EAIS vulnerable to change, contributing the largest rates of ice mass loss in the EAIS (Greenbaum et al. 2015).

2.1.2 Ice shelf stability

The stability of an ice shelf is defined here as its ability to retain mass and continue to provide a buttressing force to grounded ice (Furst et al., 2016). Ice shelves lose mass, and become less stable, either through calving, basal melting or surface melt. Approximations of ice shelf thickness are required to monitor mass change of ice-shelves across the Antarctic (Rignot et al., 2013) and are estimated on large scales by measuring surface elevation with satellite laser altimeters and then assuming hydrostatic equilibrium (Griggs and Bamber, 2011). The volume of ice mass loss on all major Antarctic ice shelves from calving and melting has been calculated using 5 years of satellite altimetry observations (Figure 2.2) (Rignot et al. 2013).

The calving process is a major contributor to ice shelf mass loss that causes sudden reductions in buttressing forces and begins after the formation of crevasses. There are two types of crevasses on ice shelves that can contribute to calving: surface crevasses that form on the ice shelf surface

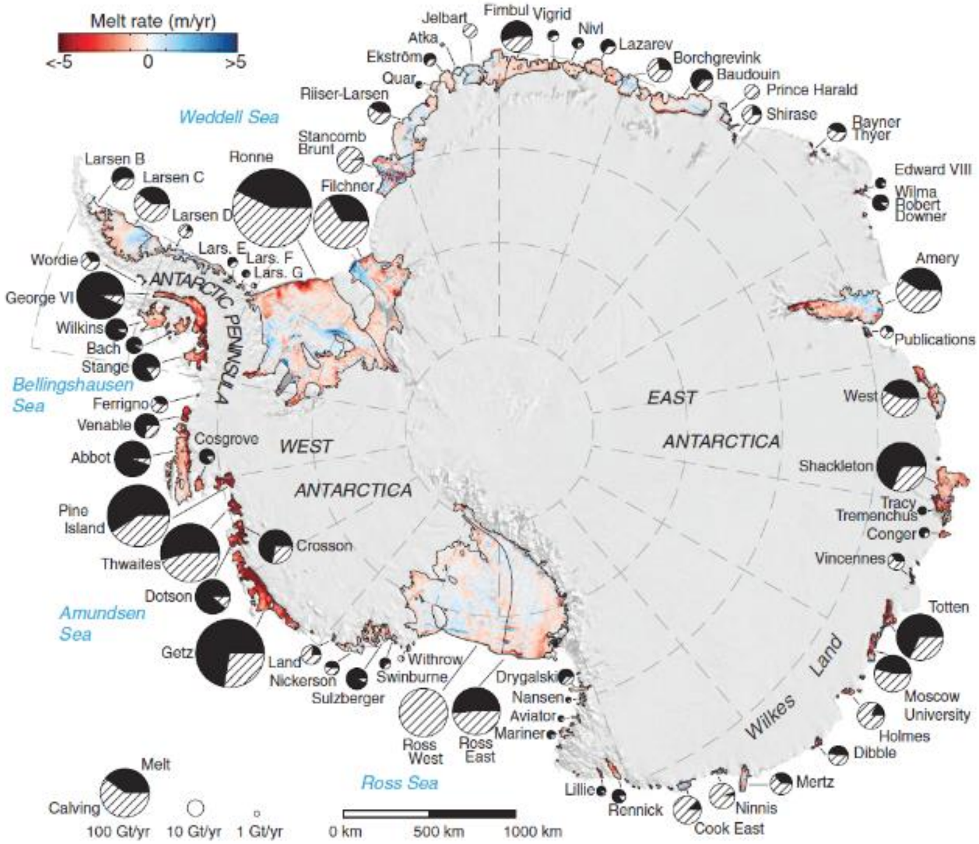

Figure 2.2: Map of Antarctica showing the total estimated mass loss from ice shelves from 2003 to 2008 as well as the relative mass loss from basal melting vs calving (Rignot et al. 2013)

and penetrate down into the ice shelf, and basal crevasses that form on the ice shelf base and penetrate up into the ice shelf (Weertman, 1973). There are then two ice shelf calving processes, surface crevasses being advected down-ice towards the thinner ice shelf edge where they may then penetrate the full ice thickness (Benn et al. 2007), or basal crevasses doing the same (Nick et al. 2010). Crevasses that penetrate the full ice thickness are called rifts and in the Antarctic, they can expand laterally across the width of an ice shelf, which leads to large calving events, such as the 2017 Larsen C calving event (Hogg and Gudmundsson, 2017). This process often occurs nearer to the ice shelf edge where ice is thinner and rifts can form and spread laterally more easily. There is no unifying calving law that predicts precisely when or how calving will occur (Bassis, 2011).

In comparison to surface crevasses, basal crevasses are less commonly observed (Luckman et al. 2012), but have been detected with a greater frequency in floating ice shelves/tongues than in terrestrial glaciers (Van Der Veen, 1998). Crevasses originating at the base of an ice shelf have been estimated to initially penetrate up to two thirds of the full thickness of an ice shelf, affecting the strain response and mechanics of the ice shelf (Luckman et al. 2012). Ocean water can freeze as marine ice within basal crevasses ice due to super cooling when water rises into the newly opened space, rapidly decreasing the pressure-freezing point (Bassis and Ma, 2015).

2.1.3 Ice-ocean interaction

Ice-ocean interactions modellers have elucidated empirical formulas for ice-ocean melting (Holland and Jenkins 1999), mechanisms for the freezing and accumulation of marine ice (Lewis and Perkins, 1986), as well as the influence of temperature and basal topography on melt rates (Holland et al., 2008).

Ocean-driven ice shelf thinning currently accounts for 40% of annual Antarctic mass loss (Pritchard et al. 2012) which is especially large around the WAIS, particularly in the Amundsen Sea, where the ice shelves there have lost 18% of their thickness since 1994 and ice shelf mass loss rate has increased 70% in the last decade (Paolo et al. 2015). Figure 2.2 demonstrates that ice shelf size alone does not determine net mass loss, as the four largest ice shelves contribute a small fraction of total Antarctic meltwater due to the protected cold continental shelf waters underneath their large areas (Rignot et al., 2013). The ice shelves that contribute the most meltwater tend to do so through basal melting as opposed to iceberg production from calving, highlighting the ocean’s control on melt flux from ice shelves (Rignot et al., 2013)

The freezing temperature of sea water is a linear function of pressure and a weakly non-linear function of salinity, and is referred to as the pressure-freezing point (Millero, 1978). When the non-saline glacial ice crosses over the grounding line and comes into contact with high pressure, saline, ocean water, ice begins to melt because of relatively low pressure-freezing points at the ice-ocean interface (Holland and Jenkins, 1999). Submarine melting from contact with ocean-water begins at the grounding line and continues along the length of the ice-ocean interface towards the ice shelf edge (Cuffey and Paterson, 2011). Assuming a constant salinity, the pressure-freezing temperature of water decreases with depth, which is why (with all other factors being equal) there is typically a faster melt rate along the ice-ocean interface at the grounding line than there is near the ice shelf edge (Holland and Jenkins, 1999).

Melt rates in the ice shelf cavity are also controlled in part by large-scale oceanic circulation driven by thermohaline gradients that influence mass and energy exchange at the ice-ocean interface (Jenkins, 1991). The relationship between ice shelf cavity melt rates and ocean temperatures was variable between a number of studies as summarized in Figure 2.3 (Hellmer et al., 1998; Jenkins, 1991; Rignot and Jacobs, 2002; Shepard et al., 2004; Williams et al., 1998; Williams et al., 2002). This previous work was re-examined by Holland et al. (2008) with a description of a more comprehensive, full ocean general circulation model for an idealized ice shelf cavity. It was concluded that the relationship between ice shelf melt rates and ocean warming is quadratic because of the cumulative linear relationships between melt rate with both ocean temperature and the ocean cavity’s basal topography (see Figure 2.1; Holland et al., 2008). Basal topography consequently has a large effect on the melt rate of an ice shelf and serves as a proxy for ocean circulation characteristics in the ice shelf cavity. Deeper cavities are more susceptible to warm water intrusions and this will increase ice shelf basal melt, as has been observed in the Amundsen Sea and the Totten Glacier in the East Antarctic (Greenbaum et al.

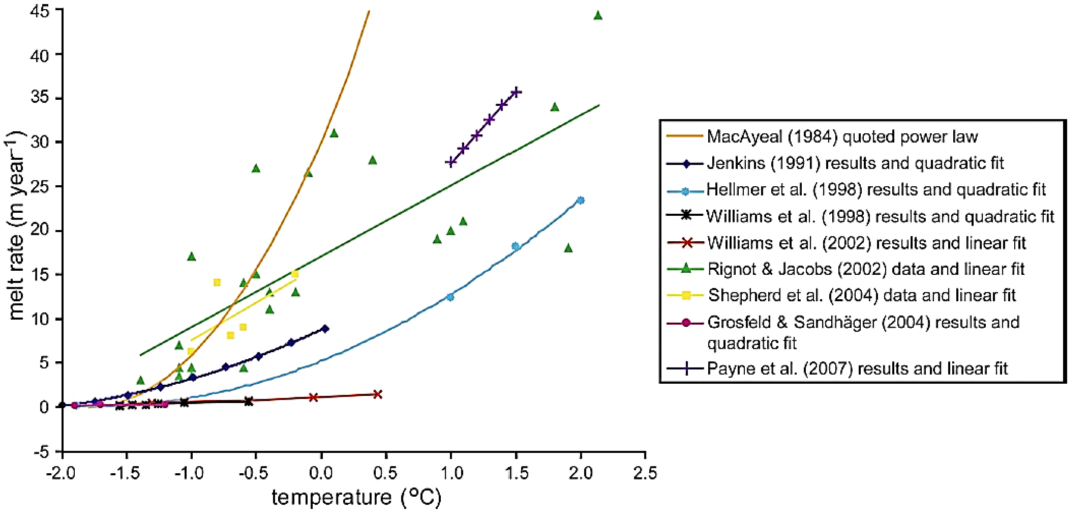

Figure 2.3: Graph from Holland et al. (2009) showing a summary of previous work attempting to characterize the relationship between ocean temperature and basal melt rate

2015). Rignot et al. (2013) also found basal melt rate was associated with deeper basal topographies from their Antarctic wide ice shelf mass balance study (Figure 2.2).

Marine ice is highly saline ice that freezes out of ocean water onto the bottom of pre-existing ice bodies and can accumulate substantially in ice shelf environments along the ice-ocean interface producing additional ice thickness (Tison et al., 2001). The fundamentals of the ‘ice pump’, a marine ice accumulation model, is illustrated in Figure 2.4 (adapted from Lewis and Perkins, 1986) where a vertical column of ice is submerged in a column of seawater of height H, and the interface between them is the line AA. Melting occurs at the bottom of the interface where the pressure and salinity are greater, generating relatively fresh, super-cooled, low density melt water, which rises to the top of the water column. The pressure freezing point decreases as the super-cooled water rises up the column where it freezes-on to a given surface. Where freezing occurs, salt is expelled, driving relatively dense water downward towards the base of the water column. Sinking saline sea water enhances the rising of super-cooled water in a convection cell that initiates the pump mechanism. Over time, the differential melting and freezing caused by the ice pump will change line AA to line BB where the new ice deposited at the top of the ice column will be ‘marine ice’ with no air bubbles and an order of magnitude more salt inclusions than glacial ice (Tison et al. 2001). Measurements of thick layers of accumulated marine ice have

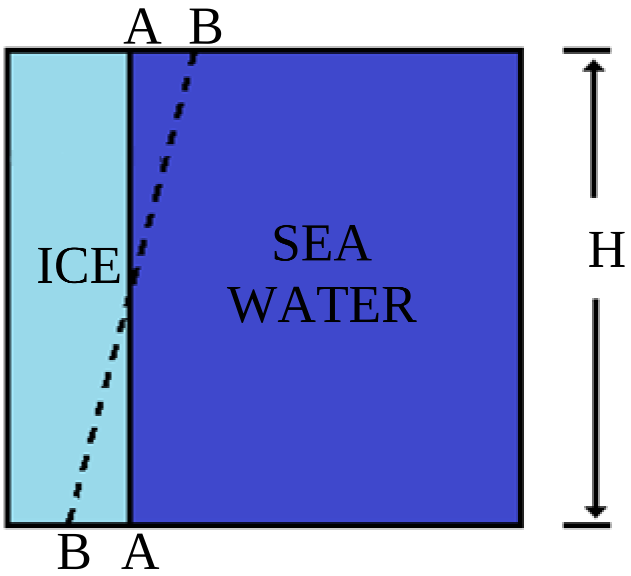

Figure 2.4: Schematic of the ice pump. Line AA represents the original interface of height H, and line BB is the new interface caused by ice pumping after some time t (modified from Lewis and Perkins, 1986)

revealed vertical stratification with internal freezing and melting zones (Tison et al., 2001). Thick layers of marine ice form in relatively calm environments under an ice shelf such as basal crevasses, rifts near the grounding line, and possibly in basal channels where super-cooled meltwater can rise into topographical apexes where it will be protected from mechanical mixing by turbulent ocean currents (Tison et al., 1993). The formation of marine ice is an important process in the ice shelf cavity as marine ice possesses different rheological and electrical properties than glacial ice (Dierckx and Tison, 2013), which is an important consideration for the IPR investigation presented in this thesis.

2.2 Antarctic basal channels

Basal channels are melt features formed at the ice-ocean interface from consistent enhanced energy delivery to a particular location, melting out inverted channels over time (Rignot and Steffen, 2008). Basal channels have been observed to possess a variety of lengths, widths, heights, and formation mechanisms, and have been categorized based on these characteristics (Alley et al., 2016). The effect of basal channels on ice shelf stability remains controversial (Gladish et al., 2012; Rignot and Steffen., 2008; Vaughan et al., 2012).

2.2.1 Physical description

Basal channels require a source of heat to locally enhance melt, which may vary depending on the location of the channel and the ocean dynamics in the ice shelf cavity. Basal channels form at the ice-ocean interface due to relatively warm buoyant plumes rising along a variably sloped ice draft topography, finding preferred paths in local apexes of the ice draft topography, andenhancing melt along these preferred paths over time (Sergienko, 2013). Based on estimations using surface elevation data, Antarctic basal channels range in width from 1 to 5 km across, 50 to 250 m tall and can be 100s of km long (Alley et al., 2016). Basal channels have been observed to grow over time, such as a 20 km extension of the Getz Ice Shelf basal channel over 30 years (Alley et al. 2016). The highest concentration of basal channels is under the ice shelves of the WAIS, where CDW intrusion in the Amundsen Sea appears to be linked to ~ 92 % of the basal channels there (Alley et al., 2016; Drews et al., 2015). The velocity of buoyant plumes is also a variable that can contribute to melting ice by increasing the relative energy transport and turbulence, which is generated by the movement of ocean water across a rough, non-uniform, ice surface (Jenkins, 2011).

Models have suggested that enhanced melting as a result of buoyant plumes seeking transverse variation in ice thickness is feasible mechanism for formation and growth of basal channels (Drews et al, 2015; Sergienko, 2013). Transverse variations in ice draft topography are common on ice shelves and are caused by land features near the grounding line, pinning points, or suture zones (convergence of tributary glaciers of differing ice thicknesses) (Sergienko, 2013). Suture zones between ice shelf branches (segments of an ice shelf directly sourced to a tributary glacier at the grounding line) often have contrasting ice thicknesses, and can support the formation of basal channels such as those observed between the three branches of the Amery Ice Shelf (Fricker et al. 2009; Sergienko, 2013). Also, meltwater outflow at the grounding line can provide sufficient energy to melt a basal channel as is observed with the presence channels near the grounding line of the largest, fastest flowing Antarctic glaciers (Le Brocq et al., 2013).

Most basal channels in the Antarctic are oriented seaward (north), with many possessing evidence of enhanced melt through the Coriolis effect, whereby channels are either steeper on their western flank or deflected towards the west on the kilometre scale (Alley et al., 2016;

Dutrieux et al., 2013; Dutrieux et al., 2014; Gladish et al., 2012; Mankoff et al., 2012; Millgate et al, 2013; Sergienko, 2013). The Coriolis effect is a pseudo-effect caused by the rotational velocity of Earth, and causes deflection of large bodies of fluid that are not grounded, such as the atmosphere and ocean. In the Southern Hemisphere, the Coriolis force deflects large fluid bodies to the left, as seen in the deflection of northward flow to the west. The Coriolis effect exerts a control on ice shelf channel shape by preferentially increasing the water velocity along one channel flank, melting the channel asymmetrically by increasing the energy delivery, turbulence of the current, meltwater production and meltwater removal. The Rossby radius is a horizontal scale that indicates the relative importance of the Coriolis effect in determining the behaviour of circulation dynamics over those distances (Nurser and Bacon, 2012). In the Antarctic, the Rossby radius is on the order of hundreds of m and is therefore often manifested in basal channels that are tens of km long (Holt et al., 2017).

Transverse profiles of large basal channels/channel networks have been modeled and suggest that channel features are often sinuous and that adjacent channels can have separate meltwater currents (Mankoff et al. 2012; Vaughan et al. 2012). Boreholes drilled into a basal channel on the PIG Ice Shelf identified a buoyancy driven boundary layer within the channel where the warmest water existed as a discrete layer at the channel apex (Stanton et al., 2013). Water stratification within basal channels has been poorly quantified in most identified channels, yet likely has a significant role in small scale melt patterns because without the ability to remove meltwater, melt rates in these features will become reduced (Dutrieux et al. 2014).

It has been observed that general basal channel form is often discernable through hydrostatic equilibrium, albeit in an attenuated form where smaller scale details are not often observable through surface elevations (Drews et al. 2015; Gladish et al., 2012; Mankoff et al., 2012; Vaughan et al., 2012). Drews et al. (2015) concluded that wider channels were more likely to be visible as a surface depression while bridging across smaller features prevents them from being in hydrostatic equilibrium at the surface. Bridging effectively holds a narrow band of thin ice at higher elevations than buoyancy should allow with the requirement that neighbouring ice is of a sufficient contrasting thickness to prevent the surface from depressing through hydrostatic balance (Deutrieux et al., 2014). An investigation by Dutrieux et al. (2014) discovered small scale features within a basal channel, not identifiable through corresponding surface elevation variations where channel flanks were ‘stepped’ with terraces separated by 5-50 m tall walls, illustrating that melt rates within the channels may be very heterogeneous. Other work mentioned complex ice draft topographies, or extreme variations in ice thickness within channels, (Gladish et al., 2012, Vaughan et al., 2012) but did not attempt to describe smaller scale sub-channel morphology.

2.2.2 Classifications

Alley et al. (2016) completed a comprehensive survey of the distribution of large basal channels around the Antarctic. Satellite laser altimetry was used, assuming hydrostatic equilibrium, to identify potential channels and airborne IPR used to confirm their presence where possible. Basal channel locations and ‘category’ are shown in Figure 2.5. Four categories of basal channels were assigned: subglacially sourced, grounding-line-sourced, ocean-sourced, and potential channels. Channels that originate at the grounding line, where subglacial outflow is predicted, are called ‘subglacially sourced channels’ and are observed to be deeply incised into the ice shelf at the grounding line and then dissipated down-ice. ‘Ocean-sourced channels’ do not originate at the grounding line but some location down-ice from it. ‘Grounding-line sourced channels’ originate at the grounding line but are not associated with areas of predicted subglacial outflow and had a morphology similar to that of ocean-sourced channels. The main morphological feature of grounding-line and ocean-sourced channels is that they do not dissipate along flow, but rather tend to deepen. The study identified ‘possible channels’ when information collected was insufficient to confirm the presence of a channel at the time (e.g. the Nansen Ice Shelf in Terra Nova Bay; Alley et al., 2016).

The origin of these basal channels is partially speculative due to the lack of observations of small scale melt and ocean circulation patterns. For example, a sub-glacially sourced channel may have ocean inputs that make the channel appear to belong to the grounding-line sourced channel category. Ocean-sourced channels are less ambiguous in their classification as it is unlikely that another process drives formation of channels down-ice of the grounding line. To better quantify the origins of basal channels, more observations of ice draft topography, ocean current turbulence velocity, and meltwater production are necessary (Alley et al. 2016).

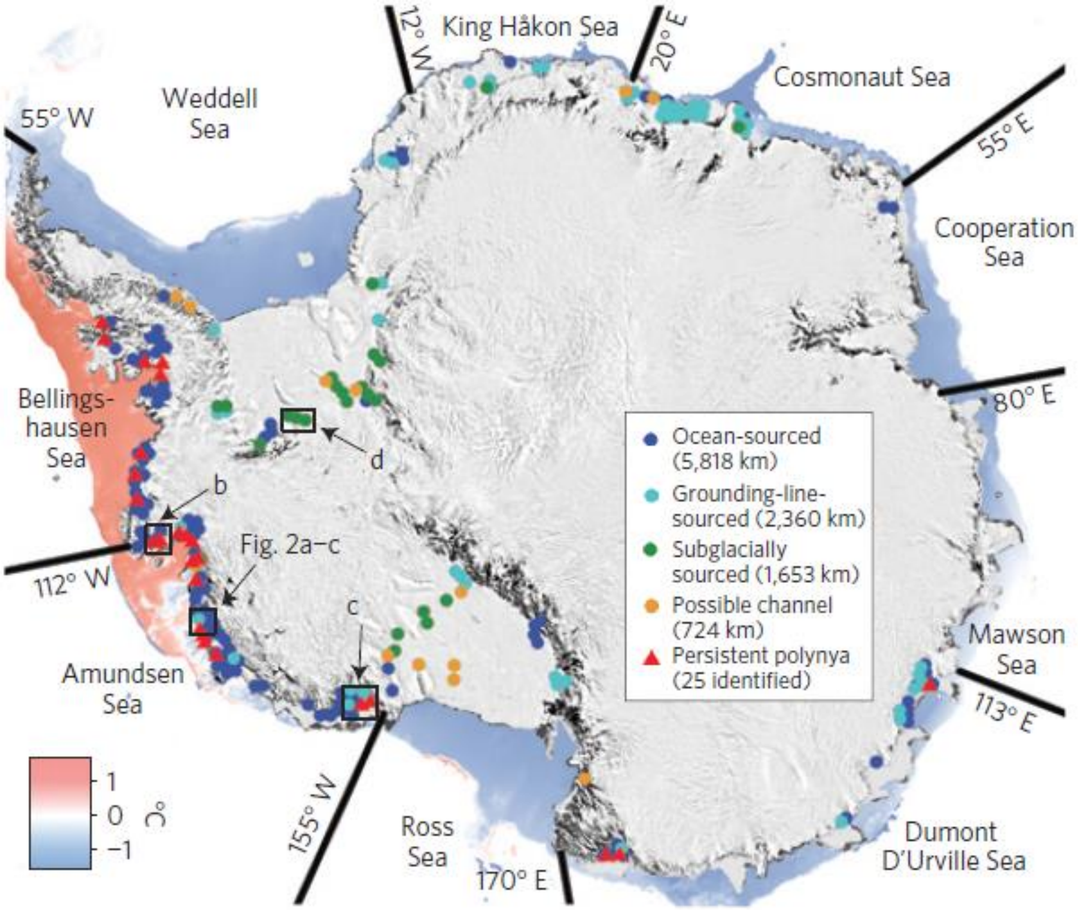

Figure 2.5: Antarctic map showing the distribution of basal channels as identified by satellite altimetry and/or confirmed with airborne radar surveys. The highest concentration of channels can be seen adjacent to regions with warm ocean water. (Alley et al., 2016)

2.2.3 Role in ice shelf stability

The role that basal channels play in ice shelf stability is controversial. The formation of basal channels in the presence of upwelling warm water to the ice-ocean interface has been argued to regulate and reduce total melt across the entire ice shelf by focussing the warmest water away from the rest of the ice shelf and into the basal channel (Gladish et al. 2012; Millgate et al. 2013; Stanton et al. 2013). The previously mentioned relationship (in Section 2.2.2) between buoyant warm water seeking shallow ice drafts and channel formation challenges the idea that distributed films of upwelling warm water in the presence of non-uniform ice draft topographies can persist, without the formation of basal channels (Segienko, 2013).

Other work has looked at the structural implications of large kilometre-wide basal channels and the role this plays on ice shelf stability (Dutrieux et al., 2014; Drews et al. 2015; Dow et al. 2018; Rignot et al. 2008; Sergienko 2013; Vaughan et al., 2012). Sergienko (2013) modelled the impacts of basal channel formation on ice shelf strain regime. Localized thinning from channel formation can generate areas of fracture initiation that may result in crevassing around a channel (Sergienko, 2013). This prediction is in agreement with identified surface and basal crevasses spatially correlated with a network of sinuous basal channels in the PIG Ice Shelf (Vaughan et al., 2012). It was hypothesized by Vaughan et al., (2012) that these crevasses form as a response to bridging stress, where the thin ice bridging the channel flexes downward towards hydrostatic equilibrium. Dow et al. (2018) argued that the strain response of ice shelves to basal channel formation can generated surface crevasses across the width of a basal channel. Interactions between surface crevasses in topographical depressions on ice shelves and concentrated surface melt was determined to be a possible driving factor in a large calving event on the NIS (Dow et al., 2018). The interaction between surface melt and surface crevasses could provide a mechanism by which basal channel formation and warming atmospheric conditions may lead to large calving events and ice shelf buttressing reductions around the Antarctic. Regardless of whether or not channelized ocean melt reduces the net basal melt of an ice shelf, there is sufficient evidence to suggest that channel growth within an ice shelf can encourage crevassing, calving and mass loss (Dow et al., 2018; Sergienko et al., 2013; Vaughan et al., 2012).

It remains difficult to predict future growth of basal channels without quantifying or measuring the degree of metre scale variability in melt rates, ice draft topography, and ocean circulation within basal channels. (Drews et al., 2015; Gladish et al, 2012; Mankoff et al., 2012; Millgate et al., 2013; Sergienko, 2013; Vaughan et al 2012).

2.3 Measurement techniques

2.3.1 Radar

Measurements of ice shelf thickness have progressed due to advancements in the radar systems that transmit and receive information using electromagnetic waves. Conversely, GPR has advanced due to the early pioneering work testing the theory and systems on ice sheets (Waite and Schmidt, 1961). The theory around GPR/IPR has generated its own terminology but is founded on electromagnetic theory (Annan, 2009). Electromagnetic fields can propagate with either wave or diffusive properties depending on the frequency of the field being emitted and the electrical properties of the medium they are travelling through (Annan, 2009). Considering the propagation of a sinusoidal electromagnetic field with some frequency f (as produced by an IPR system) the behaviour of this field as it travels through a geologic medium can be written as (Annan, 2009):

$$\nabla^2 B = 2\pi f \mu \sigma i B - (2\pi f)^2 \mu \varepsilon B \quad (2.1)$$

$$\nabla^2 E = 2\pi f \mu \sigma i E - (2\pi f)^2 \mu \varepsilon E \quad (2.2)$$

where B is magnetic induction or flux density (Wb m^{-2}), E is the electric field intensity (V m^{-1}), ε is dielectric permittivity in farads per metre (F m^{-1}), μ is magnetic permeability in Henrys per metre (H m^{-1}), σ is electric conductivity in Siemens per metre (S m^{-1}), f is the frequency of the field emitted (Hz) and i is the imaginary phase component of the wave. There are several important implications of Equations 2.1 and 2.2 as they pertain to the application of radar surveys. Firstly, there are three physical properties that affect the propagation of an electromagnetic field through a medium: μ, ε, and σ (Annan, 2009). For IPR surveys, it is assumed that μ is small and constant within glacial ice and is thus negligible. The frequency used will determine electromagnetic propagation as either a wave or as a displacement current based on the frequency f used; where for wave propagation:

$$f \gg \frac{\sigma}{2\pi\varepsilon} \quad (2.3)$$

which for low conductivity material, such as impermeable isotropic glacial ice, is typically 2 MHz and above (Arcone, 2009). To maintain electromagnetic wave propagation in physical media, frequency needs to increase with electrical conductivity to continue to meet the condition in equation 2.3.

Dielectric permittivity and electric conductivity are the most variable physical properties within glacial ice and influence the speed of propagation of electromagnetic waves and the magnitude of wave reflection at the ice-ocean interface. Dielectric permittivity is a measure of a medium's ability to displace charge in its material structure under the influence of an electromagnetic field (Annan, 2009), or, how well a medium behaves as a capacitor under an electromagnetic field. The dielectric material (solid or liquid water) does this by temporarily adjusting the alignment of its molecules and electrons. Liquid water has a higher dielectric permittivity while solid glacial ice has a lower dielectric permittivity.

There is an inverse relationship between dielectric permittivity and electromagnetic wave velocity described by:

$$v = \frac{c}{\sqrt{k}} \tag{2.4}$$

where c is the speed of light in a vacuum and $\kappa$is a dimensionless quantity called the dielectric constant (Annan, 2009) defined by:

$$\kappa = \frac{\varepsilon}{\varepsilon_0} \tag{2.5}$$

where ε is the dielectric permeability of the material in question, and ε_0 is the dielectric permeability of a vacuum (8.8542x10^{-12} F m^{-1}) (Annan, 2009). Typical dielectric constants for ice and pure water are 3.2 (Arcone, 2009) and 80 (Annan, 2009) respectively. Contrasts in dielectric permittivity between horizontal layers equates to velocity changes between horizontal layers, which changes the amplitudes and signature of waves upon arriving at these interfaces. At interfaces, some of the electromagnetic energy is typically reflected upwards while some of the energy passes through the interface (Neal, 2004). The change in amplitude and the relative magnitude of the reflection of the electromagnetic wave is related to the reflection coefficient R at the interface:

$$R = \frac{\sqrt{k_2} - \sqrt{k_1}}{\sqrt{k_2} + \sqrt{k_1}} \tag{2.6}$$

where k_1 and k_2 are the dielectric constants of the upper and lower layer respectively (Neal, 2004). The closer R is to 0 (no interface) the smaller the change in amplitude of the wave. A limiting value of 1 is used for R to signify a reflection near unity, where all of the signal is reflected off of the interface (Neal, 2004). Electromagnetic wave reflections off the interface are then detected as returns by the Rx after some time t, dependent upon the distance between the Tx and Rx called the offset, and the velocity of the wave though the medium such that:

$$t_x{}^2 = t_o^2 + \frac{x^2}{v^2} \tag{2.7}$$

where t_x is the two-way travel time of the wave from the Tx to the interface and back to the Rx, t_o is the zero offset travel time (the time it would take for the wave to go straight down to the interface and straight back again to Tx), x is the offset between the Rx and the Tx, and v is the speed of the wave through the medium (illustrated in Figure 2.6). The time at which the reflection occurred can be determined for every radar signal received, called a trace. Traces can be put side by side as a radar system moves across a surface at a fixed offset to generate a cross section image of the reflections from the subsurface called a radargram, such as seen in Figure 2.7, which contains 1152 traces. Time, antennae offset and wave velocity information can be interpreted and processed to provide high spatial resolution of ice thicknesses.

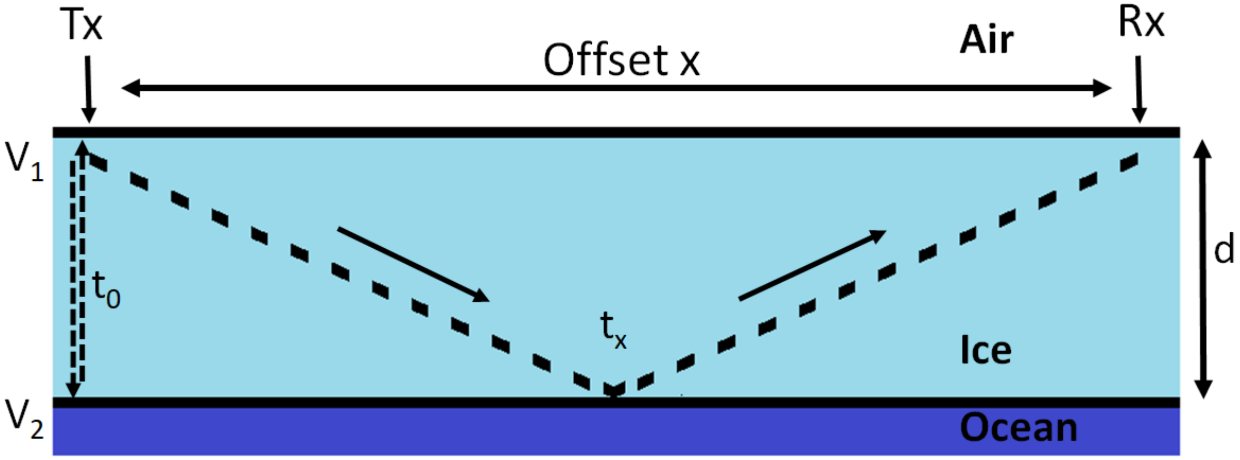

Figure 2.6: Single layer scenario for an idealized radar survey.

Lateral (horizontal) resolution of radar systems is a function of radar wavelength, and the one way travel distance to the interface, which for IPR on an ice shelf is ice thickness (Pearce and Mittleman, 2002). The horizontal resolution exists due to the cone shape of the transmitting radar wave; however, if ice thickness is much larger than the radar wavelength the secondary reflections from the target will not interfere with the first received reflection (Pearce and Mittleman, 2002).

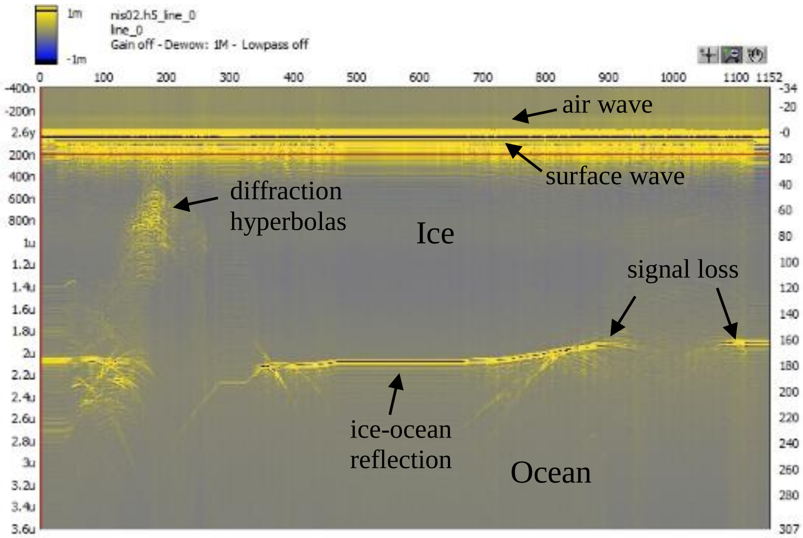

Figure 2.7: Annotated unprocessed radargram from 10 MHz ground-based IPR on the Nansen Ice Shelf. Areas of poor bed reflection can be caused by interference from features in the ice.

2.3.2 Electromagnetic wave propagation in ice

The dominant interface observed in IPR on ice shelves is the ice-ocean interface. Water is prevented from soaking up into an ice shelf because of the impermeability of glacial ice, making ice shelves ideal for radar surveys. From equation 2.6, the contrast in dielectric permittivity between glacial ice and ocean water generates reflection coefficients above 1, or complete reflections at unity (Arcone, 2009), generating signal returns from the ice-ocean interface as can be seen in Figure 2.7. Wave velocities within glacial ice are typically within the narrow range of 168-169.5 m μs^{-1} (Fujita et al., 2000). Factors that can affect the speed of electromagnetic wave propagation in glacial ice are: ice density, acidity from ash layers, and changes in crystal orientation fabric (Fujita et al., 2000).

There are three types of ice found in the ice shelf environment: glacial ice which is composed of meteoric ice, sea ice that forms on the ocean, and marine ice as described in section 2.1.3 each of which has different conductivities due to their formation processes and variable salt inclusions. Meteoric ice is the least conductive with salinity values an order of magnitude smaller than those of marine ice and a few orders of magnitudes less than sea ice (Dierckx and Tison, 2013). At low radar frequencies, significant changes in conductivity and dielectric permittivity from increased salinity of ice may change the behaviour of electromagnetic field propagation from displacement waves to diffusive currents removing signal return from the ice-ocean interface (Holland et al., 2009). The largest sources of interpretive error for IPR on ice shelves are no-signal returns generated by marine ice accumulation, as well as geometric scattering effects that produce diffraction hyperbolas (as labeled in Figure 2.7) with the latter caused by sharp topography gradients in ice shelf draft or englacial rock debris.

Marine ice causes loss of radar signal because: it has greater conductivity due to its higher concentration of salt inclusions (Dierckx and Tison, 2013), higher dielectric permittivity due to its softer and sometimes weakly consolidated physical state (Dierckx and Tison, 2013), and can posses discrete layering of these qualities, because of older marine ice ejecting saline sea water, where these variables will gradationally increase with depth. (Tison et al., 2001, Moore et al., 1994). Assuming adequate radar penetration, marine ice accumulation is the only physical process that causes loss of radar signal barring the effects of geometric scattering (Holland et al., 2009).

Geometric scattering is the effect caused by the expanding cone shape of the electromagnetic foot-print that propagates in all directions at once (Woodward and Burke, 2007). Geometric scattering can produce secondary returns from features perpendicular to the antenna orientation that may obscure the desired return as seen in Figure 2.7 (Olhoeft, 1998). If an ice shelf was a uniform planar feature, the interface directly underneath the Tx and the Rx would be the first one reached by a spreading hemispherical wave. However, in reality, other reflections may be detected by the Rx before this. For example, a basal crevasse apex located 10 m perpendicular to the radar survey direction in plane view would appear to be located directly beneath the system as a hyperbolic shape (due to the squared relationship in Equation 2.7) in the radar gram but at a depth greater than it truly exists, and the actual ice-ocean interface directly underneath the radar system would be obscured/ by the reflections from this crevasse.

2.3.3 Stress and strain

The physical stresses experienced by an ice shelf as it fills an embayment plays a significant role in fracture initiation, ice thinning, crevassing, and calving. Stress is a force applied to an object over a two dimensional area (N m^{-2}), and strain is the object's response to that stress. Strain is measured as deformation of an object's length per unit length resulting in a dimensionless scalar ranging from 0 to 1. When considering changes in ice thickness of an ice shelf, it is important to consider that as an ice shelf spreads to fill an embayment it thins vertically through conservation of mass. The amount of thinning is directly proportional to spreading which can be determined by the velocity of the ice shelf (Young and Hyland, 2002).

Ice shelves have less complex strain regimes than glaciers. Friction at the base of an ice shelf in contact with ocean water is negligible in comparison to the friction from contact between a glacier and rock (Cuffey and Paterson, 2011). In the absence of contact with land, the spreading of an ice shelf is understood as a simplified model of three principle axes of velocity and strain, where ice is incompressible. The relationship between velocity vectors and vertical strain rate on an ice shelf is related by conservation of mass:

$$\dot{\varepsilon}_1 = \dot{\varepsilon}_{xx} + \dot{\varepsilon}_{yy} + \dot{\varepsilon}_{zz} = 0 \tag{2.9}$$

where $\dot{\varepsilon}_1$ is the net strain rate of the ice, which is equal to zero and $\dot{\varepsilon}_{xx}$, $\dot{\varepsilon}_{yy}$, and $\dot{\varepsilon}_{zz}$, are the strain rates parallel to principal x, y and, z axis respectively (Weertman, 1973). Ice velocity change across the profile of an ice shelf can be influenced by a convergence of ice masses such as tributary glaciers, which will converge or spread to fill the shape of the embayment confining the ice shelf (Young and Hyland, 2002). If the change in velocity is known over time in the x and y direction (denoted by $\frac{du}{dx}$ and $\frac{dv}{dy}$), then the strain rate of $\dot{\varepsilon}_{xx}$ and $\dot{\varepsilon}_{yy}$ can be calculated by the equations:

$$\dot{\varepsilon}_{xx} = \frac{du}{dx} \tag{2.10}$$

$$\dot{\varepsilon}_{yy} = \frac{dv}{dy} \tag{2.11}$$

By tracking features on an ice shelf using satellite imagery, velocities can be calculated over some span of time *t* and through conservation of mass vertical thinning can be calculated (Young and Hyland, 2002) by:

$$\dot{\epsilon}_{zz} = -\left(\frac{du}{dx} + \frac{dv}{dy}\right) \tag{2.12}$$

Vertical strain, $\dot{\varepsilon}_{zz}$, is important to quantify as is operates independently of basal melting to thin an ice shelf as it spreads to fill an embayment.

Chapter 3

Site Description

The NIS is a small ~1800 km^2 ice shelf in Terra Nova Bay, Antarctica, located north of the western Ross Ice Shelf along the Victoria Land coastal ocean region of the western Ross Sea (Figure 3.1). The NIS drains part of the EAIS through the Transantarctic Mountains.

3.1 Location

The NIS is located at ~ 75 ˚S, 163 ˚E (Baroni et al., 1991), 20 km from Italy's Mario Zucchelli Station (74° 41′ S, 164° 6′ E) and 30 km from South Korea's Jang Bogo Station (74° 37' S, 164° 13′ E).

The two glaciers that supply the NIS are the Reeves Glacier to the south and the Priestley Glacier to the north (Figure 3.1). The Priestley and Reeves glaciers drain the Taylor Dome (the southern portion of which is seen in Figure 3.2), and are mostly separated from the alpine glaciers of the Transantarctic Mountains. The Priestley Glacier is more than 1000 m thick near its grounding line and has ice surface velocities up to 130 m yr^{-1}, with an estimated ice discharge of 0.77 ± 0.13 km^3 yr^{-1} (Frezzotti et al., 2000). The Reeves Glacier separates into two distinctive branches as it flows around the Teall Nunatak at the grounding line. Immediately down ice of this branch separation, there is a region of rifts that are filed with marine ice as evidenced by ice cores (2001 ice core in Figure 3.1; Khazendar et al., 2001, Dierckx and Tison 2013). The Reeves Glacier is ~700 m thick at its grounding line with an average surface ice velocity of 200 m a^{-1} and an approximate ice discharge of 0.52 ± 0.06 km^3 a^{-1} (Frezzotti et al., 2000). The grounding lines of the Priestley and Reeves glaciers are 70 km and 40 km from the ice shelf edge, respectively. The NIS ranges in thickness from 1000 m near the Priestley Glacier grounding line to 120 m at the ice shelf edge. The branches of the NIS formed by Priestley and Reeves glaciers converge, as shown by the flow lines of Figure 3.3, ~ 30 km from the ice shelf edge. An area of landfast sea ice connects the southern extent of the NIS with the smaller Larsen Glacier (Figure 3.1). The Drygalski Ice Tongue (hereafter DIT) is located further south and is also connected to the

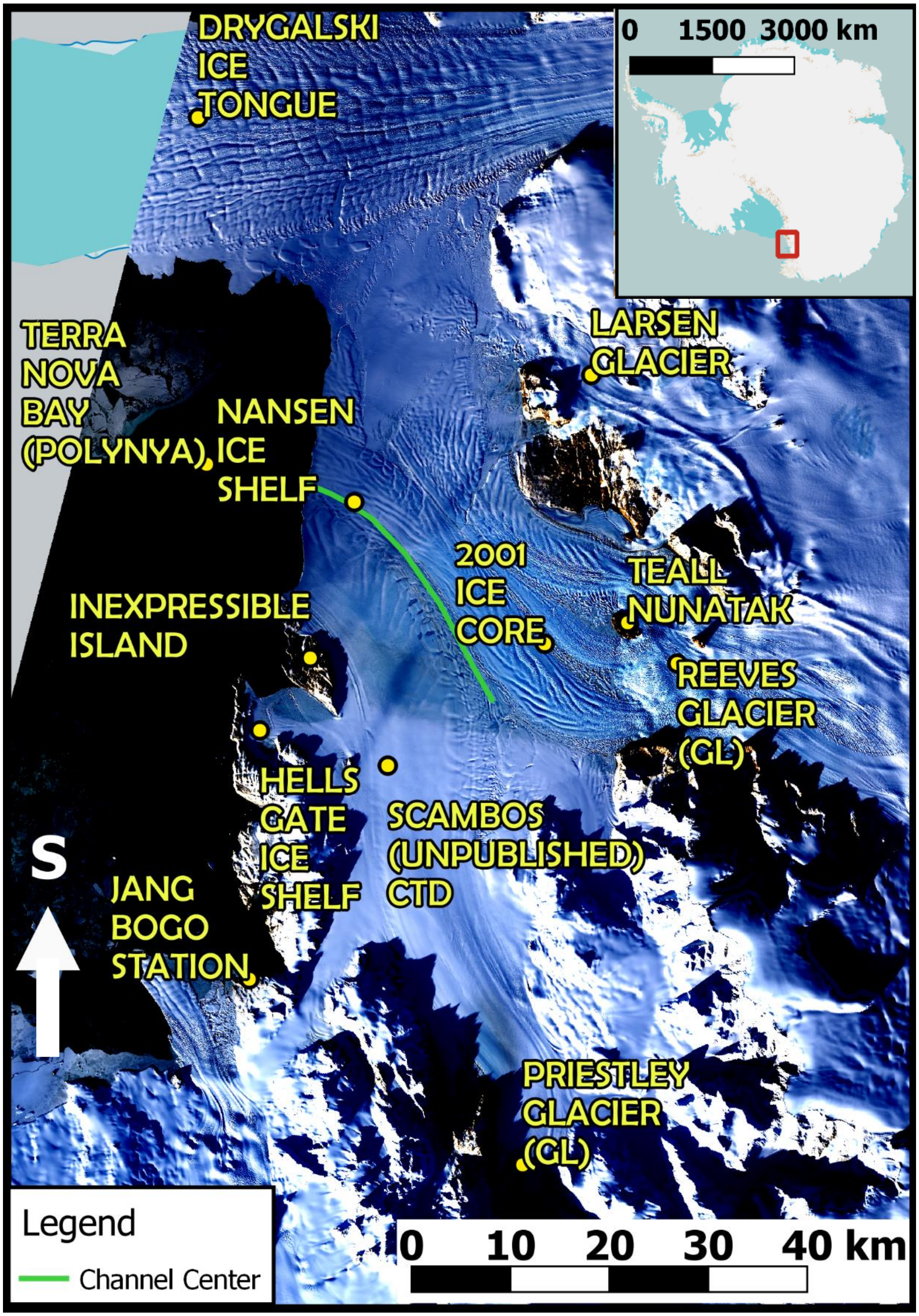

Figure 3.1: Location of the Nansen Ice Shelf, part of the East Antarctic Ice Sheet, along the Victoria Land Coast

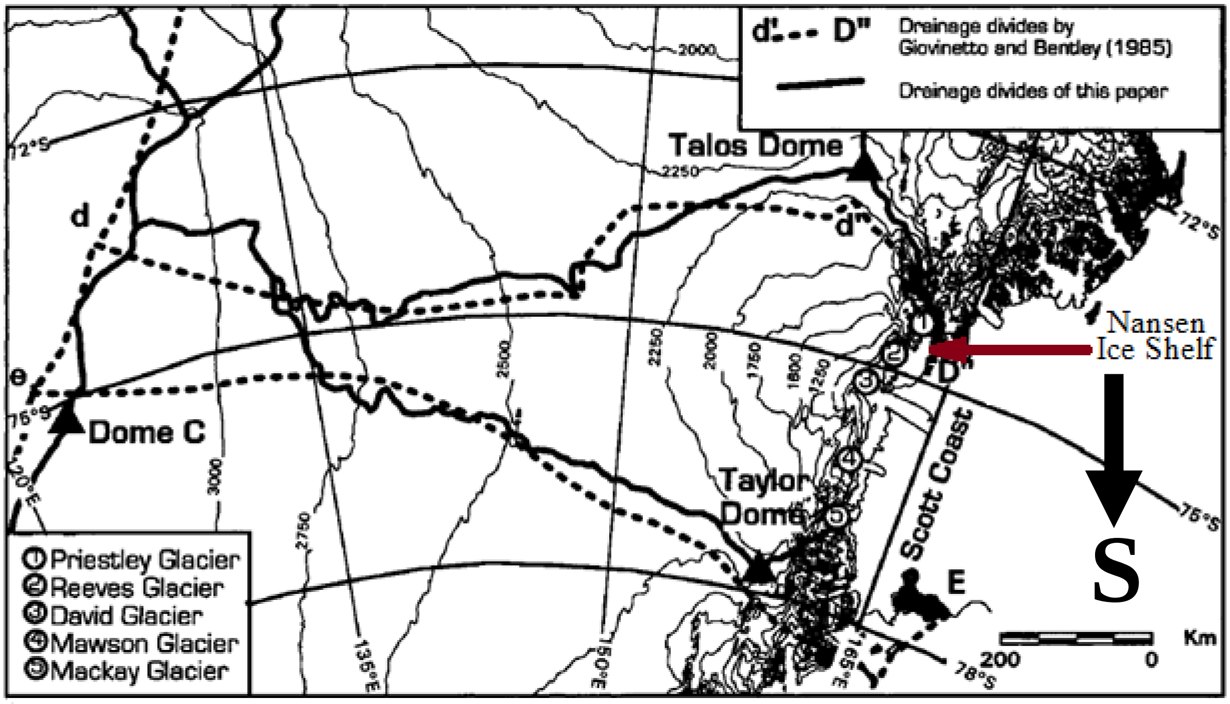

Figure 3.2: Drainage divides and study areas along the Victoria Land Coast (adapted Frezzotti et al., 2000)

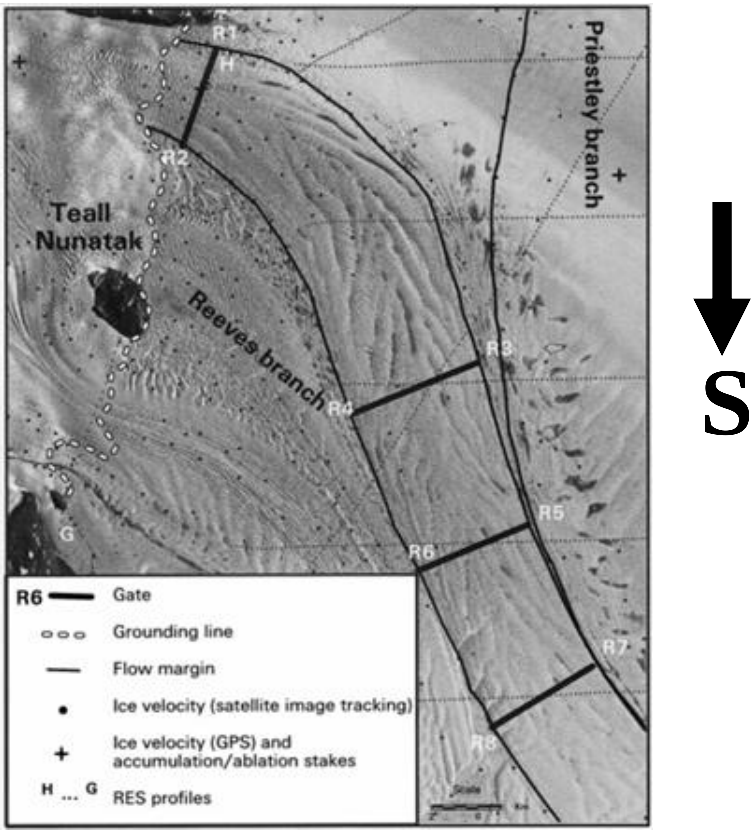

Figure 3.3: Glaciological survey results from Frezzotti et al, (2000) showing the grounding line and flow lines for the Reeves, and Priestly Glacier branches of the NIS. The basal channel examined in this thesis forms along the suture zone between the Reeves and Priestly seen here

NIS and Larsen Glacier by sea ice, and plays a significant role in sheltering Terra Nova Bay from ocean currents and drifting sea ice (Stevens et al., 2017). The Terra Nova polynya, which is kept free of sea ice year round by the presence of strong katabatic winds from the Transantarctic Mountains (Kurtz and Bromwich, 1983), is found along the NIS edge extending from Inexpressible Island to the DIT.

Inexpressible Island is a small land mass and pinning point located at the north-eastern end of the ice shelf edge dividing the main NIS from the smaller Hell’s Gate Ice Shelf. The Hell’s Gate Ice Shelf is relatively thin (~60 m thick) and has an area of exposed marine ice at it terminus that accretes onto its base further up-ice somewhere under the Priestley Glacier branch of the NIS (Souchez et al., 1991).

3.2 Climate

Manuela weather station located on Inexpressible Island recorded an average air temperature of -14 ºC in 2016 and 2017. The maximum and minimum temperatures recorded during this period of time were 4.2 ºC and -39 ºC, respectively. The average wind speed recorded by Manuela Station was 24 km hr^{-1} with an average relative humidity of 55 %. The strong katabatic winds from the Transantarctic Mountains, ablate approximately 20 cm of ice per year across most of the NIS (Baroni et al., 1991). This ablation also removes snow and firn (compressed snow with a density between ice and snow) from the surface of the majority of the NIS.

3.3 Terra Nova Bay

Recent work has characterized the large-scale ocean circulation of the Victoria Land Coast, with focus on McMurdo Sound (Robinson et al., 2014), the DIT (Stevens et al., 2017) and the Terra Nova Bay Polynya (Cappelletti et al., 2010, Budillon and Spezie, 2000). These studies have revealed the presence of the Victoria Land Coastal Current (VLCC), which is hypothesized to carry a mass of buoyant ice shelf meltwater from underneath the western Ross Ice Shelf cavity northward underneath the ice shelves and tongues of the Victoria Land Coast. Vertical profiles of salinity and temperature by Stevens et al. (2017) indicated that the southern side of the DIT has observable haloclines and thermoclines but patterns are much less clear on the northern side, suggesting that the VLCC is partially deflected by the DIT (Stevens et al, 2017); therefore, it is unclear how much influence the VLCC may have on the NIS cavity.

Budillon and Spezie (2000) described the circulation in Terra Nova Bay as an intense north-easterly current along the coast from 55 m to 402 m depth with 40% of velocities greater than 15 cm s^{-1} and maximum velocities greater than 50 cm s^{-1}. Average ocean temperature in Terra Nova Bay in 1996 was -1.87 ºC at 140 m depth and -1.89 ºC at 400 m depth (Budillon and Spezie, 2000). Average ocean salinity in Terra Nova Bay during the same time period was 33.00-34.50 g L^{-1} at the surface and 34.82 g L^{-1} at 747 m depth. Oceanographic data collected by Manzella et al. (1999) also indicated relatively cold ocean water conditions in Terra Nova Bay, suggesting that vertical melt rates within the basal channel are likely to be small in comparison to the more widely documented basal channels of the Amundsen Sea sector. Terra Nova Bay has an estimated Rossby radius of 650 m (C Zappa 2017, personal communications).

There is little published information about the basal topography or ocean conditions of the NIS cavity. It is hypothesized that the oceanography of the cavity is extremely favourable for significant marine ice accretion in some locations under NIS due to the prevalence of marine ice at the adjacent Hell's Gate Ice Shelf (Frezzotti, 1997). Frezzotti (2000) estimated that the Reeves Glacier branch of the ice shelf loses 25% of its mass to basal melt, and approximated that mass loss from basal melt across the entire ice shelf equates to 4 Gt a^{-1}, which is in agreement with Budilion and Spezie (2000) who approximated a similar number based on ocean data in Terra Nova Bay, as a first order approximation of the cavity.

3.4 The NIS basal channel, surface depression and recent calving

A 30 km long surface depression runs east-west across the NIS along the suture zone of the Reeves and Priestly branches (Alley et al., 2016; Bell et al., 2017, Baroni et al., 1991; Dow et al., 2018). Within 20 km of the eastern ice shelf edge, this topographic depression is the surface expression of a 10 km wide basal channel (Dow et al., 2018). The strain regime experienced by the ice shelf surface has been shown to have driven the formation of a transverse crevasse across the width of the basal channel, first observed in a 1987 Landsat image (Dow et al., 2018). A surface river forms in this surface depression along the suture zone due to the impermeable nature of the ablated ice shelf surface and positive surface temperatures, since as early as 1974 and formed annually from 2014-2016 (Bell et al., 2017). The river has been observed to flow into the previously formed crevasse during the January to April melt season of 2014, 2015, and 2016, (Dow et al., 2018) as seen in Figure 3.4. In April 2016 full lateral expansion of the rift caused a 213 km^2 calving event (Bell et al., 2017) similar in size to a documented but unobserved mass loss event between 1963-1972 (Baroni et al., 1991).

Figure 3.4: Photograph of the Nansen Ice Shelf showing a surface river flowing into the rift in January 2014 with the Reeves Glacier in the background. Note the lack of snow or firn present on the surface. Taken by KOPRI (2016).

Chapter 4

Methods

The methods used in this thesis are primarily based on data from two radar systems that provided ice thickness and surface elevation measurements, as plotted in Figure 4.1. The two radar systems required different data processing workflows to calculate ice thickness values. In addition, surface ice velocity data products for the NIS were converted to strain rates. These data were used to produce DEMs/DITMs, strain rate maps, vertical melts rates, channel cross sectional area, and hydrostatic balance analyses. A crossover analysis compared the differences between adjacent ice thicknesses and surface elevations from different radar surveys to compute greatest possible errors for those ice thickness and surface elevation data sets. The work

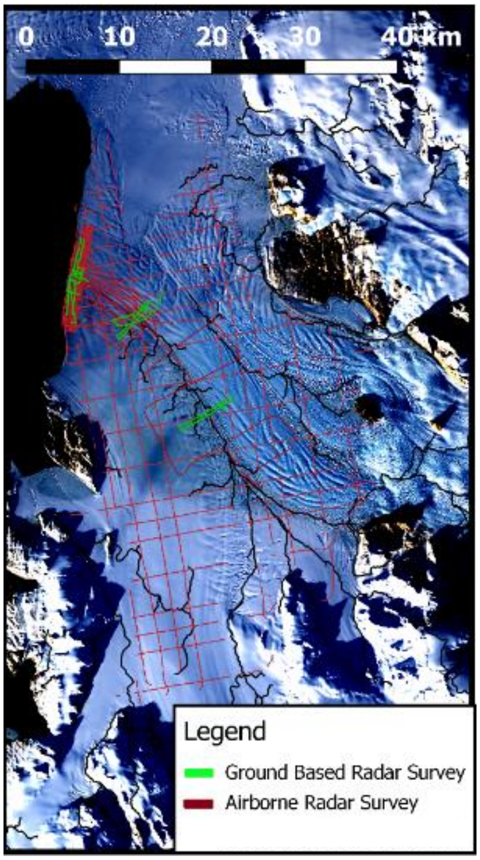

Figure 4.1: All radar surveys completed during the 2016/2017 Antarctic summer

described in this chapter was completed by the author, with the exception of field data collection, and some aspects of the airborne data processing workflow.

4.1 Radar systems

4.1.1 Ground based ice penetrating radar

From November 3rd to Nov 19th 2016, ground-based radar surveys were conducted by Dr. Christine Dow of The University of Waterloo and Dr. Derek Mueller of Carleton University. Operations were based out of Jang Bogo Station in collaboration with the Korean Polar Research Institute (KOPRI). The radar system (IceRadar, Blue Systems Integration, Ltd) consisted of two ski mounted sleds, a portable Embedded Processing Unit/receiver (EPU), a transmitter, a Topcon, Hiper V GPS receiver, a pair of 10 and 25 MHz antennas, antenna protection, and a ~40 m length of rope (Figure 4.2). The EPU was attached to the receiving antenna and was used to acquire, manage, and display radar data that were written as hierarchical data format (HDF) files. The IceRadar EPU allowed for one centre frequency at a time, and had an onboard GPS receiver that was supplemented with the mounted Topcon receiver. Most ground-based data used in this thesis were collected with a 10 MHz antenna, although initially some surveys were completed with a 25 MHz antenna. The change to the 10 MHz antenna was made in the field due to difficulty getting adequate returns from the ice-ocean interface with the higher frequency.

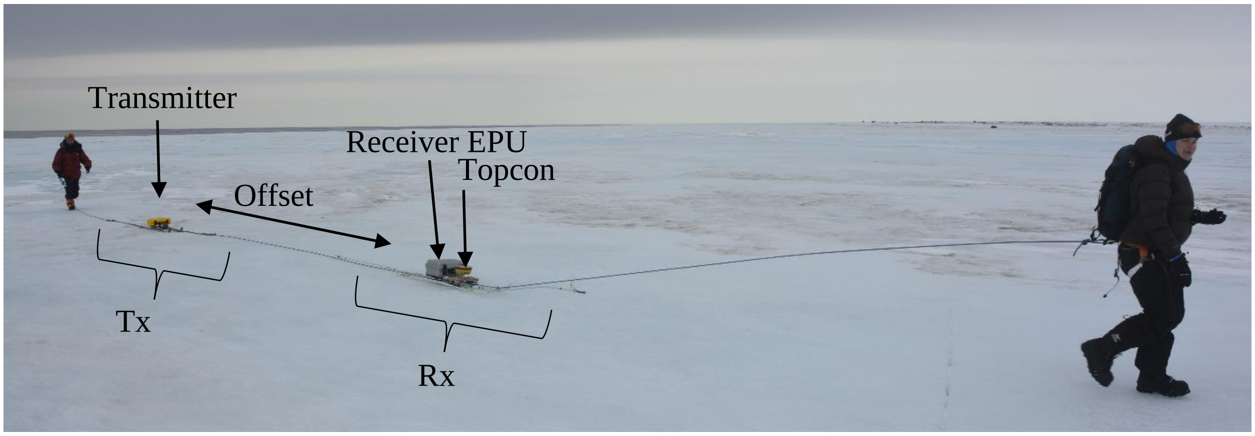

Figure 4.2: Field setup of ground based IPR system by Blue System Integration. Note the sled mounted radar transmitter attached the Tx, the Receiver EPU attached to the Rx, and the Topcon GPS receiver mounted to the front of the receiver sled. Photo by Derek Mueller (2016)

Three different sites along the length of the ice shelf channel, named site 1, site 2, and site 3, were targeted. The sites were spaced approximately 10 km apart, starting with site 1 at the ice shelf edge and then moving west towards the grounding zone (Figure 4.1). Radar lines within a survey were run both parallel and transverse to the channel with at least 10 intersections between these lines at any given site (hereafter called crossovers). The 10 MHz surveys were completed with a constant offset of 15 m between the Tx and the Rx and the 25 MHz with a constant offset of 9 m. Average linear spacing of ground-based radar data values, with attached surface elevations, was 4.1 m.

4.1.2 Airborne ice penetrating radar

From December 25th 2016 to February 18th 2017, personnel from the University of Texas Institute for Geophysics (UTIG) conducted a helicopter based airborne geophysics field survey based out of Jang Bogo Station. A radar system was installed on an Aérospatiale AS-350 helicopter in a fixed boom (Figure 4.3), and was complemented by a laser altimeter, camera, GPS, and an internal navigation system (INS) for precise positioning. The three mast fixed boom attached to the bottom of the helicopter contained two separate antennas, installed in a cross-track polarized dipole arrangement, that both transmitted and received independently, with 60 MHz centre frequencies, 15 MHz chirp bandwidths, and 1 µs pulse widths (Lindzey et al., 2017). Both antennas also had two receiver pathways for a low and high gain receiver, creating a total of four

Figure 4.3: Airborne radar system designed by UTIG and mounted on an AS-350 helicopter. The left and right boom contained the two independent pairs of radar antennas, the front boom was empty. Photograph by UTIG 2017 field participants.

traces for each radar data point. The NIS was surveyed on January 7th, 19th, 29th; February 6th and 13th. Surveys were flown between 300 m and 600 m above ground level. Average linear distance between radar data values for airborne data was 11.9 m and 13.0 m for the laser altimeter system.

Three surveys were targeted by UTIG: the NIS, NCH and NCH2 surveys. The NCH and NCH2 surveys were completed over the NIS basal channel within ~ 20 km of the ice shelf edge. The NCH2 survey contained 11, 8 km-long, parallel cross sections of the basal channel within 2 km of the ice shelf edge. Much of the spatial range in the NIS extent DEMs and DITMs (see section 4.3.1) was from the large-scale NIS survey. Two radar lines, one from an International Collaborative Exploration of the Cryosphere through Aerogeophysical Profiling (ICECAP) survey, in October 2011 and one from a Geophysical Investigations of Marie Byrd Land (GIMBL) survey in December 2014, crossed the NIS basal channel and were used to examine if there was significant vertical melt between 2011/ 2014 to 2016 by comparing ice thicknesses from those radar lines with the 2016 data.

4.2 Radar data processing

4.2.1 Ground based radar processing

RINEX files were downloaded from the mounted Topcon GPS receiver on the radar sled, PPP was performed using Natural Resources Canada’s (NRCan) online service. PPP resolves GPS measurements at the centimetre to decimetre scale with the use of precise orbital cloaks on GPS satellites and the real-time network of Global Navigation Satellite System reference stations to produce ellipsoidal heights (Kouba and Hèroux, 2001). Two reference stations, COTE and MCM4, are located near the Ross Sea and Transantarctic Mountains adjacent to the NIS field site (Blewitt et al., 2018).

Data from ground based radar surveys were downloaded as HDF files. Radar files were processed with a Python-based suite of scripts called Ice Radar Tools developed by Nathan Wilson (github ID: njwilson23/irlib), to analyze data generated by the IPR system. The location information associated with the onboard GPS was replaced, based on the time the location information was taken, with the more accurate PPP corrected GPS data. WGS84 Antarctic Polar Stereographic latitudes and longitudes were converted into UTM Eastings and Northings referenced to 71° S. The file was then saved after removing static GPS duplicates, blank traces caused by trigger failures, and stationary traces.

Radargram traces were picked using the ice_pick utility in Ice Radar Tools. For sections of poor radar return no interpretations were made and the bed reflection was given a place holder value to mark that section of the radargram. Once the picking was complete, the radar_join script was used to combine the picking files and apply antenna offsets. A wave velocity value of 170 m μs^{-1} was applied to calculate ice thickness for each trace (SOURCE). Figure 4.4 shows the complete ground based IPR workflow.

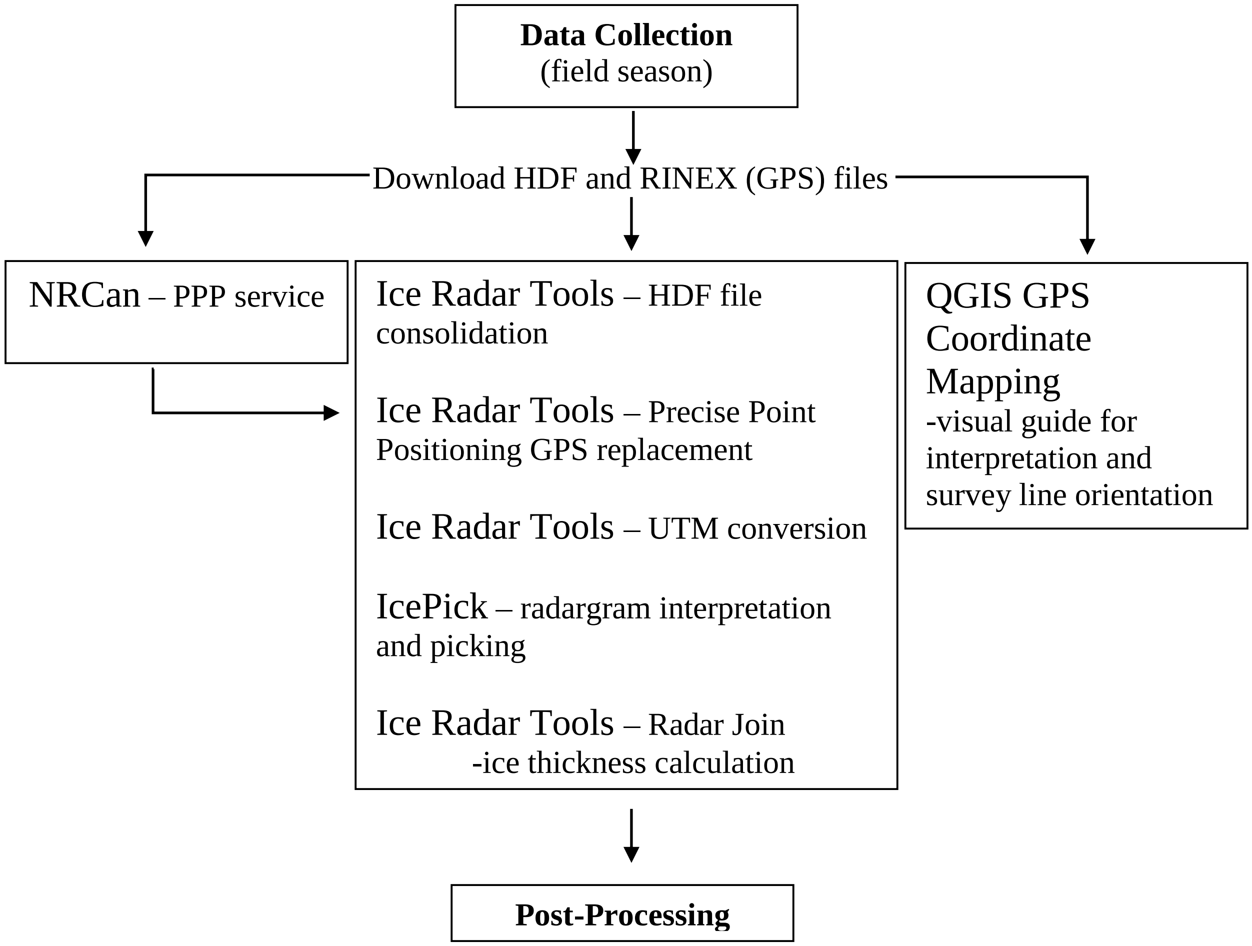

Figure 4.4: Data processing workflow for the ground-based IPR data.

4.2.2 Airborne radar processing

Airborne radar and surface data were downloaded in the field onto laptops with a custom software that produced pickable radar products by stacking and compressing the raw radar data

(Lindzey et al., 2017). These radar products required a computed solution to their spatial variables (time, latitude, longitude, and the helicopter's three dimensional orientation) before picking could begin. UTIG combined the GPS and INS data using the Novatel Waypoint software to attach the spatial information to the unpicked radar data (Lindzey et al., 2017). Access to the data and an in-house software was provided to the author to pick ~1000 km of radargrams at UTIG.

After initially picking the surface and bed, a series of iterative focusing algorithms were applied to the data to reduce the effect of diffraction hyperbolas. All radargrams were then re-picked with many of the diffraction hyperbolas removed or reduced, which aided identification of the ice-ocean interface. A v value of 169 m μs^{-1} (Carter., et al., 2007) was used to calculate ice thickness after which ice thickness, surface elevation and positional data was exported for further processing.

4.3 Data analysis

MATLAB was used to analyse ice thickness, surface elevation, spatial variables, and ice shelf velocity to display various aspects of the ice-ocean interface under the NIS. Ground-based and airborne data were converted from WGS ellipsoidal heights to orthometric elevations relative to the GL04C geoid datum, which is an approximation of mean sea level (Förste et al., 2008). A channel center datum-line was drawn down the basal channel center/apex with negative distances calculated to the south and positive distances to the north. The channel center datum and was subsequently used in all cross sections.

4.3.1 Digital elevation and digital ice thickness models

Three dimensional gridded models of ice thickness and surface elevation were computed using most of the processed radar data. Two different DEM extents, (the main NIS area and the basal channel area) were used to optimize the resolution of the digital models over the data dense basal channel area. The number of ground-based vs airborne data values for the main NIS extent and basal channel extent were ~18 000: 96 000 and ~18 000: 41 000 respectively. The ground-based and airborne data were interpolated onto grids in MATLAB using a triangulation-based natural neighbour interpolation, which was found to produce the most realistic product in comparison to the several other interpolation methods available. The number of grid cells in the two different extents were 2.7, and 4.0 million, with square grid cell sizes of 28 m and 10 m respectively. Ice thickness grids were subtracted from surface elevation grids to produce the ice draft DEMs. The DEMs and DITMs were clipped to exclude all measurements located over grounded ice, and exposed land masses surrounding the NIS were traced in a GIS software and exported as polygons to be displayed on the models for reference. The main NIS area excluded a ~30 km long, 400 – 1000 m thick section of the Priestley Glacier branch that extended to the grounding line because of low radar survey density and limitations with the gridding software.

Ice thickness and surface elevation data density were spatial variable in both DEM extents. Sections of the DEM extent with approximately equal densities were divided into three data density zones to provide qualitative levels of confidence for the interpolation in these sectors (Figure 4.5). Data density zones 1, 2 and 3, had a density of 618, 80 and 35 ice thickness values per km^2 respectively and 1305, 67, and 35 surface elevation values per km^2 respectively. Zone 1 was used to make sub-km scale observations of the channel and sub-channel morphology, zone 2 assisted with kilometer scale interpretation of ice thickness and ice shelf branch distribution, and interpretation of zone 3 was limited to large scale qualitative analysis of boundary conditions and areas of reduced ice supply.

4.3.2 Strain rates from Go-LIVE data

Ice velocity information was retrieved from the Landsat 8 derived Go-LIVE data base (Scambos et al., 2016). Feature tracking between two panchromatic Landsat 8 images taken at different dates to produce a ‘velocity image’, which quantifies the displacement of that ice over time using an automated algorithm (Fahnestock et al., 2015). Four Go-LIVE products were used: L8_063_113_288_2013_335_2014_258, L8_063_113_368_2014_258_2015_261, L8_064_113_272_2015_076_2015_348, L8_064_113_272_2016_063_2016_335 with observation spans of 258, 261, 348, and 335 days for the years 2013, 2014, 2015 and 2016 respectively. The ice shelf edge was the most problematic section of the ice shelf for velocity information likely due to the presence of concentrated surface drainage and proximity to open water. The best velocity information found in the Go-LIVE database for the NIS edge only

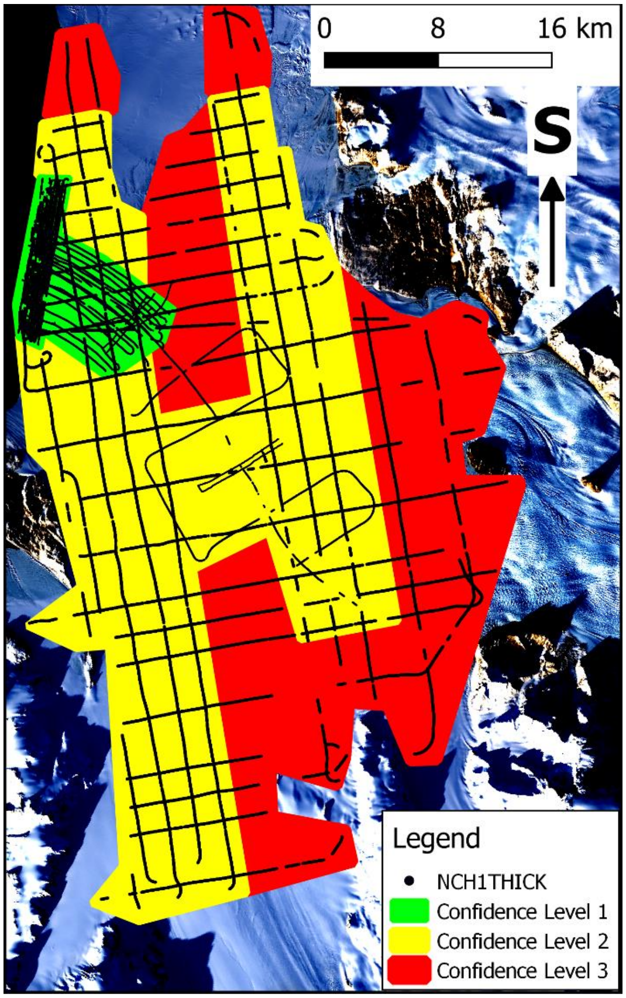

Figure 4.5: Sectors of confidence level within the main NIS extent. Confidence level 1, 2 and 3, have ice thickness data densities of 618, 80 and 35 ice thickness values per km^2 respectively.

covered 55% of the 11 NCH2 cross sections within 2 km of the ice shelf edge. Velocity data were converted into strain rates using equations 2.10, 2.11 and 2.12. Velocity and strain data were used from the four images as needed for the specific span of time required for the ice thickness change calculations in Section 4.3.3 and 4.3.4. Values were then interpolated onto radar data locations to assess the distribution and speed of spreading and thinning rates on the NIS. Vertical thinning values were two orders of magnitude smaller on average than changes in ice thickness between trackable features.

4.3.3 Vertical melt rate calculation over time

The 2011 ICECAP survey line over the NIS was considered in the planning of the ground-based 2016 radar survey. A ground-based survey line was repeated directly over the 2011 radar track as well as ~900 m down-ice of it, accounting for 5 years of ice shelf advection. Apexes and keels of the sub-channel features within the basal channel, as labeled in Figure 4.6, were tracked in ice draft cross sections and their ice thickness values were recorded. Using the equation

$$M_{5y} = (H_{11} - H_{16}) - \dot{\varepsilon}_{zzxa} \tag{4.1}$$

where M_{5y} is vertical melt over 5 years, H_{11} is the ice thickness in 2011, H_{16} is the ice thickness in 2016, and ε_{zzxa} is the vertical strain rate over x years in this location, 8 vertical melt rates and 8 changes in ice thickness were calculated across the channel.

The same method of tracking sub-channel features was employed for the 4 km long 2014 GIMBL survey line, which passed over the front of the NIS edge at an oblique angle to basal channel center. The 2014 survey, coupled with a repeat 2016 survey line provided four changes in thickness values over 2 years using Equation 4.1.

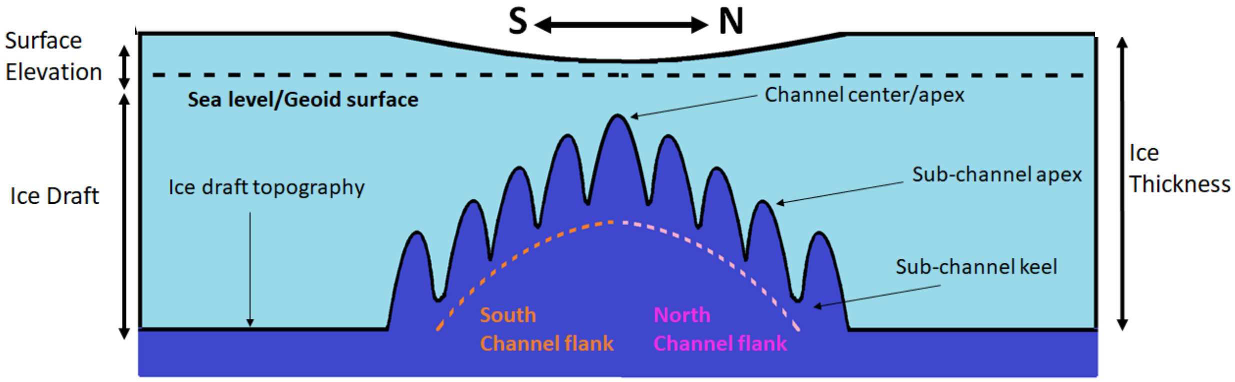

Figure 4.6 Simplified transverse-to-ice-flow cross section of a basal channel with terminology used throughout this thesis labeled.

4.3.4 Vertical melt calculation between cross sections

The 11 parallel cross sections of the NCH2 survey spanned the width of the main basal channel feature and were each spaced approximately 200 m apart within 2 km of the ice shelf edge. Apexes and keels within the sub-channel morphology were tracked using their ice draft between these parallel cross sections and then the associated ice thickness values were extracted. Vertical melt values resulting from ice-ocean interaction over a mean time of 3.1 years were calculated based on a space for time substitution, using the equation

$$H_{melt} = \left[T_{L(n+1)} - T_{L(n)}\right] - [\dot{\varepsilon}_{zz_{L(n+1)}} \times \frac{X}{V_{L(n+1)}}] \tag{4.2}$$

where: H_{melt} is vertical melt in m, $T_{L(n)}$ is the ice thickness of the down-ice cross section in m, $T_{L(n+1)}$ is the ice thickness of the up-ice cross section in m, $\dot{\varepsilon}_{zzL(n+1)}$ is the vertical strain in m a^{-1} of the up-ice cross section, X is the horizontal distance between the ice thickness values on L(n+1) and L(n) in m, and $V_{L(n+1)}$ is the velocity in m a^{-1} averaged from the Go-LIVE database over the number of years of interest (four in this instance). Using this method, distance between trackable features and the surface velocity of the ice was used to calculate the travel time between the tracked sub-channel features. The travel time for each melt value was multiplied by the average vertical strain in m a^{-1} experienced by the shelf in that location to remove the effect of vertical thinning from the difference in ice thickness between the two points. The mean time it took for a sub-channel feature to advect down-ice to the adjacent cross section was 3.1 years. Using equation 4.8, 180 changes in ice thickness were calculated.

Equation 4.2 assumes as the ice shelf advected a distance of ~200 m that: ice shelf velocity vectors were perpendicular to the cross sections, ice shelf velocities and vertical strain rates remained relatively constant, and that the basal channel morphology and sub-channel features within 2 km of the ice shelf edge were uniformly affected by an identical melt history, resulting in constant uniform changes in channel morphology.

Cross sectional channel area above an ice draft of 182 m below sea level was calculated for two NCH2 cross sections, 1.2 km apart, by integrating the area between their ice draft and this datum (Figure 4.7). The cross sections were chosen as far apart as possible within the NCH2 survey while still having good radar signal coverage. An ice draft of 182 m was used because it corresponded with the keel of the deeper cross-section (Figure 4.7b). The difference in cross sectional area was calculated using the same datum to remove the effect of net ice shelf melting, providing a more direct comparison of the change in size of the basal channel. Ice thickness cross sectional area was also computed for comparison.

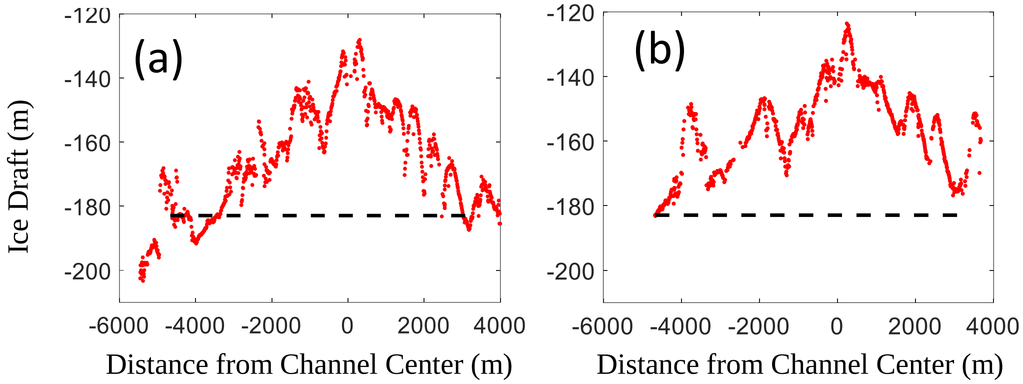

Figure 4.7: Ice draft cross sections and horizontal datum used to define the integration area for two NCH2 survey cross sections 1.2 km apart (a) ice draft cross section of the up-ice survey line NCH2 L10 (b) ice draft cross section of down-ice survey line NCH2 L4. Note that the datum line in panel (b) does not connect with the northern (positive x distance) keel

4.3.5 Hydrostatic balance models

To test the assumption of hydrostatic equilibrium, the surface elevations used in the DEMs were converted into hydrostatic equilibrium ice thicknesses, using the equation:

$$T_{HE} = \frac{S_m * \rho_{sw}}{\rho_i} \tag{4.3}$$

where: T_{HE} is hydrostatic equilibrium ice thickness in m, S_m is the measured surface elevation above the GL04C geoid in m, ρ_{sw} is the density of sea water (1025 kg m^{-3}; Budilion and Spezie, 2000) and ρ_i is the density of meteoric glacial ice (917 kg m^{-3}; Frezzotti, 1997). The hydrostatic equilibrium ice thickness was compared to the measured ice thickness using:

$$HB = T_m - T_{HE} \tag{4.4}$$

where: HB is hydrostatic balance in m, and T_m is the measured ice thickness in m. Equations 4.3 and 4.4 were used to compute DITMs as described in Section 4.3.1. Hydrostatic balance values returned by Equation 4.4 at or near zero indicate that the ice is in hydrostatic balance. Positive hydrostatic balance values indicate that the measured ice thickness is greater than what is predicted by the surface elevations, or alternatively that the surface elevations are depressed more than they should be for the thickness of ice. Negative values returned by Equation 4.4 indicates that the measured ice is thinner than it should be for the elevation of the ice surface, or that the ice shelf surface is being forced up through some physical process.

Equations 4.3 and 4.4 do not account for snow and firn accumulation on the surface of the ice shelf. A line was drawn across the NIS based on satellite imagery, which identified the border of the firn free and firn covered portions of the ice shelf. Interpretation of the hydrostatic imbalance of the NIS was confined to the firn free portions of the NIS due to uncertainties in firn density and thickness.

4.4 Errors

Sources of error that contributed to the precision of ice thickness and surface elevation measurements were separated into two categories: human error introduced during the interpretation of radargrams, and experimental sources of error introduced by the technical limitations of the methods used and the different wave velocities used in the ground-based and airborne datasets. Comparing the precision of data crossovers provided an estimation of the combined effect of human and experimental error in the measuring of ice thicknesses and surface elevations. Additional experimental error from the variability of tides and the large scale accuracy of the geoid model were also quantified, as they were not fully captured in the crossover analysis.

4.4.1 Crossover analysis

Ice thickness and surface elevation values were compared at crossovers that were less than 10 m apart between different surveys to assess the precision of the radargram picking as well as the precision of the surface elevation instruments. This crossover analysis produced a greatest possible error since value pairs at crossovers represented ice thickness or surface elevations at slightly different locations, and thus should not return a difference of 0.

The median absolute difference in ice thickness and distance between the data points at 546 crossover points was 4.24 m and 5.3 m, respectively. The 546 crossovers were between ground-based/airborne surveys as well as airborne/airborne surveys. The median absolute difference between surface elevations and the distance between those data points at 317 crossover locations was 0.83 m and 5.14 m, respectively. Figure 4.8 displays a histogram of these crossover values.

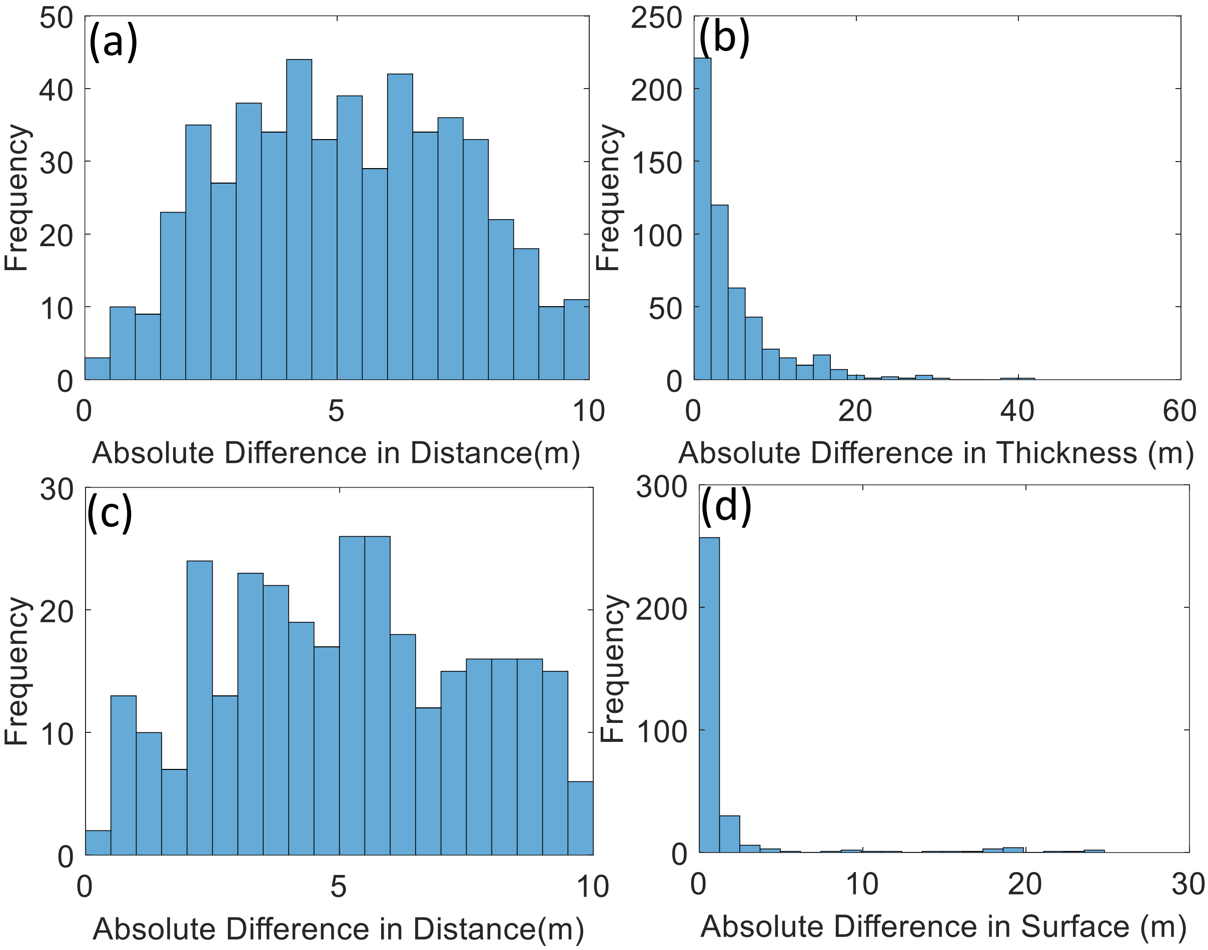

Figure 4.8: Histogram of differences in crossover pairs between different radar surveys, showing (a) the distance between 546 ice thickness crossover pairs and (b) the absolute differences in ice thickness of those 546 surface elevation crossover pairs (c) the distance between 317 crossover pairs and (d) the absolute differences in surface elevation of those 317 crossover pairs.

4.4.2 Sources of interpretive error

The two most prevalent interpretive difficulties in radargrams that contributed to the error determined from the crossover analysis were geometric scattering that produced diffraction hyperbolas and signal loss likely caused by marine ice. In the airborne dataset, diffraction hyperbolae were focused by UTIG operators, which significantly reduced them as a source of error. The heavily crevassed area up-ice of the Reeves and Priestley branch convergence zone generated full thickness rifts filled with marine ice (Kazendar et al., 2001), which appeared to cause loss of radar signal over small lengths of many radar surveys, similar to those observed by Holland et al., (2009). However, neither diffraction hyperbolas nor marine ice generated signal loss pervasive enough to inhibit analysis.

4.4.3 Experimental error analysis

The accuracy of GEOID models and the effects of the tides on floating ice shelves may have generated sources of error in the ice thickness and surface elevation data. The large scale vertical accuracy of the GL04C geoid model is estimated to have a greatest possible error of 0.15 m from average sea level at any given location (Förste et al., 2008).

The effect of tides was an important consideration for the accuracy of GPS measurements on the NIS. Terra Nova Bay has some of the smallest tides on the Antarctic coast (Padman et al., 2002). Hourly GPS measurements (provided by Ryan Walker, NASA) at 75.022 °S, 163.308 °E for over 72 days from November 2015 to January 2016 provided an approximation of the effect of tides on the NIS. Over this period sea level fluctuation was 0.46 m with a range in tidal height was from 0.11 to 0.82 m.

Total maximum potential error in ice draft calculations can be estimated by adding the independent errors in quadrature (Taylor, 1997):

$$e_{ID} = \sqrt{(e_{TM})^2 + (e_{SM})^2 + (e_{TR})^2 + \left(e_{geoid}\right)^2} \tag{4.5}$$

Where e_{ID} is the greatest possible error of any ice draft calculation, e_{TM} and e_{SM} are the errors of thickness and surface measurements respectively based on crossover analysis, e_{TR} is the error created by the tidal range in Terra Nova Bay and e_{geoid} is the large scale error of the GL04C geoid. Based on the previously stated average errors, the greatest possible error for ice draft values was found to be 4.36 m. Vertical melt rates calculated, as described in Section 4.3.3, which use differences in ice thickness over time have a greatest possible error calculated by:

$$e_{\Delta T} = \sqrt{2 * (e_{TM1})^2} \tag{4.6}$$

where e_{TM1} is the greatest possible error of ice thickness measurements as determined from the crossover analysis. The error in melt rate, $e_{\Delta T},$ (6.00 m), does not account for errors of the surface velocity derived vertical strain.

4.5 Experimental design limitations

The software used to pick and export the airborne radar data, as described in section 4.3.2, removed all parts of the radar line where ice thickness was not interpreted rather than using placeholders of ‘0’ or ‘NaN’, which prevented differentiating between no radar return versus unresolved diffraction hyperbolas from basal crevasses or steep ice draft topography. The missing radar data locations were manually repopulated for all airborne radar data and given ‘NaN’ placeholder values (Figure 4.9); however, it was still not possible to know why the segments of radar data were not picked. Areas of unpicked radar data were concentrated over: areas of known sea ice, down the channel center, at the ice shelf edge, near grounding lines, and in the firn-covered heavily crevassed area up-ice of the glacier convergence.

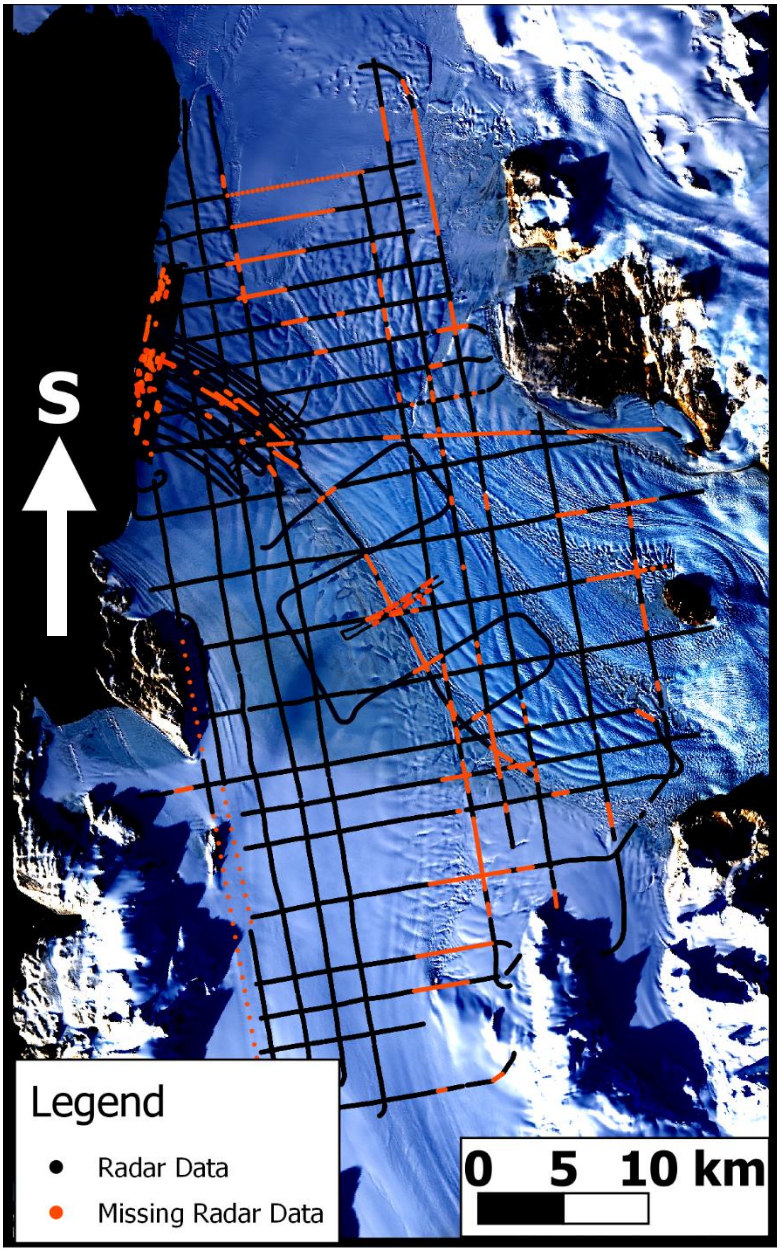

Figure 4.9: Map of the NIS with orange line segments indicating areas of missing radar data

Chapter 5

Results

In this chapter, surface elevation, ice thickness and surface ice velocity data are presented in the form of DEMs, DITMs and strain rate maps. These data are also used to estimate melt rates within the channel and patterns of hydrostatic imbalance experienced by the ice shelf.

5.1 NIS morphology

5.1.1 Digital elevation models and digital ice thickness models

Figure 5.1 is a map of all IPR survey data showing: the two areas used for the separate DEM/DITM extents, all radar data used in those extents, and the boundary between the firn-covered and firn-free portions of the NIS. The main NIS DEMs and DITM (Figure 5.2) provides a more detailed description of the NIS than the work from Frezzotti et al. (2000) provided in Chapter 3. The large-scale morphology of the NIS can be explained by following the three main branches of the ice shelf that determine the ice distribution from the tributary glaciers across the ice shelf as well as identifies areas of decreased ice supply.

There are three branches of the NIS: the southern Reeves Glacier branch, the northern Reeves Glacier branch, which diverge into two branches around the Teall Nunatak near the grounding line, and the Priestley Glacier branch. The southern branch of the Reeves Glacier was 450 m thick near the grounding line and thinned ~230 m over 27 km as it flowed south towards the NIS's southern edge near Larsen Glacier (Figure 3.1). The fast flowing northern branch of the Reeves Glacier (Frezzotti et al., 2000) was similar in ice thickness to its southern branch near the grounding line (450 m) but thinned 250 m over ~45 km towards the ice shelf edge. This branch of the Reeves Glacier was originally oriented east immediately after the grounding line then deflected towards the south-east after convergence with the Priestley Glacier branch ~15 km down-ice, orienting towards the east again after the southern Reeves branch curves away from it.

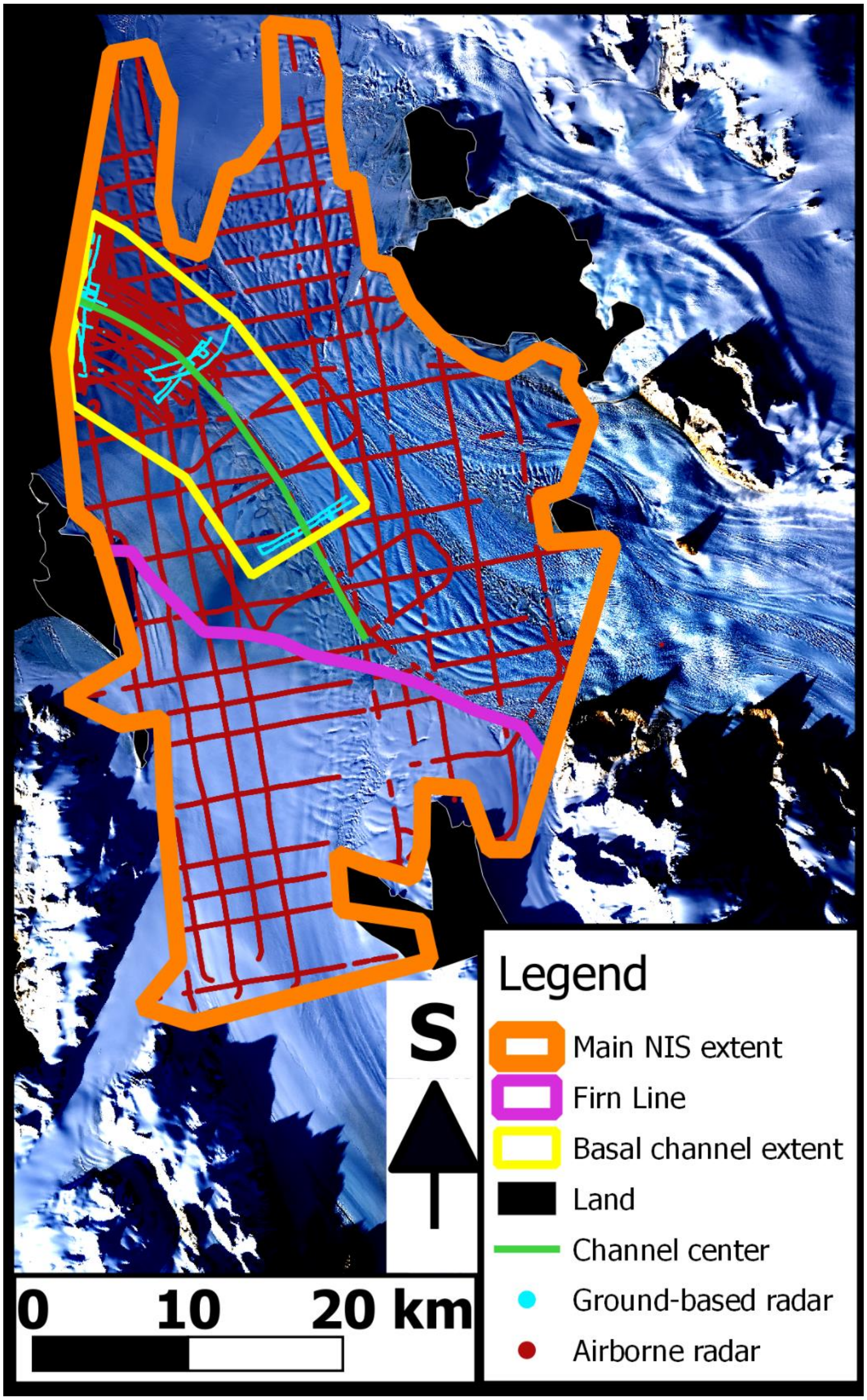

Figure 5.1: Map of the NIS showing the two extents of the DEMs/DITMs, and all the ground based (blue) and airborne (red) radar surveys used. The ice surface south of the firn line (purple), is firn free. Black polygons show the rock outcrops adjacent to the NIS.

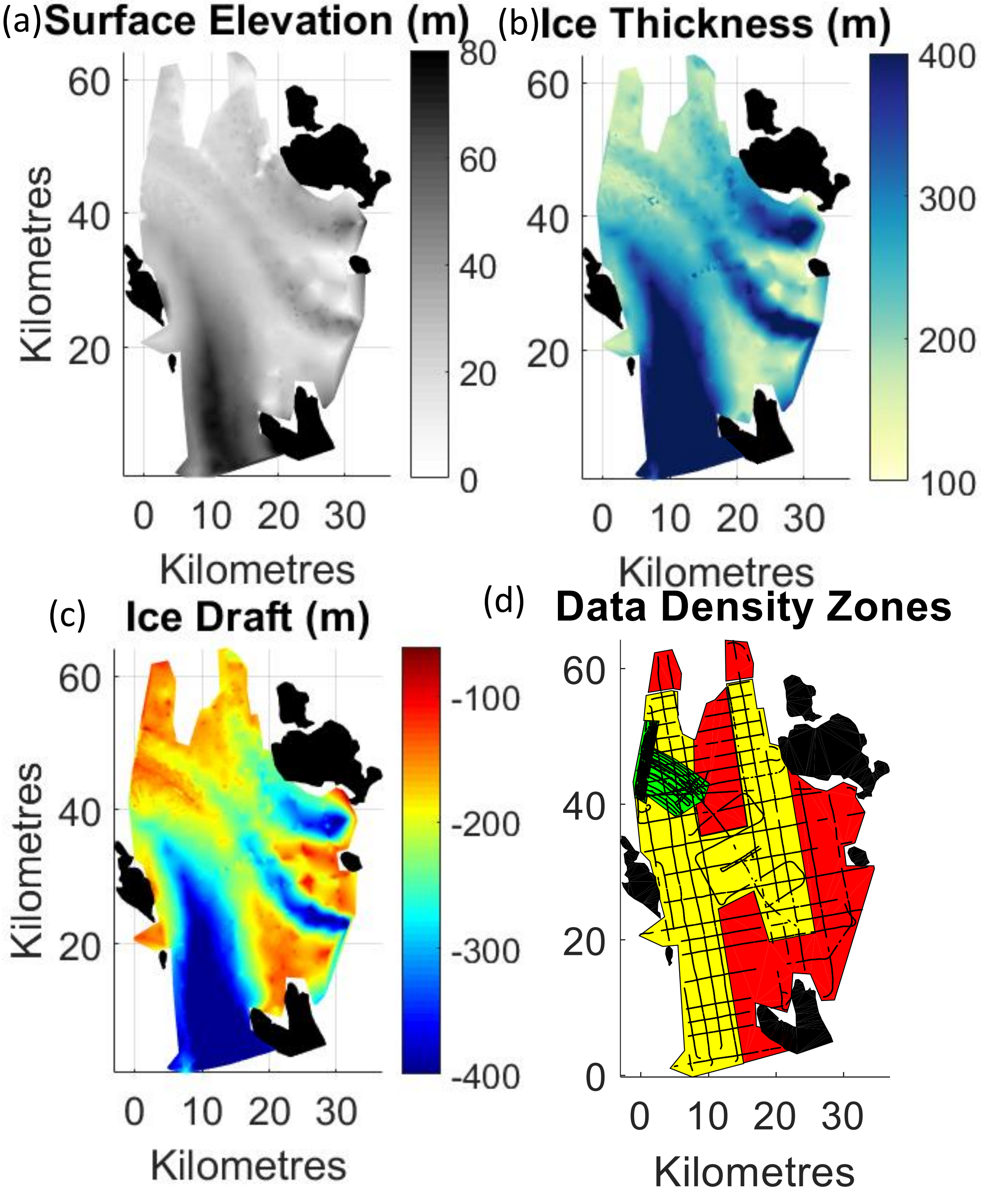

Figure 5.2: The main NIS extent DEMs and DITM. (a) surface DEM (b) DITM (c) ice draft DEM (d) data density zones. Black polygons represent rock outcrops adjacent to the NIS.

The grounding line of the Priestley Glacier (not shown in Figure 5.2) is located north of Figure 5.2's extent where it flows south down a narrow, 7 - 11 km wide, 30 km long corridor into the ice shelf bay. The Priestly Glacier branch was 645 m thick where it first enters the extent displayed in Figure 5.2 and it thinned by 370 m over ~ 45 km to the ice shelf edge. Approximately 100 m of this thinning occurred following the convergence with the northern Reeves Glacier branch over a distance of ~10 km. The thinning rates for the maximum ice thickness of each branch were approximately 8.5, 5.5, and 8.2 m km^{-1} for the southern Reeves, northern Reeves, and Priestly Glacier branches respectively.

There were four areas of thinner ice on the NIS (Figure 5.2): 1. The heavily crevassed zone up-ice of the Priestley and Reeves Glacier convergence, 2. A similar region on the down-ice side of the Teall Nunatak, 3. The southern ice shelf edge between the two divergent branches of the Reeves Glacier, and 4. The basal channel area in the suture zone down-ice of the convergence between the northern Reeves and Priestley Glacier branches. Area 1 was 150 – 200 m thick and was bordered by 400 m thick ice from the two adjacent branches. This area appeared similar in plan view to the basal channel area; however, it narrowed down-ice instead of widening without any discernible patterns or features as observed in the basal channel. Area 2, immediately down-ice of Teall Nunatak, was also 150 - 200 m thick and was bordered by ~400 m thick ice from the two Reeves Glacier branches. Area 3 at the southern edge of the NIS contained thin partly rifted sections of the ice shelf, held in place by sea ice. The presence of sea ice was determined by a lack of radar return, which clearly corresponded to observable boundaries in satellite imagery over the same area (see Figure 4.7). Area 4 is the basal channel which forms in the suture zone, 10 km down-ice of the convergence between the Priestley and Reeves Glacier branches. At the start of the suture zone the Priestley Glacier branch was 60 m deeper in ice draft than the northern Reeves Glacier branch (Figure 5.2 and 5.3). The formation of the basal channel began as the thinning/widening of this suture zone, where a continuous zone of relatively thin, 165 m thick ice, can be traced to the ice shelf edge where it thinned an additional 20 m (Figure 5.3). The basal channel and suture zone were observed to curve in plan view as the two branches were deflected east around Inexpressible Island (Figure 5.2).

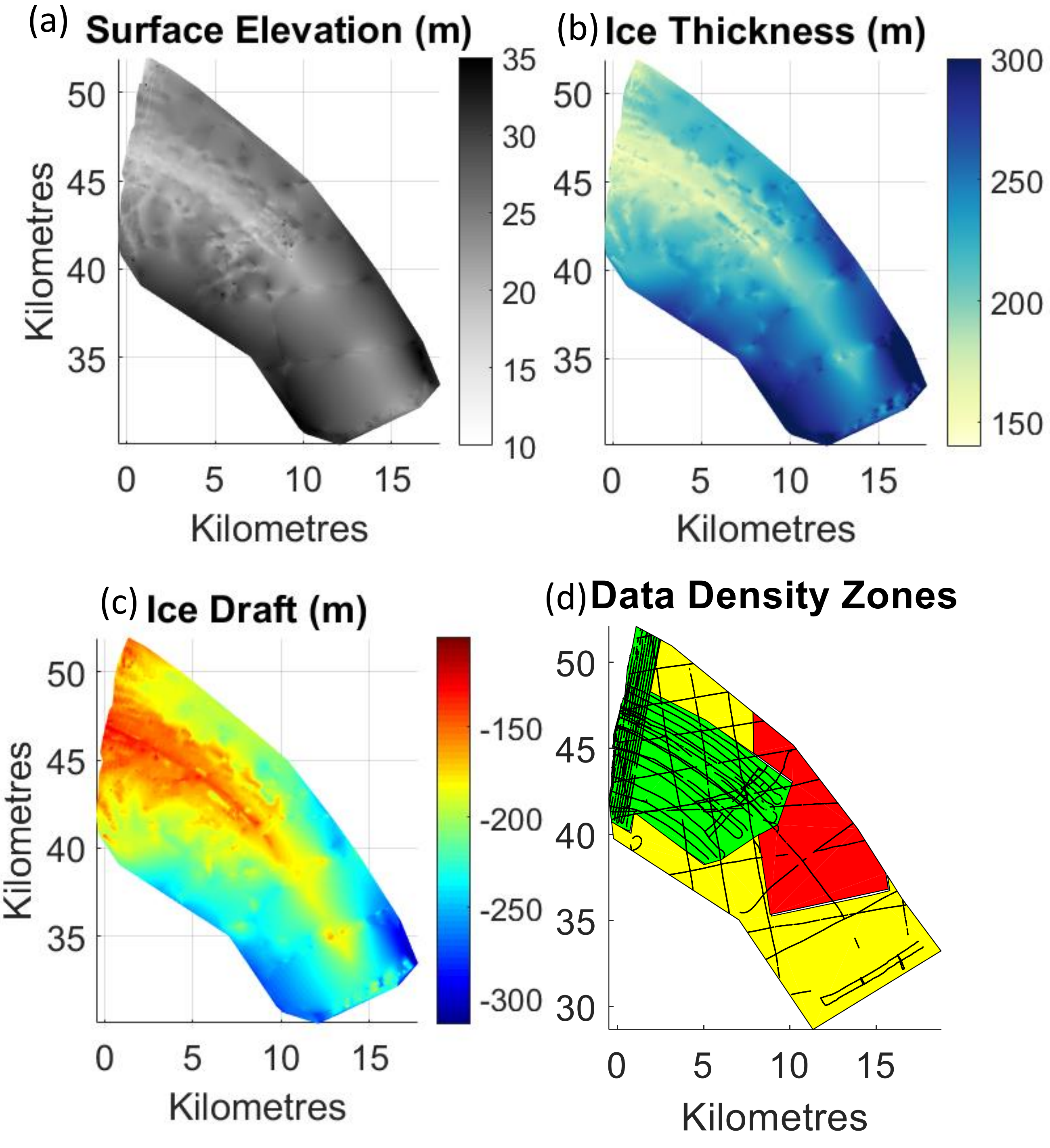

Figure 5.3: Higher resolution basal channel extent of (a) surface DEM (b) DITM (c) ice draft DEM. (d) data density zones

The higher resolution basal channel extent (Figure 5.3) had a mean spatial density of ~400 data points km^{-2} and more clearly shows the basal channel and discrete sub-channel feature within it. The basal channel was 4.5 km wide and had an apex height of 50 m at its start and then widened 10 km over its 15 km length with apex heights ranging from 90 m (as measured from the northern keel) to 60 m (from the southern keel). At its terminus, the northern flank of the channel was wider (6 km) than the southern flank (4 km) with an average slope of ~1.3˚ and ~1.1˚ at the ice shelf edge, respectively. Complex channel morphology consisted of many discrete semi-continuous features that were parallel, or oblique, to the continuous basal channel center (Figure 5.3c).

5.1.2 Sub-channels

Sub-channels are defined here as elongated basal channel features that sustain a two-fold increase in channel wall slope, are spatially continuous for more than 500 m in length and are ~500 m wide. These features, and the associated terminology used throughout this thesis are labeled in Figure 5.4 for reference. Shorter sub-channels were more irregular in their continuity and appeared to merge into larger sub channels nearer to the ice shelf edge. Sub-channel size and orientation relative to the basal channel center, were different on the northern and southern flanks. Southern flank sub-channels were consistently parallel to the main channel center, ranged from 15 - 25 m high and were ~500 m wide on average. These features were often discontinuous down their length, when one sub-channel segment ended another began but some offset, transverse distance away from it, as seen near 7.5 km and 45 km in Figure 5.4. These parallel sub-channels continued down the main channel length 1 to 1.5 km south of the channel center.

On the northern flank, the sub channels were also 20 m high and ~500 m wide but were 3 km to 5 km long near the ice shelf edge, and were oriented at an angle of ~ 40º from the primary channel center. The northern sub-channels were also semi-circular, curving northwards away from the channel center line, with those nearest the ice shelf edge curving to ~90º from their original orientation. The semi-circular sub-channels curved outward and away from the channel center in the ice draft DEM (Figure 5.3c) but in the surface DEM (Figure 5.3a) the same curved features appear more perpendicular from the main channel center line.

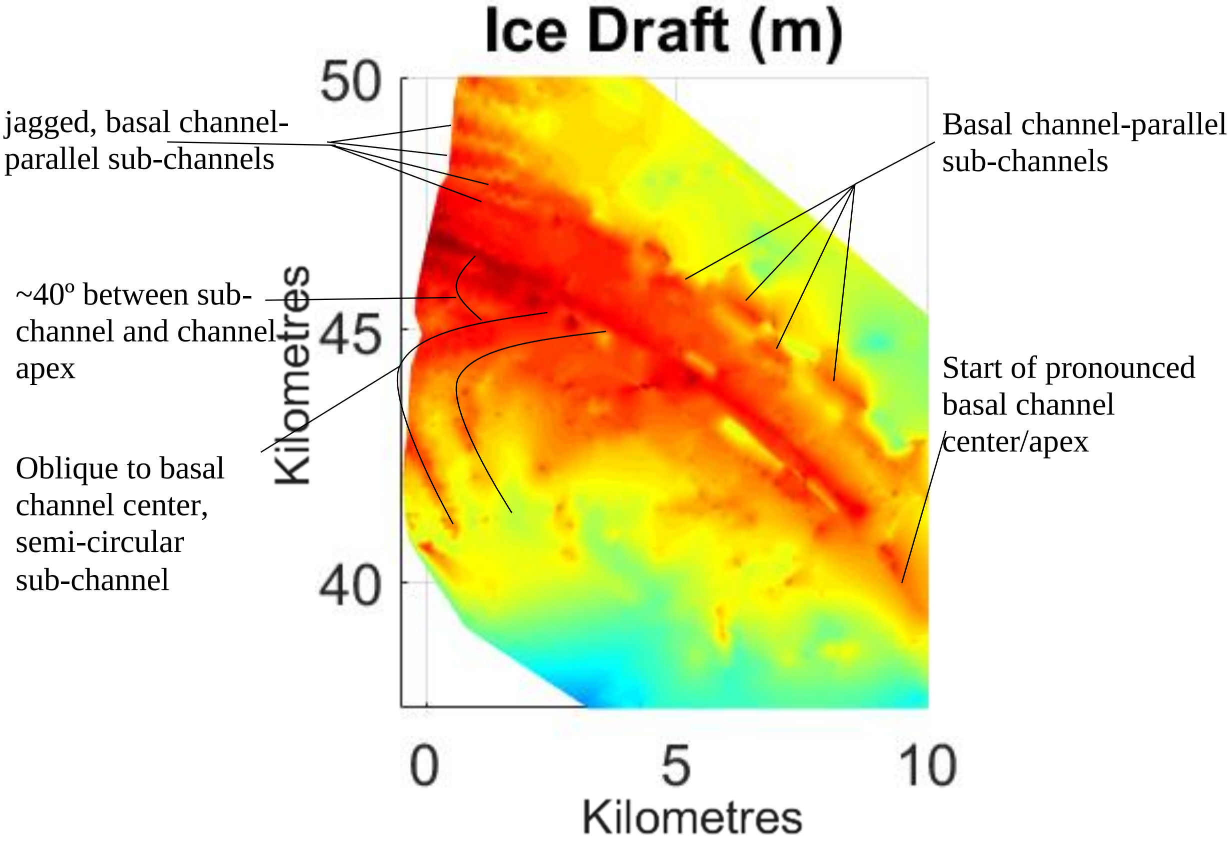

Figure 5.4: Annotated, zoomed in, ice draft DEM showing sub-channel features

5.2 Strain rates

Figure 5.5 shows strain rates derived from 2016 velocity vectors overlaid on the 2016/17 basal channel extent DITM. Missing coverage of strain rate vectors is likely due to cloud cover and surface water content during the image acquisition times. On either side of the channel center there were contrasting bands of continuous, parallel to channel center, strain rate vectors that were compressive on the northern flank and extensional on the southern flank (Figure 5.5b and 5.5c). The northern flank of the channel was characterized by curved bands of alternating extensional and compressive bands of strain that were oblique to the basal channel center, similar to the sub-channels that characterize the ice thickness of that flank. The continuous band of compressional strain in Figure 5.6 panels (a) and (b) indicates that the Priestley Glacier branch is compressed between the northern Reeves Glacier branch and Inexpressible Island. A continuous

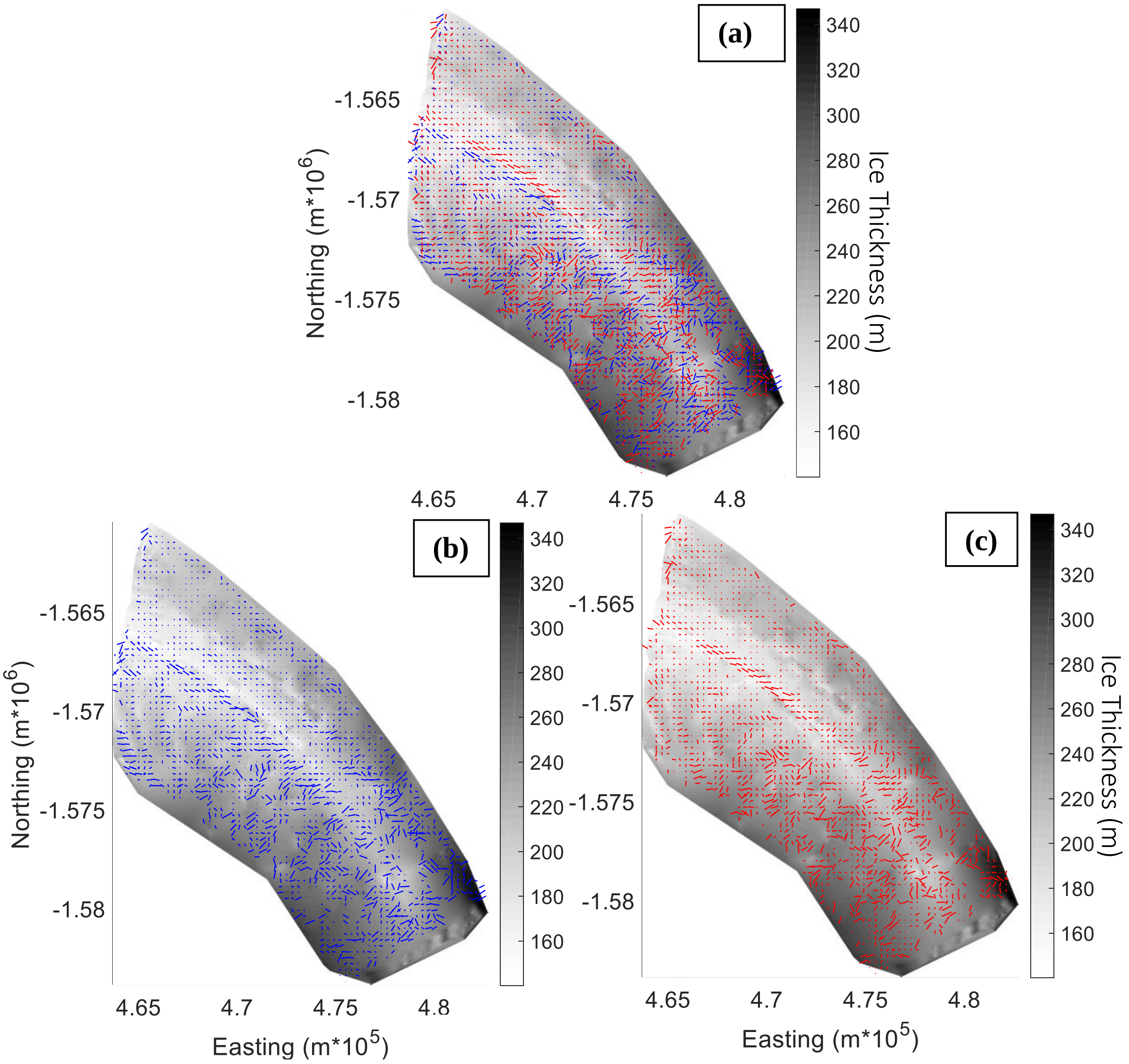

Figure 5.5: Go-LIVE derived 2016 strain rates, overlaid on the 2016/17 DITM with a) both compressional and extensional strain rate vectors, b) the compressive strain rate vectors and c) extensional strain rate vectors. The size of the vector indicates the relative magnitude of the strain rate at that location.

band of extensional strain on the south side of the suture zone suggests that the northern Reeves Glacier branch is less confined possibly because of the diverging southern Reeves branch. The southern flank of the channel, south of the continuous extensional band, has fewer observable small scale strain rate patterns in comparison to the alternating bands of the northern flank.

5.3 Melt rates and changes in ice thickness

Rates of ice thickness change had a heterogeneous distribution of positive values (indicating melt), negative values (indicating ice accretion), and uninterpretable values within the greatest possible error or uncertainty range of |6| m. For a change in ice thickness to constitute a melt or accretion rate, it had to account for the advection of the parcel of ice over time. Melt rates and changes in ice thickness were calculated over 5 years at ground-based site 2 and changes in ice thickness were calculated over 2 years at ground-based site 1 (Figure 5.6). Melt rates were also analysed between the NCH2 survey cross sections (Figure 5.6). Vertical strain rates, as analyzed from Go-LIVE data, were small in comparison to changes in ice thickness at the sites (Figure 5.7).

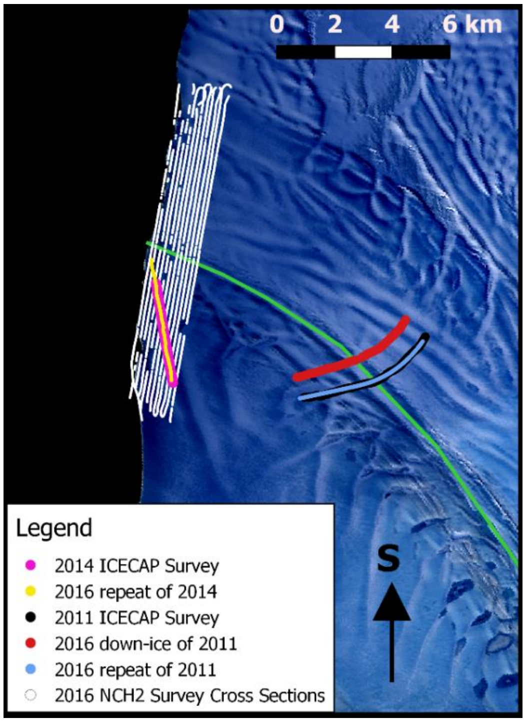

Figure 5.6: IPR survey lines used to calculate vertical melt and accretion

5.3.1 Melt rates and changes in ice thickness over time

The 2011 (black) and 2016 surveys (blue and red) at site 2 show the channel with several traceable sub-channel apexes and keels (Figure 5.8a). Ice thickness change between 2011 and 2016 at the same location (i.e., repeat survey, not accounting for ice advection) is shown in blue

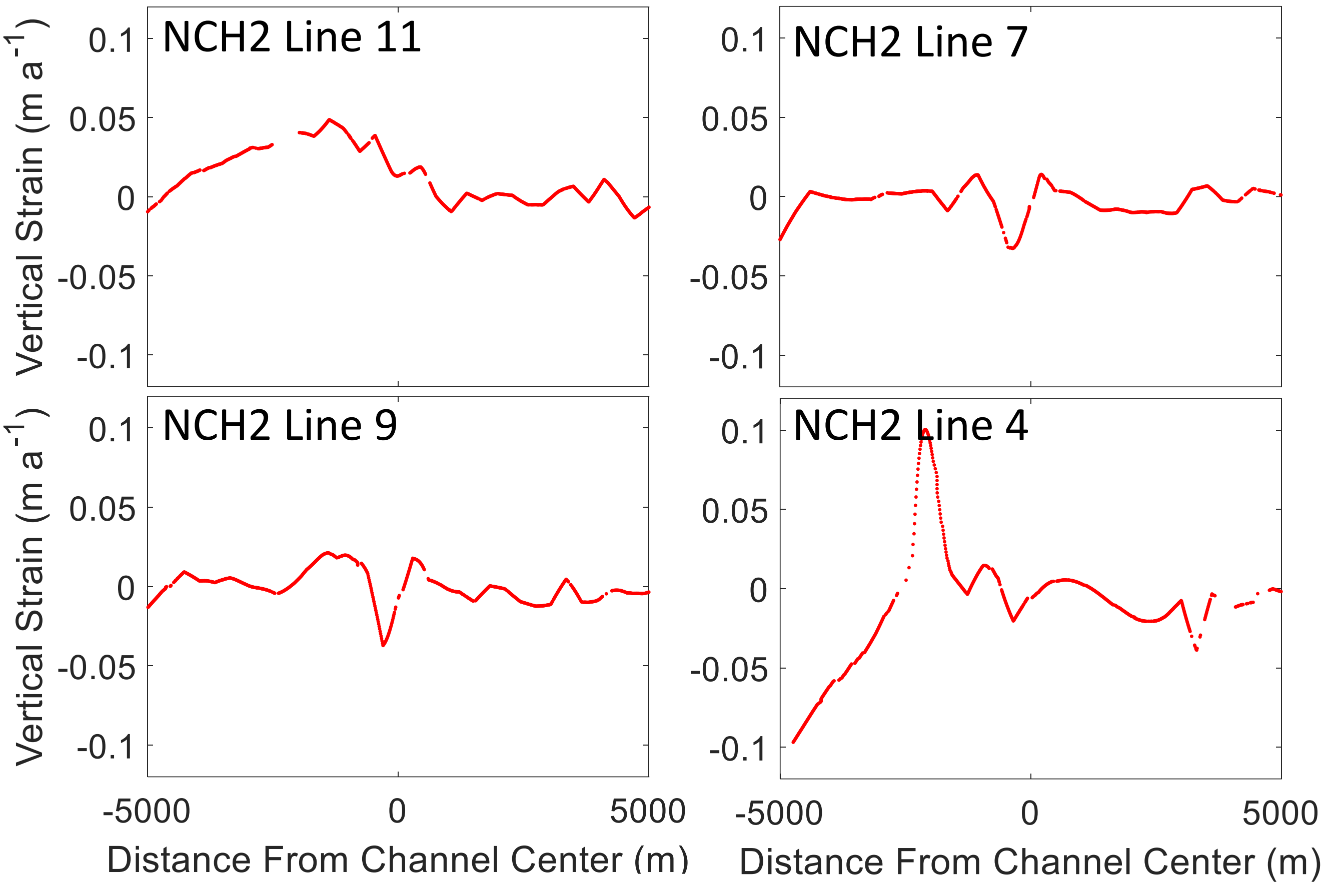

Figure 5.7: Vertical strain rates cross sections of select NCH2 Survey lines in m a^{-1} calculated from Go-LIVE surface ice velocities: (a) NCH2 Survey line 11, (b): NCH2 Survey line 9, (c): NCH2 Survey line 7, (d): NCH2 Survey line 4. Negative vertical strain values indicate vertical thinning.

in Figure 5.8b. Changes were positive (+14 m) over a sub-channel apex on the southern flank and negative (-9 m) over two sub-channel keels on the northern flank. Most of the changes in ice thickness between tracked features were within the range of error. The significant values suggest that the shape of the sub-channel features further away from channel center changed at these three positions over the 5-year period. The 2016 down-ice survey line (red), re-measured the same parcel of ice that was surveyed in 2011, accounting for advection, and was used to calculate vertical melt over 5 years (Figure 5.8c). Melt rates were positive, yet small, suggesting melt may have occurred in this location; however, they were mostly within the uncertainty range. One exception was a significant melt value of 11 m on the southern channel flank at a sub-channel apex that corresponded to significant positive change in ice thickness in Figure 5.8b. This may indicate that melt of that sub-channel increased over space or that these results are influenced by a change in sub-channel shape.

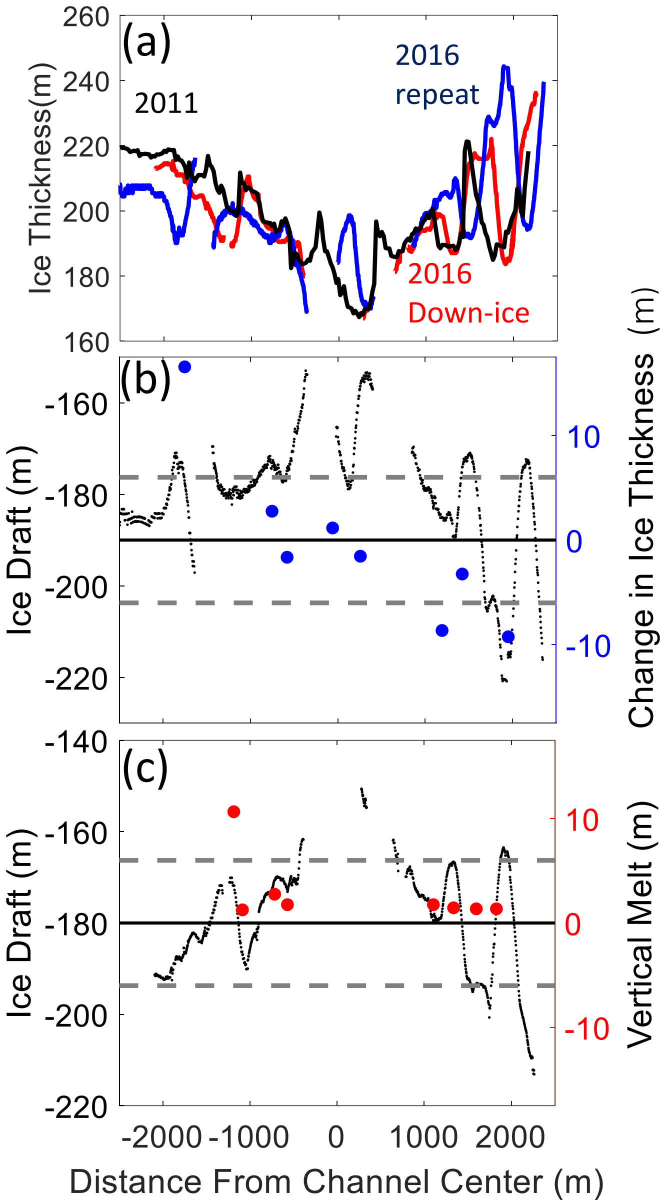

Figure 5.8: Melt rates and change in ice thickness from 2011 to 2016 at ground-based site 2 (a) ice thickness cross sections of 2011 ICECAP survey with the 2016 repeat (blue) and 2016 down-ice (red) survey lines (b) change in ice thickness over 5 years with 2016 repeat ice draft displayed in black to show the sub-channel feature associated with the melt value (c) vertical melt over 5 years with 2016 down-ice ice draft displayed in black. Grey dashed lines indicate the uncertainty of ± 6 m.

Figure 5.9 shows changes in ice thickness between apexes and keels of the 2014 (magenta) and 2016 (yellow) survey lines. Although the 2014 survey and 2016 repeat surveys were not cross sections of the main basal channel, they do provide a cross section of a sub-channel that ran oblique to the channel center. There were two features that did not change appreciably (less than |6| m) and two positive changes in thickness (9 and 13 m) nearer the main channel center. The former occurred at sub-channel keels, whereas the latter were found at sub-channel apexes. This pattern suggests that the apexes of these sub-channels incised significantly over the last two years.

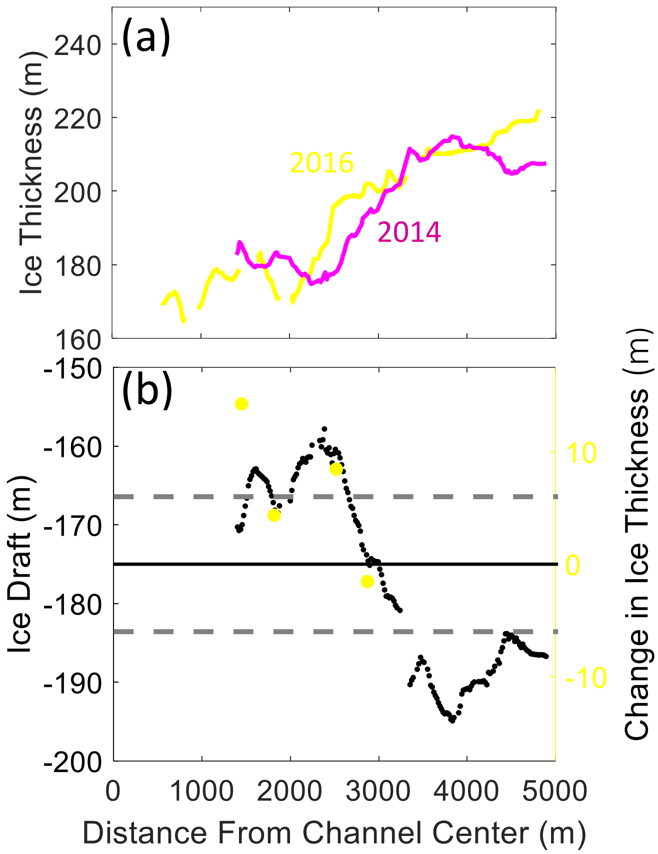

Figure 5.9: Change in ice thickness from 2014 to 2016 at ground-based site 1 a) ice thickness cross sections of 2014 GIMBL survey with the 2016 repeat (yellow) survey (b) change in ice thickness with 2016 repeat ice draft displayed. Grey dashed lines indicate the uncertainty of ± 6 m.

5.3.2 Ice thickness change between cross sections

Cross sectional basal channel geometry within 2 km of the ice shelf edge was moderately consitent between adjacent cross sections but was subject to significant vertical change over distances greater than 200 m, especially in the sub-channel features. The eleven parallel channel cross sections at the ice shelf edge (the NCH2 survey) produced 180 ice thickness change measurements at traceable features (Figure 5.10). Positive change, above 6 m, suggests melt occurred whereas negative values, below -6 m, are assumed to indicate accretion of marine ice was occurring. However, in both cases, interpretation of these results is subject to the assumption that the shape of the sub-channel features remained consistent across spans of 200 m and were only influenced by vertical melt, accretion, and thinning from vertical strain.

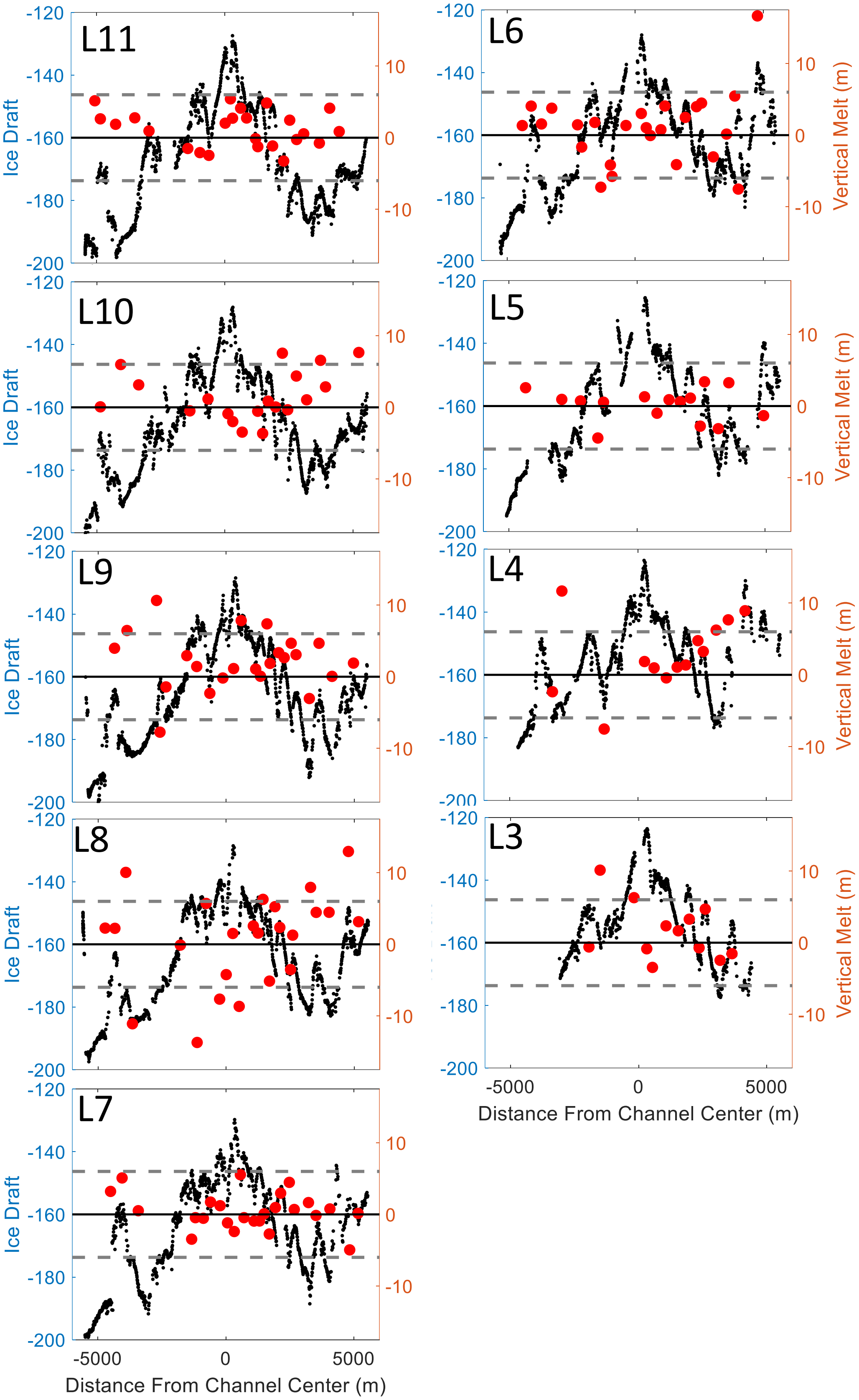

Figure 5.10: Vertical melt rates calculated using Equation 4.2 change in ice thickness and vertical thinning between apexes and keels of sub-channels across 11 parallel cross sections within 2 km of the ice shelf edge. Ice draft cross sections are displayed in black. Grey dashed lines indicate the greatest possible error of ± 6 mm for taking the difference of two independent ice thickness measurements.

Of the 180 ice thickness changes calculated, 154 of them were within the uncertainty range of |6| m leaving 18 positive (melt) and 8 negative (accretion) values. Of the 18 melt values, 11 occurred at sub-channel apexes and 7 were at sub-channel keels. There were 5 melt values greater than 10 m, 4 of which occured at sub-channels apexes. Significant melt was more prevalent further from the channel center with 11 values more than 2.5 km from the channel center. The northern flank of the channel had 13 of the significant melts values while the southern had 6. Melt rates may have been larger in the oblique components of the northern flank sub-channels since melt rates were most prevelant in the sub-channel apexes on the northern flank away from the channel center, which is in agreement with the significant ice thickness changes of Figure 5.9.

The 8 negative values, which suggest accretion of marine ice, were located evenly across sub-channel keels and apexes, while the two accretion values greater than 10 m occurred at sub-channel keels. Sigificant accretion was more prevelant near the main channel apex with only 2 values further than 2.5 km from the channel center. Six of the locations where accretion occurred were on the southern flank and only two were on the northern flank.Figure 5.11 shows the calculation of basal channel cross sectional area change between NCH2 survey lines 10 and 4. The basal channel cross-sectional area increased 27% from 163 660 m^2 to 208 613 m^2 over the 1.2 km and the number of sub-channels decreased from 10 to 7 (Figure 5.10a and 5.10b). The reduction in sub-channels was more pronounced on the northern flank of the channel where four subchannels reduced to two. Although vertical melt rates in Figure 5.10 tended to be within the uncertainty range between adjacent cross sections, channel growth is apparent over longer distances. The cross sectional ice area decreased by 4.5% from 1 438 510 m^2 to 1 375 715 m^2 (Figure 5.11c and 5.11d). The mean surface ice velocity along the 7.8 km wide NCH2 L10 survey was 62 m a^{-1}, which equates to a mean travel time of 19 years between the two cross sections. Using the ice thickness cross sectional difference of panels (a) and (b) (62 795 m^2), and incorporating vertical thinning rates, a mean vertical melt of 0.42 m a^{-1} is estimated for this 9.36 km^2 portion of the NIS basal channel.

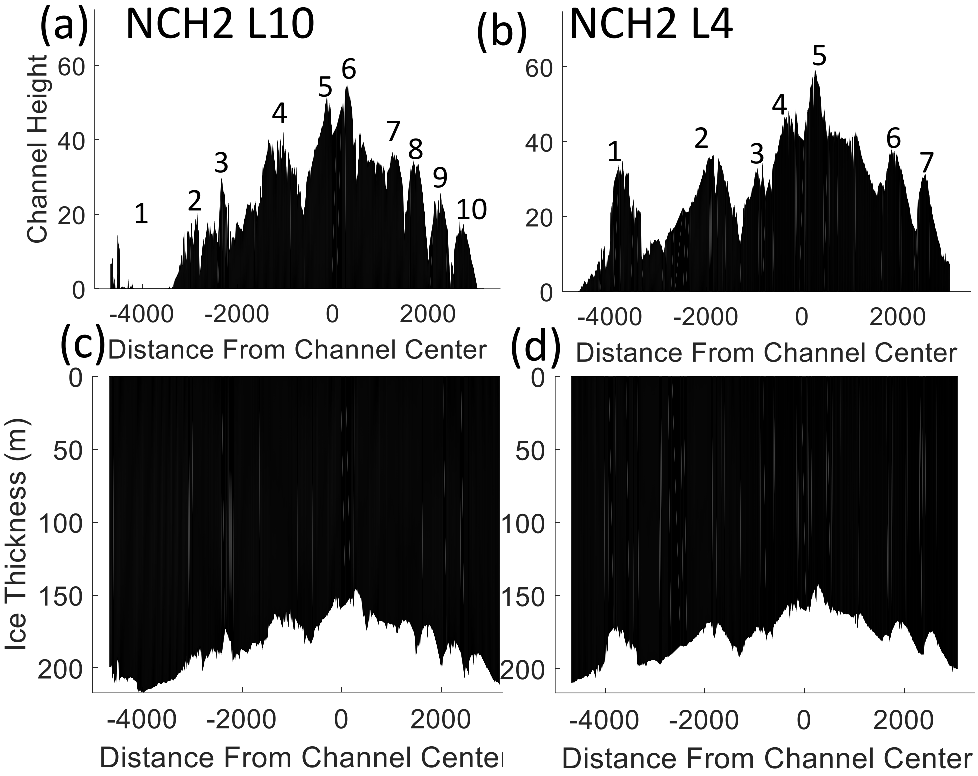

Figure 5.11: Cross sectional channel and ice thickness area between lines NCH2 10 and 4. (a) and (b) shows the up-ice and down-ice cross sectional channel area, (c) and (d) show the ice thickness cross sectional area. Note that the north keel of L4 does not make contact with the datum line and the channel area was extended as a result

5.4 Hydrostatic equilibrium

5.4.1 Large scale hydrostatic equilibrium

Figure 5.12 shows the measured ice thickness DITM for the NIS, the calculated ice thickness DITM (based on the assumption of hydrostatic equilibrium) and the difference between these DITMs. A net imbalance (red in Figure 5.12c) of -0.003 m per m^2 was calculated for the NIS (south of the firn line), suggesting that surface elevations, over most of this area, predicted thicker ice than was measured. Near the Reeves Glacier grounding line surface elevations were generally depressed (blue), small regions of hydrostatic balance were evident in the middle of the ice shelf and higher surface elevations (red) were found near the ice shelf edge in comparison to the thickness of ice measured at those locations. The convergence/suture zone between the Reeves and Priestley glacier branches was in quasi-hydrostatic balance in comparison to the rest of the ice shelf. The surface elevation up-ice of the Priestley and Reeves convergence, near the

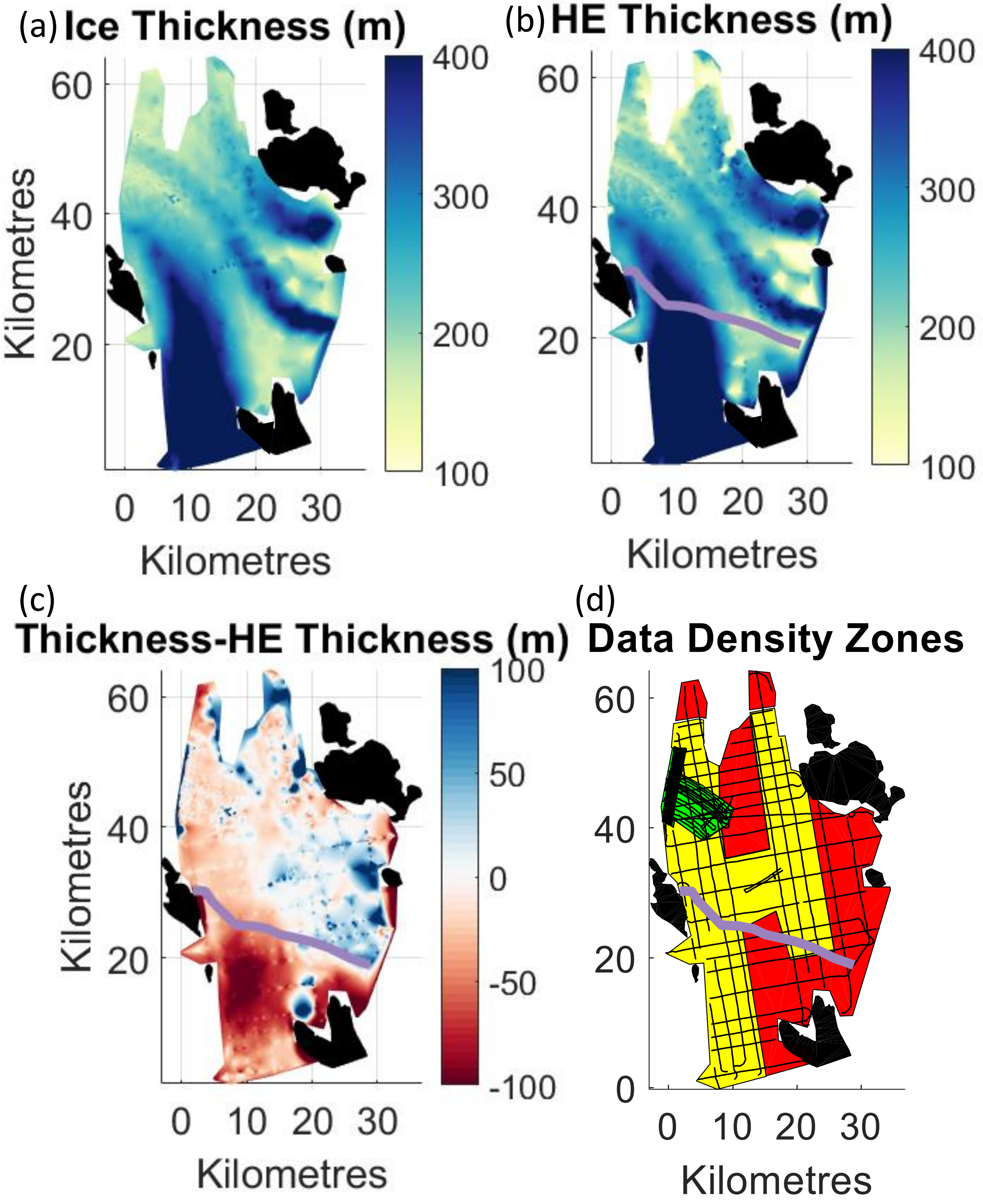

Figure 5.12: Main NIS extent hydrostatic balance DITMs (a) measured DITM (b) hydrostatic equilibrium DITM from inverted surface elevations (c) difference between measured and calculated ice thickness (d) data density zones for surface elevation values, zones 1 (green), 2 (yellow), and 3 (red) have data densities of 1305, 67, and 35 values per km^2 *respectively. Black polygons represent rock outcrops adjacent to the NIS.*

grounding line, predicted thinner ice than was measured (a positive imbalance, blue). A similar imbalance, caused possibly by depressed surface elevations, was seen down-ice of the Teall Nunatak.

Figure 5.13 shows the DITMs and hydrostatic imbalance for the NIS basal channel. The mean hydrostatic imbalance in this region is -0.12 m per m^2. A comparison between the net hydrostatic imbalance derived for the firn-free portion of the NIS and the basal channel area, shows that the basal channel area was a large contributor to the overall negative imbalance of the ice shelf. There are differences in ice thickness morphology between Figure 5.13a and 5.13b, whereby a more discrete and narrow basal channel/basal channel features are visible. In Figure 5.13b the perpendicular, curved sub-channels originate at a 90° angle from the channel center, whereas in Figure 5.13a the same features originate from a wider basal channel at angels closer to 40°. Small blue areas are visible near the channel center where the surface elevation under-predicted the thickness of the ice. This difference in the shape of the northern flank sub-channels between the two DITMs may have been the result of surface river erosion as these pockets were located along the channel centre where the surface drainage processes were active in recent years (Bell et al., 2017).

5.4.2 Hydrostatic equilibrium cross sections

Channel cross sections were plotted with their measured ice thickness and calculated hydrostatic equilibrium ice thickness in descending order with respect to distance from the ice shelf edge (Figure 5.14). The large scale trends in hydrostatic equilibrium from the grounding line to the ice shelf edge, as described in Figure 5.12, are reflected in Figure 5.14. Site 3 surveys showed depressed surface elevations, which produced positive hydrostatic imbalances and then, nearer to the ice shelf edge, the NCH2 surveys had progressively more elevated surface elevations (measured ice was thinner than predicted), which produced negative hydrostatic imbalances. The surface elevation often captured the large-scale geometry of the channel morphology, however small features (less than 350 m wide) were less likely to be represented via hydrostatic equilibrium calculations. Where there were large contrasts in ice draft topography over distances of a few hundred metres, narrow features were less likely to be represented by elevation data even if they then exceeded 350 m in width. Locations where surface elevation best predicted ice thickness was in the sub-channel apexes (ice thickness minimums).

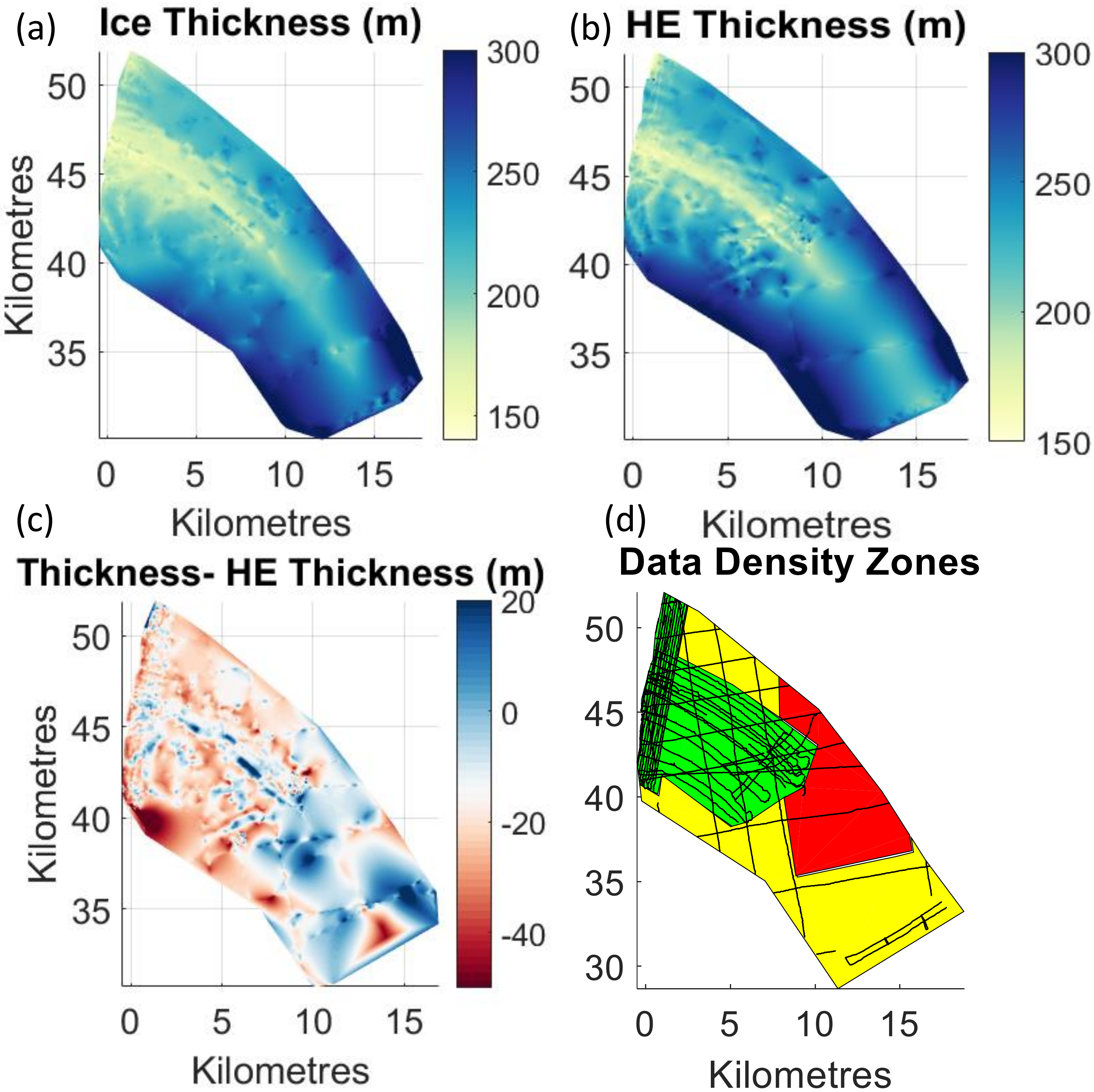

Figure 5.13: Higher resolution basal channel extent of the hydrostatic balance DITMs (a) measured DITM (b) hydrostatic equilibrium DITM from inverted surface elevations (c) difference between measured and calculated ice thickness d) data density zones for surface elevation values, zones 1 (green), 2 (yellow), and 3 (red) have data densities of 1305, 67, and 35 values per km^2 respectively

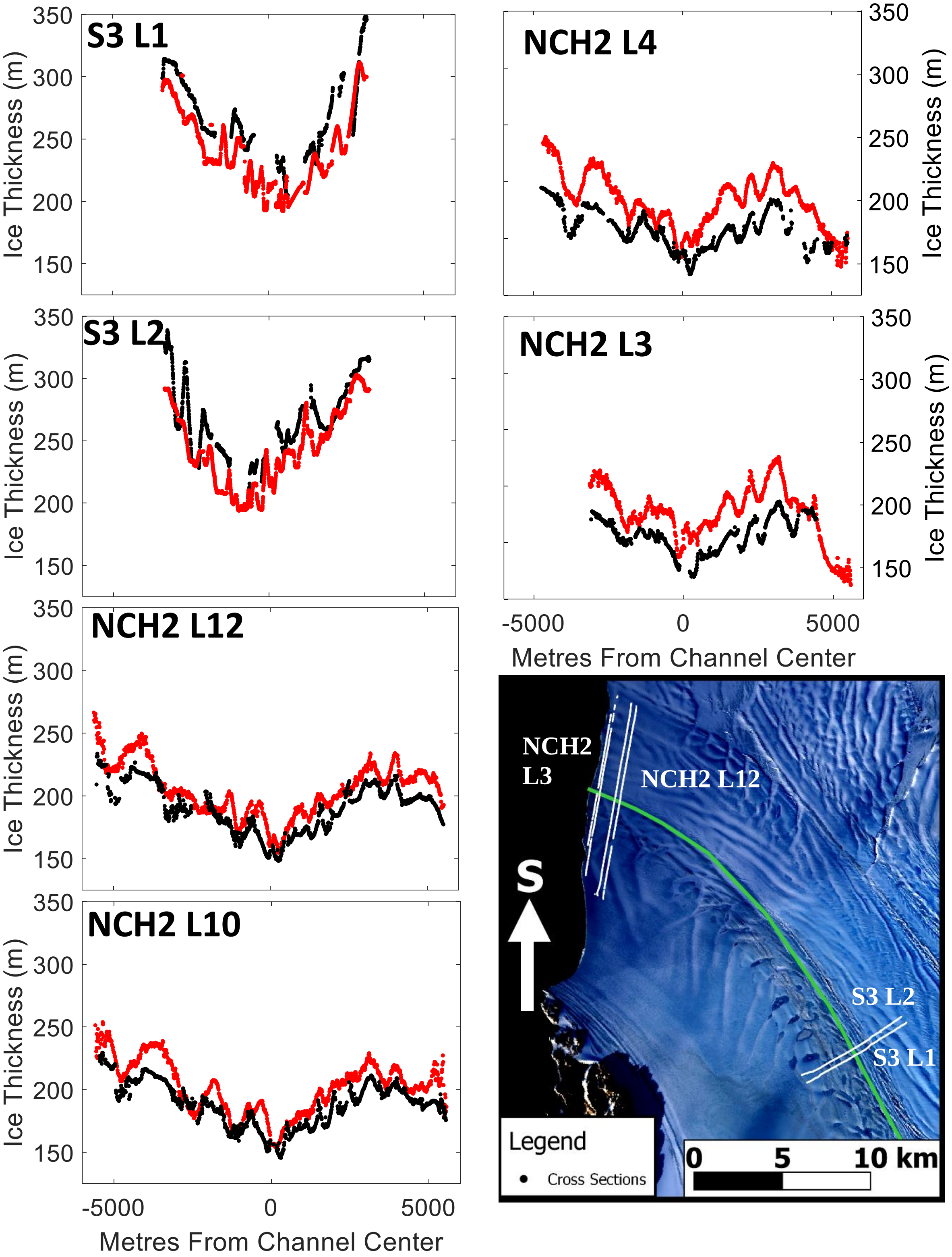

Figure 5.14: Select channel cross sections showing ice thickness (black) and hydrostatic equilibrium ice thickness from inverted surface elevations (red) and an index map for the location of these cross sections.

Chapter 6

Discussion

The Antarctic holds the majority of the global water equivalent capable of contributing to future sea level rise (DeConto and Pollard, 2016). The ice shelves that fringe the continent play a critical role in holding ice mass, on the continent through the buttressing force that they exert on grounded ice (Dupont and Alley, 2005). The oceans and atmosphere around the Antarctic are warming, causing a change in wind patterns, which delivers warm water to ice shelf cavities (Pritchard et al., 2012). Basal channels have been found under many Antarctic ice shelves and are correlated with the presence of relatively warm ocean water (Alley et al., 2016). Incision into ice shelves from basal channel melt drives ice shelf surface elevations down over these features as they move towards new hydrostatic equilibriums. Contrasting ice thickness and depression of surface elevation has been shown to produce characteristic sets of surface and basal crevasses (Sergienko, 2013; Vaughan et al., 2012), and these crevasses have been observed to be susceptible to interactions with surface melt water contributing to large calving events (Dow et al., 2018). In order to assess the effect, that the basal channel has on the stability of the NIS, the data in this thesis will be discussed in terms of large-scale ice shelf features, basal channel characteristics, and small-scale sub-channel morphology.

6.1 The NIS morphology and hydrostatic balance

6.1.1 Distribution of ice thickness and draft

The three branches of the NIS are centered on sinuous tracks of ice thickness maximums and are bounded by corresponding ice thickness minimums (Figure 5.2); one consists of ice from Priestley Glacier and the other two are branches from the Reeves Glacier. This description fits well with the most recent published physical surveys of the NIS that described ice thickness of the three NIS branches and ice flux at the grounding line (Frezzotti et al., 2000). Based on measurements taken from Figure 5.2 the southern, middle, and northern branches had contrasting thinning rates of 8.5, 5.5 and 8.2 m km^{-1}, respectively. This may be due to their different velocities and subsequent residence times in the NIS, differing ice drafts at the grounding line, and spatially variable ocean conditions in the ice shelf cavity. Areas of contrasting ice thickness across the NIS appear largely controlled by ice supply at the grounding line. Four areas of relatively thin ice (less than 200 m) occur on the NIS, three of which can be attributed to this reduced ice supply. Downstream of the Teall Nunatak between the divergent branches of the Reeves Glacier there is a heavily crevassed region (Khazendar et al., 2001). The thin and crevassed nature of the ice there is likely caused by divergent flow around the Teall Nunatak creating an area of poor ice supply on the down-ice side of the feature and may also be influenced by hidden portions of the Teall Nunatak under the ice surface. A second area of thin ice is located between the Priestley and northern Reeves Glacier branches, which narrows then ends shortly after convergence between the two. This heavily crevassed area, surrounded by landmass at the grounding line, is without any significant ice supply. Full thickness marine-ice layers were likely generated in these first two areas by rifts near the Reeves Glacier grounding line that filled with melt water, froze, and advected down-ice. This is corroborated by a confirmed surface marine-ice sample at ground-based site 3, over the suture zone, down-ice of this crevassed area, and by Khazendar et al. (2001). The third area of thin ice is located at the southern ice shelf edge where the two branches of the Reeves Glacier diverged, leaving thin sections of calved ice held in place by sea ice that connect to the Larsen Glacier and DIT.

The NIS basal channel, the fourth area of anomalously thin ice, is the only one that actively thins along its length, and can not be explained by the distribution of ice over the grounding line or divergent velocity vectors between the branches of the NIS. Good ice supply and a lack of divergent branch velocities suggests that the basal channel area actively thins from basal melt. The basal channel initiates ~30 km from the grounding line and widens down its length indicating that it is ‘ocean-sourced’, based on the characteristics of basal channel classes as defined by Alley et al. (2016). The DEM and DITMs of Figure 5.2 show the basal channel growing from mid-ice shelf to the ice shelf edge within the suture zone. Dow et al. (2018) suggested that the NIS surface river became concentrated in the surface depression that formed because of this ocean-sourced basal channel.

6.1.2 NIS hydrostatic imbalance

The majority of the NIS is out of hydrostatic equilibrium south of the firn line as seen in Figure 5.11c by an average of -0.003 m m^{-2}. The net negative imbalance experienced by the ice shelf may indicate that the glacial ice density value used in equation 4.3 was too low, however the average imbalance is close to zero (~ 0.003 m m^{-2}) and well below the greatest possible error for both surface elevation and ice thickness measurements that the equation uses. Negative imbalances suggest that either: the ice surface elevation was being held up artificially, the measured ice thickness underrepresented the true thickness of ice, or the real density of the glacial ice was greater than the value used. Hydrostatic imbalance pertaining to the presence of the NIS basal channel is discussed in Section 6.2.

Predictions of significant marine-ice production under the NIS (Tison et al., 1993) indicates that the large scale negative hydrostatic imbalance observed on the eastern half of the ice shelf could have been caused by vertical marine-ice accretion in thick layers. In order for the 10-20 m of negative hydrostatic imbalance observed across this part of the NIS to be caused by undetected marine-ice, the radar returns in both the ground-based and airborne data would have to have been consistently picking a Marine-Meteoric Ice Reflection (MMR). In this scenario, the conductivity contrast between meteoric ice and wide spread marine-ice layers at the base of the ice shelf was great enough, without any gradual changes in the internal layering of those marine ice layers, that the radar returns were returned off of a strong and clear MMR and then subsequently attenuated in the marine ice layer to prevent secondary returns from the ice-ocean interface.

Blindow, (1994) and Kulessa et al., (2014) were able to identify MMR using 40 and 50 MHz IPR surveys under Filchner Ronne and the Larsen C ice shelves respectively. In these surveys, the strongest reflections were the ice-ocean interface but this higher frequency radar data provided information on ice layering, including observable MMRs. The ground-based 10 MHz frequency used near the NIS edge did not reveal ice layering within isotropic meteoric ice or provide any discernible MMR. The lack of an MMR could have been caused by a change in wave propagation from a displacement wave to a diffusive current as a function of the low frequency used and the higher conductivity of marine-ice, as explained by Equation 2.7, which would not have affected the higher frequencies used by Blindow, (1994) and Kulessa et al., (2014) as much.

There were sections of radargrams where signal return from the ice-ocean interface was weaker or returned no reflection, providing evidence of marine-ice accumulation, but it was not a wide-spread phenomenon. Areas of signal loss were in short linear sections of some radargrams as seen in Figure 2.8, suggesting the presence of narrow, linear marine-ice filled crevasses as documented by Khazendar et al. (2001). If the large-scale negative hydrostatic imbalance was caused by basal marine ice accumulation, it would have to exhibit different behaviour compared to the relatively thin stripes of marine ice filled rifts identified by the lack of radar returns, which had no indication of a discernible MMR. As such, the air-marine ice interface appeared to cause diffusive electromagnetic behaviour and, if there was a widespread basal meteoric marine-ice interface, it instead produced significant reflections consistently, without attenuating any of the 10 MHz frequency radar waves (Figure 6.2). Considering that this negative imbalance is most prominent in the area of enhanced melt (the basal channel) it seems unlikely that significant marine ice accumulation is the main cause of the 10 – 20 m negative hydrostatic imbalance there.

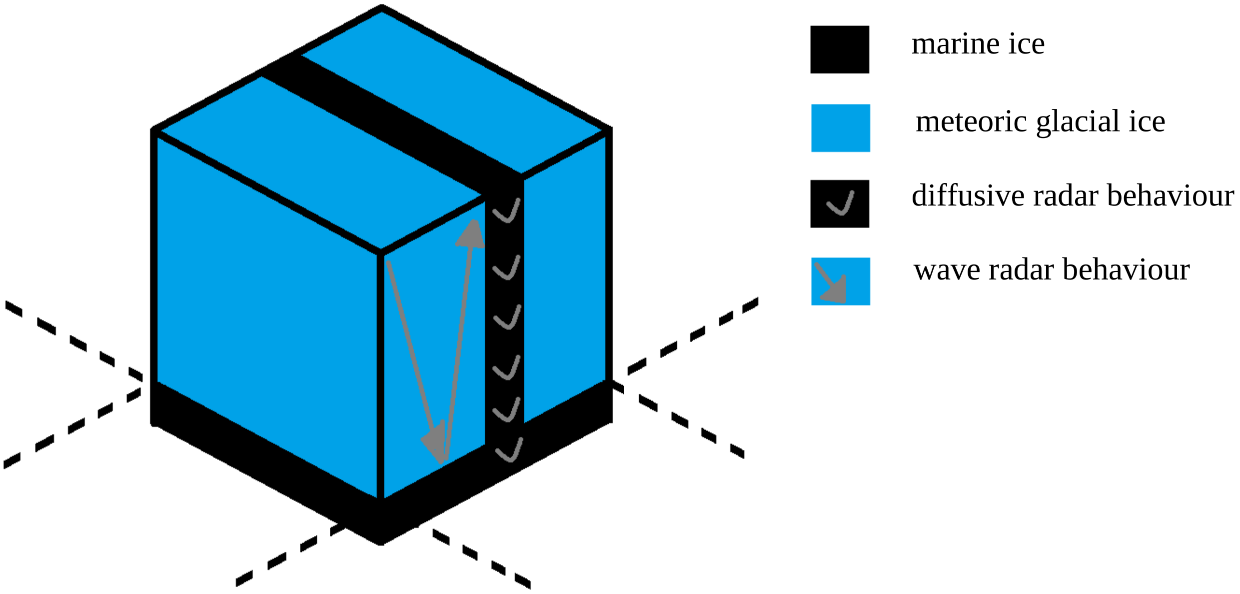

Figure 6.1: Block model showing the marine ice/ electromagnetic field behaviour scenario required to have the hydrostatic balance at the ice shelf edge be attributed to basal marine ice accumulation

Figure 5.11c shows that the heavily crevassed areas of the NIS close to the Reeves Glacier grounding line had positive hydrostatic imbalance, or surface elevations that were lower than they should have been considering the thickness of ice measured there. The full ice thickness rifts filling with marine-ice in these areas increases the bulk density of the ice, since marine-ice is denser with more impurities and no air bubbles (Dierckz and Tison 2013). Significant marine-ice inclusion may then have caused the areas to have an average bulk density significantly greater than 910 kg m^{-3}, which would reduce buoyancy as well as the surface elevations relative to the thickness of ice there. Reduced buoyancy would depress surface elevations relative to the thickness of ice, predicting smaller ice thicknesses than those measured generating a positive hydrostatic imbalance. The most central part of the ice shelf is in reasonable hydrostatic balance indicating that proximity to the grounding line and ice shelf edge may be factors affecting the hydrostatic imbalance observed on the NIS.

6.2 NIS basal channel

6.2.1 Basal channel morphology

The NIS basal channel, (Figure 5.3), is triangularly shaped with a slight curve in plan view. The channel expands by 5.5 km in width and 50 m in height along the suture zone over a length of 15 km and ends at the ice shelf edge. The growth in cross sectional area of the basal channel between two parallel cross sections located 1.2 km down-ice from each other, as re-illustrated in Figure 6.1, confirms that melt occurred in the basal channel portion of the NIS and reduced the number of sub-channels.

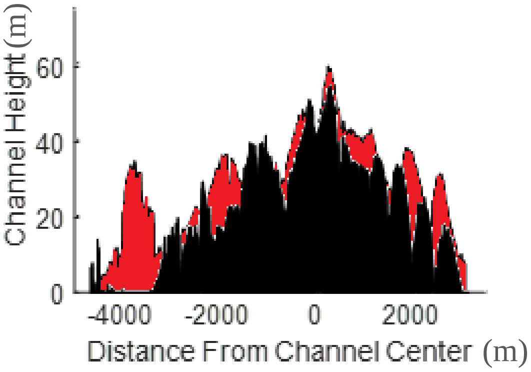

Figure 6.2: Down-ice change in channel cross sectional area between up-ice NCH2 survey line 10 (black) and down-ice NCH2 survey line 2 (red) displayed in Figure 5.10 over 1.2 km

The NIS is one of the smallest ice shelves observed to possess a basal channel in Antarctica (Alley et al., 2016); however, the coarse spatial resolution of satellites used to infer basal features

(Drews et al., 2015), may prevent small channels from being detected. In comparison to the average observed basal channels documented in the Antarctic that are typically 5 km wide and 200 m high (Alley et al., 2016) the NIS basal channel is a quarter the height for its width at 10 km wide and 90 m high. The NIS is also the widest basal channel reported, 3.5 km wider than the relatively well studied CDW driven basal channels of the Amundsen Sea (Alley et al., 2016, Dutrieux et al., 2014, Millgate et al., 2013, Vaughan et al., 2012), but appears much more narrow through hydrostatic equilibrium calculations. Basal channels have been modeled to form in areas of transverse differences in ice draft (Sergienko, 2013) and have been observed in suture zones between different branches of the Ronne-Filchner Ice Shelf (Fricker et al., 2012). The NIS basal channel is similar to other basal channels in this respect.

Vertical melt rates calculated across the channel were mostly within the uncertainty range of |6| m of ice thickness change over three years. Melt rates modeled in Antarctic ocean-sourced basal channels under the PIG Ice Shelf have yielded vertical melt rates of 30 m a^{-1} (Dutrieux et al., 2013). It is evident that the ocean forcing experienced by the NIS is different from other well studied ocean-sourced basal channels and that upwelling, intrusive, warm ocean water similar to the CDW was not the driving force behind the NIS basal channel formation.

6.2.2 Basal channel-ocean interaction

The NIS basal channel is an ocean-sourced area of enhanced melt, and therefore the ocean circulation of the ice shelf cavity is required to explain this enhancement. However, there are limited direct measurements of that environment available. Observations of the channel morphology, other studied basal channels and the surrounding ocean environment provide some insight into the controlling factors that may be driving this enhanced melt.

Many Antarctic basal channels are influenced by the Coriolis effect, which accelerates currents along their west channel flank thereby increasing energy transport (Alley et al., 2016; Dutrieux et al., 2013; Dutrieux et al., 2014; Gladish et al., 2012; Mankoff et al., 2012; Millgate et al, 2013; Seirgeinko, 2013). The NIS basal channel contains curved features longer than the local Rossby radius and had greater ice loss on its northern flank suggesting the Coriolis force may be influencing channel morphology here. Higher current velocities encourage more turbulent flow, which increases energy transport driving more efficient production and removal of super-cooled meltwater from the ice-ocean interface (Holland and Jenkins, 1999). The complex morphology of the NIS basal channel suggests that channel currents would likely be turbulent along this complex ice-ocean interface.

Ocean temperature, salinity and velocity in Terra Nova Bay can be used as a first-order approximation of the water properties in the NIS cavity near the ice shelf edge. The Terra Nova Bay polynya has temporally stable north-east currents of 7.4 cm s^{-1} located at depths of 144 m (Manzella et al., 1999), which is similar to the ice draft of the basal channel there. The north-east currents are in the same approximate orientation and depth as the oblique northern flank sub-channels labelled in Figure 5.4. The north-east current may be present in the basal channel as well and could be influencing the sub-channel morphology at that location. Using typical Terra Nova Bay salinities of 34.54 to 34.78 psu (practical salinity units), and a temperature of -1.86 ºC (Manzella et al., 1999), a pressure freezing temperature of -2.00 ºC can be estimated at 140 m depth (as calculated using TEOS-10). Assuming this water is representative to the basal channel ice-ocean interface, there would be a driving temperature of ~0.14 ºC to melt ice in the channel at that depth. This relatively low driving temperature agrees with the relatively low vertical melt rates calculated.

A CTD cast in 2017 through the Priestley Glacier branch of the NIS, ~15 km up-ice of the suture zone revealed isothermal super-cooled water at -2.3 ºC around ~400 m depth, indicating a quiet ocean environment in the sheltered part of the NIS cavity that should promote marine-ice accumulation as observed on the Hell’s Gate Ice Shelf (T Scambos, personal communication). The contrast in the measured ocean properties under the Priestley Glacier branch and those assumed to be at the ice shelf edge near the basal channel, suggests that there are major gradients within the NIS cavity between these two locations. The convergence and formation of the suture zone with differing ice drafts under the central area of the ice shelf may increase current velocity and turbulence. Without any evidence of water warmer than -1.86 ºC the most simplistic assumption is that melting is enhanced in the channel because of increased velocities generating turbulent currents in the suture zone. One particular basal channel formation model explains that the upwelling of warm water under an ice shelf can be supplemented by high velocity horizontal currents where there are substantial transverse differences in ice draft (Sergienko 2013). These processes may be influencing the basal channel formation in the NIS. Obtaining cavity and basal channel oceanographic data, should be a major focus of future research on the NIS.

6.2.3 Hydrostatic balance of the NIS basal channel

The hydrostatic balance DITMs (Figure 5.12) and hydrostatic ice thickness cross sections (Figure 5.13) show that the basal channel and the areas of the ice shelf on either side of it experienced a negative hydrostatic imbalance, which indicates that surface elevations were higher than they should have been in comparison to the measured ice thickness. The basal channel extent area was on average -0.12 m m^{-2} out of balance, suggesting that the ice surface across the eastern edge of the ice shelf was being ‘held up’ higher than it would have been if it were floating in hydrostatic equilibrium.

Potential causes of hydrostatic imbalance might be: Inexpressible Island as a pinning point at the ice shelf edge, uplift following the large calving event of 2016, reduction of surface elevations along discrete paths due to erosion from the surface meltwater river, the complex morphology of the NIS basal channel (discussed in Section 6.3.3), or basal marine-ice accumulation as discussed above in Section 6.1. Figures 5.11c and 5.12c show that at the ice shelf edge the area most out of balance was adjacent to Inexpressible Island with a large scale trend towards, without reaching, hydrostatic balance at the southern ice shelf edge of the NIS. The presence of Inexpressible Island at the ice shelf edge may have played a significant role in ‘holding up’ adjacent portions of the NIS similar to the observed doming of ice around pinning points by up to 5-15 m over an area of ~200 km^2 (Furst et al., 2015).

The calving event that occurred in 2016 represented a ~ 12 % loss of the ice shelf surface area and might also have significantly altered the hydrostatic balance of the ice shelf. However, to date there has been no work examining the effect of large calving events on ice shelf hydrostatic balance. Future radar surveys across the ice shelf edge could re-measure hydrostatic balance to examine if has moved closer to zero since the 2016/17 surveys.

Ice removal from the surface melt water system would have acted against the large scale negative hydrostatic imbalance seen in Figure 5.12c. Discrete removal of ice along the channel center created a non-uniform hydrostatic imbalance observed as alternating positive and negative signatures down the channel center. Furthermore, the semi-circular sub-channels on the north side of the channel curved away from the channel center in the measured ice thicknesses of Figure 5.12a but appeared to run close to 90 ° to the channel center in the hydrostatic equilibrium ice thicknesses of Figure 5.12b. The semi-circular meltwater ponds likely filled and drained into the main surface river, driven by the surface topography gradient, which would have cut into and removed part of the circular shape of these features on the surface that was originally expressed through hydrostatic equilibrium.

6.3 NIS sub-channel features

The density of radar lines over the NIS basal channel offers high resolution images of the complex morphology that has been mentioned, but not described in other basal channel work (Drews et al. 2015; Dutrieux et al., 2013; Gladish et al., 2012; Mankoff et al., 2012; Vaughan et al., 2012;). Figure 5.4 reveals semi-continuous sub-channels that comprise most of the complex channel morphology.

6.3.1 Sub-channel melt rates

Significant melt rates in the channel, within 2 km of the ice shelf edge, were concentrated far from the centre, at sub-channel apexes, on the northern flank. The northern flank was also 2 km wider at the ice shelf edge than the southern flank, suggesting that melt in the channel may have been focused in the oblique to channel center sub-channels on the northern flank. Areas with significant ice accretion values were evenly distributed across sub-channel apexes and keels, located near the channel center on the southern flank. If melt was focused away from the channel center in the long oblique northern flank sub-channels, then they may have pirated some of the current and focused heat away from the channel center at the ice shelf edge, similar to the larger-scale effect that basal channels have on mitigating net melt across an ice shelf (Mankoff, 2012; Millgate et al., 2013).

The observed reduction in the number of sub-channels on the northern flank in Figure 5.10 from 4 to 2 between two cross sections 1.2 km apart suggests that significant melt must have been occurring to account for this reduction. Three scenarios may exist to explain this discrepancy: all the points of the ice-ocean interface where significant melt occurred were not captured by the apex and keel analysis method; vertical melt that occurred at sub-channel apexes and keels between cross sections 200 m apart were below the detection limit for this method, or a large portion of the enhanced melt was focused in the northern flank's oblique semi-circular sub-channels, which were poorly represented in transverse cross sections. A combination of the scenarios is likely where melt occurred across the entire ice-ocean interface in the channel, the calculations of changes in ice thickness were below the greatest possible error limit hiding many small melt rates over short distances that accumulated to significant mass loss at a larger scale, and that the long oblique sub-channels of the northern flank may have driven melt away from the channel center.

6.3.2 Sub-channel hydrostatic balance

In the absence of radar surveys, remotely sensed surface elevations from satellite observations are used to detect basal channel shape. While sub-channels are likely to be partly detected by undulating surface depressions, channel morphology will be largely misrepresented in size by surface elevations according to Figure 5.13. Features under ~350 m wide were less likely to be represented if they were situated between features of contrasting ice draft and sometime even features even wider than 350 m were undetected if this contrast was great enough. Monitoring and modelling small scale morphology in more deeply incised basal channels is then subject to error if satellite altimetry alone is used to make interpretations of features less then ~350 m wide.

Error associated with small scale interpretations of complex basal channel morphology from surface elevation is in agreement with many other investigations of basal channels that have measured ice thickness (Drews et al. 2015; Gladish et al., 2012; Mankoff et al., 2012; Vaughan et al., 2012). Ice bridging has been determined to be responsible for the small scale hydrostatic imbalance of discrete features, which prevents the surface from depressing (Drews et al., 2015). Gladish et al. (2012) hypothesized that adjustment to hydrostatic equilibrium from locally varying melt rates is slower than the residence time of ice on an ice shelf, leading to permanent hydrostatic imbalance of rapidly melting features. However, the work presented here shows that even a slowly melting basal channel can be subject to these small scale hydrostatic imbalances.

Significant widespread marine-ice accumulation at the ice shelf edge is unlikely as discussed in Section 6.1.2; however, smaller scale marine-ice accumulation near the ice shelf edge is possible and suggested by significant ice accretion under sub-channel keels (Figure 5.9) along with relatively larger hydrostatic imbalances at the same locations. Figure 5.13 indicates that ice thickness minimums (sub-channel apexes) were more often closer to hydrostatic equilibrium while local ice thickness maximums (sub-channel keels) were more often further from hydrostatic equilibrium, suggesting that some sub-channel keels may have had significant marine-ice accumulation that was not detected by the radar system. The sub-channel apexes either did not have this marine-ice accumulation or the radar system was systematically able to resolve the ice-ocean interface at sub-channel apexes but not at sub-channel keels, perhaps due to sub-channel flanks interfering with the radar reflections. Other studies examining basal channel hydrostatic balance have discussed the possibility of marine-ice accumulation in basal channels (Drews et al., 2015). However, the bridging of narrow features is often considered the driving cause of local hydrostatic imbalances (Drews et al., 2015), which seems more probable than wide-spread marine ice accumulation along an ice-ocean interface in a zone of enhanced melt.

6.3.3 Sub-channel strain rates and morphology

There is a clear relationship between the northern flank sub-channels seen in Figure 5.4 and the strain rates observed in Figure 5.5. The Priestley Glacier branch of the NIS experiences a predominantly compressive strain regime as it is squeezed between the Reeves Glacier and Inexpressible Island at the ice shelf edge. The confined boundary conditions of the Priestly Glacier branch at the ice shelf edge and the enhanced melt experienced on this flank of the basal channel likely affects its strain regime and ice draft morphology, respectively, which appear to relate with each other spatially. The semi-circular bands of alternating compressional and extensional strain rates are observed on the northern flank of the channel, at ~ 40º to ice flow. These semi-circular strain rate bands align with the semi-circular, oblique to channel center, sub-channels in the DEMs and DITMs. Sub-channels themselves are not features previously defined and the semi-circular oblique sub-channels have not yet been described in the other basal channel studies discussed here, and should therefore be further investigated in the future.

There are two likely processes that may explain the formation of the curved nature of these features: 1) the Coriolis effect exerting a control on sub-channel shape, or 2) the alternating strain rate bands driving curved ice draft minimums in the topography for buoyant, high velocity plumes to flow along. The Coriolis effect could have deflected water movement in the ice shelf cavity to the north creating counter clockwise tracks over time as melting caused erosion of this part of the ice shelf. The radius of the largest semi-circular sub-channel was ~1.5 km, in comparison to the Rossby radius in Terra Nova Bay of 650 m (C Zappa, personal communication) indicating that the control of the Coriolis effect on deflection of water in this region could be significant enough to contribute to the observed sub-channel curving. The melting of these features may have then influenced the strain regime producing the alternating strain bands. Conversely, the location of the semi-circular sub-channels may have been determined by the strain regime, whereby the boundary conditions of the Reeves and Priestley Glacier branches initially produced the transverse alternating bands of compressional and extensional strain along the suture zone, which manifested itself in the ice draft topography, and provided pathways for buoyant water plumes to melt the sub-channel features. Drews et al. (2015) also concluded that channel morphology is related to the surface ice velocities of the Roi Baudouin Ice Shelf**,** and even suggested that surface velocities and related strain rates from satellite observation may be sufficient to characterize basal channel morphology.

Two continuous bands of strain occurred on either side of the channel center (Figure 5.5); a compressional ridge to the slower-flowing northern flank and an extensional ridge to the faster flowing southern flank. The two consistent bands of strain were parallel to the channel apex within 20 km of the ice shelf edge. The presence of marine-ice filled rifts may have played a role in concentrating the shear strain created by the contrasting branch velocities in these marine-ice stripes near the main channel apex allowing for the two continuous bands of contrasting strain to persist (Jansen et al., 2013). The continuous band of extensional strain on the southern side of the basal channel center may have allowed the basal channel features of the southern flank to extend more than those on the northern flank. Beyond this, the strain regime at the southern flank of the basal channel, south of the extensional strain band, did not have an observable pattern like the northern flank did. The movement of the sub-channels away from the channel center on the southern flank, was likely related to the extensional strain regime there, as can be seen by the migration of the southern flank sub-channels to the left in Figure 6.1.

Surface elevations are known to produce significant errors when predicting small scale channel morphology (Drews et al. 2015; Gladish et al., 2012; Mankoff et al., 2012; Vaughan et al., 2012) where ice bridging causes hydrostatic imbalances. Horizontal strain rates derived from surface ice velocities in addition to surface elevations may be better indicators of small and large scale channel morphology than using surface elevations alone. Identifying a relationship between surface ice velocity and complex channel morphology is in agreement with Drews et al. (2015) who observed enhanced horizontal shear corresponding to small features of a basal channel under the Roi Baudouin Ice Shelf that were not represented through hydrostatic equilibrium. More work is needed to quantify the relationship between the size of strain rate vectors and the size of sub-channel features.

6.4 Nansen ice shelf stability

Models and laboratory experiments examining the rheology of marine-ice and the effect that significant bottom accretion or marine ice filled crevasses have on the stability of ice shelves have determined that the lower viscosity of marine-ice enhances stability (Dierckx and Tison, 2013; Jansen et al., 2013; Khazendar et al., 2009). The results of laboratory work on ice cores taken from the NIS determined that the reduced viscosity of marine-ice is not an intrinsic property but rather is related to the warmer temperature profiles associated with this type of ice (Dierckx and Tison, 2013). The presence of large quantities of marine-ice likely increases the NIS's stability by facilitating the shear strain along the suture zone, reducing the risk of brittle failure (Jansen et al., 2013).

The NIS basal channel does not appear to be growing rapidly based on calculated vertical melt rates. Concentrated surface drainage over the NIS basal channel was first detected in satellite imagery and airborne photos in 1975 (Belle et al., 2017), indicating that the basal channel may be at least 44 years old. A large, 170 km^2 calving event, 53 – 43 years previous to the April 2016 event, was documented on the NIS from a difference in ice shelf extent between two aerial photos, but was not directly observed (Frezzotti, 2000). Historic evidence for the presence of the

NIS basal channel and documented calving events of similar size to the April 2016 calving event may indicate that feedbacks between surface melt water and basal channel induced rifts have occurred for many years at this location. Calving similar to the April 2016 event could be occurring with some consistent frequency every several decades and as such the basal channel may not pose an immediate risk to the NIS's stability. However, a warming atmosphere around the Antarctic (Trusel et al., 2013) will increase the volume of melt water present on the NIS surface and generate progressively larger surface river systems over time that will more readily be able to interact with any transverse crevasses or rifts that might appear. Through this mechanism, the stability of the NIS may be at risk if large calving events begin to occur with greater frequency.

If large calving events became more frequent, the size of the NIS will reduce and the grounded glacier velocity will likely increase. A retreat of the Priestley and Reeves grounding lines may also occur and a drawdown of their grounded ice thickness would then be expected (e.g. Scambos et al., 2004). If increased mass loss driven by more frequent calving events causes the NIS to retreat and lose contact with the Inexpressible Island pinning point (Favier et al., 2012), the buttressing force the NIS applies to the Eastern Antarctic's Taylor domes could reduce significantly (Favier et al., 2012; Frezzotti et al., 2000). Over the last 30 years, reductions in ice shelf extent of the NIS and Hells Gate Ice Shelf have already exposed the entire, previously ice covered, eastern coastline of Inexpressible Island to the ocean (Baroni et al., 1992), suggesting that this process may already be occurring.

If the NIS basal channel has existed for over 45 years then it is likely that it was maintained by a consistent sub-ice shelf environment. As atmospheric temperatures continue to increase, altering the climate, wind patterns and ocean circulation (Pritchard et al., 2012), the cold and turbulent conditions of Terra Nova Bay may also change. A warming VLCC, reductions in sea ice, mass loss from DIT, or the introduction of infiltrating ocean currents could all introduce more heat underneath the NIS. Increased basal melt rates similar to those observed in other channels could possibly lead to rapid channel growth, changing the morphology of the basal channel, potentially growing and merging sub-channels, and further incising the feature. However, by the time the climate changes enough to cause these effects, it may be that increased calving rates have already destabilized a portion of the NIS.

Chapter 7

Conclusion

Ice shelves surrounding Antarctica act as retaining walls holding much of the Antarctic Ice Sheet's mass on land, preventing it from displacing ocean water and increasing global sea level. Many ice shelves are actively thinning and experiencing dynamic change as the atmosphere warms, wind patterns shift, and ocean currents deliver warm water to Antarctica's continental shelf (Pritchard et al., 2012). This thesis examines the morphology of the NIS and its basal channel, which is a region of widening and enhanced melt at the suture zone of the Priestley and Reeves glaciers. Approximately 1000 km of spatially dense grids of IPR were collected over the Nansen Ice Sheet in East Antarctica and these data have begun to elucidate relationships between processes at the ice-ocean interface and those at the surface of the ice shelf. The data presented here, in the form of DEMs and DITMs can be used as context for researchers planning future studies on the NIS, and also provides data that will be directly comparable to future measurements.

7.1 The main NIS area

The NIS is a small and complex ice shelf as revealed by radar surveys and surface ice velocities. From the research presented in this thesis, the following has been determined about the NIS:

1. There are two areas of poor ice supply near the grounding line that generate marine ice filled rifts which advect to ice shelf edge as observable stripes parallel to mean surface ice flow.
2. The NIS is largely out of hydrostatic balance, with depressed surface elevations down-ice of the Reeves Glacier grounding line and elevated surface elevations across the ice shelf edge, especially near Inexpressible Island. With little geophysical evidence of wide spread marine ice accumulation at the ice shelf edge, the hydrostatic imbalance at the ice shelf edge is likely a combined effect from the Inexpressible Island pinning point, the

large calving event in April 2016 that preceded the surveys, and enhanced melting of the basal channel.

3. The NIS has a 15 km long, 60 - 90 m high and ~10 km wide ocean-sourced basal channel that grows as a result of enhanced melt in the suture zone between the Reeves and Priestley glaciers. Based on an approximated driving temperature of 0.14 ºC in the basal channel near the ice shelf edge, and the difference in morphology between this channel and others in the Antarctic, basal channel formation is hypothesized to be driven by increased current velocities within the suture zone.

7.2 The NIS basal channel

Grids of airborne radar surveys have been used successfully over basal channels by others to: confirm channel presence (Alley et al., 2016; Le Brocq et al., 2013), calculate mass balance to determine basal melt rates (Rignot and Steffen, 2008), provide ice thickness constraints for models validating channel formation processes (Drews et al., 2015, Le Brocq et al., 2013), and generate ice draft DEMs to describe hydrostatic imbalance and observe/model the formation of basal and surface crevasses (Vaughan et al., 2012). The investigation of the NIS basal channel using a dense grid of radar surveys determined:

1. The NIS basal channel’s complex morphology consists mostly of semi-continuous sub-channels where melt appears to be focused in local apexes. The distribution and continuity of these sub-channels changes on the km-scale indicating that melt and ice strain history are markedly variable between neighbouring up-ice and down-ice parcels of ice.
2. The NIS basal channel is largely out of equilibrium. Using surface elevations and hydrostatic calculations is sufficient to identify that a basal channel with some discrete sub-channel features exists but the width and ice draft of the channel is inaccurate and many of the narrower sub-channel features are not represented. This result is not unique to the NIS basal channel and has been mentioned in other work (Drews et al. 2015; Gladish et al., 2012; Mankoff et al., 2012; Vaughan et al., 2012), though no other method currently exists to remotely sense basal channels accurately without radar surveys. The use of satellite based remote sensing to detect, measure, and monitor basal

channels should incorporate more than just hydrostatic balance to determine the ice shelf draft.

3. There is a spatial relationship between surface strain rates and sub-channel features. While the cause of this relationship is currently unknown, if further investigated, it might allow for a method of satellite based remote sensing not limited by the errors of the hydrostatic equilibrium assumption at smaller scales.
4. Ocean currents in the NIS basal channel near the ice shelf edge, may have a significant component of velocity consistently oriented north-east, at ~40 º from the channel center. Vertical melt in the basal channel near the ice shelf edge was focussed in the oblique sub-channel apexes, on the northern flank. One of these sub-channels extends 3 km from the channel center line to the ice shelf edge where ocean currents at the same depth and orientation have been measured in Terra Nova Bay with a temperature of -1.86 ºC.

Based on the data examined in this thesis, the NIS is relatively stable and likely not at risk of substantial retreat in the near future. The ice shelf is stabilized by the presence of pinning points at the grounding line and ice shelf edge, the inclusion of longitudinal stripes of full thickness marine ice, and the reasonably low melt rates. One potential risk to the stability of the NIS is that atmospheric warming will continue to drive surface river formation, which will be more readily available to interact with transverse crevasses across the basal channel and then may increase the rate of large calving events, and reduce contact of the ice shelf with Inexpressible Island.

7.3 Recommended future work

With accurate DEMs and DITMs of the NIS constructed, the greatest remaining knowledge gap is the size of NIS cavity and the nature of the ocean circulation within it. Drilling into the NIS basal channel in the main channel apex and one of the larger oblique to channel center sub-channels could potentially confirm the hypothesis of enhanced melt in the suture zone due to greater current velocities. Furthermore, phase sensitive radar surveys near the ice shelf edge (capable of measuring and detecting marine ice) could confirm the argument made in this thesis that the hydrostatic imbalance at the ice shelf edge is not caused by wide spread marine ice accumulation.

In the future, full or partial repeat radar surveys over the NIS basal channel could examine the change between two spatially identical DITMs over time, producing a point to point change in ice thickness over the basal channel, providing a more complete analysis of the distribution of melt and accretion throughout the channel. In addition, comparing the elucidated melt/accretion distribution to changes in the strain regime from Go-LIVE data could present an opportunity to quantify the relationship between strain rates change and sub-channel morphology change, hopefully creating a methodology that could be tested on other Antarctic ice shelves with basal channels. Significant modelling efforts would be needed to accomplish this goal, which were beyond the scope of this thesis.

If the relationship between surface strain, surface elevations and basal channel morphology can be better quantified, an approximation of basal channel morphology could be calculated from Landsat imagery and surface elevation data, remotely generating a database of basal channel change through time.

7.4 Overview

The NIS basal channel morphology is unique in width and height possibly due to the relatively smaller amount of residual heat energy available for melting (~0.14 ºC) and the development of large oblique sub-channels. The ocean conditions that encourage enhanced melt and the ice draft topographies in which that melting occurs is variable around Antarctic creating different types of basal channels, ranging from the networks of channels in the Amundsen Sea driven by CDW to the subglacially fed basal channels at the grounding line of most major ice streams (Alley et al., 2016; Le Brocq et al., 2013). In order to make progress on accurately predicting channel growth and ice shelf response to that growth, a large database of accurate channel morphology observations is required. The hydrostatic imbalance common over basal channels is a large obstacle in being able to generate this database, requiring gridded radar surveys over many difficult to access Antarctic ice shelves. Analyzing the relationship between cross sectional channel morphology and strain rates may be a crucial first step in generating an accurate database that can be used to numerically predict channel growth.

It has been demonstrated that ice shelf basal channels are growing in the presence of warming ocean water and that their growth locally reduces ice volume, which not only reduces buttressing force from basal mass loss, but can contribute to large calving events through enhanced strain and rifting (Dow et al., 2018). The effect of basal channel growth around the Antarctic has not been sufficiently quantified and is therefore not currently represented in global models that predict ice shelf collapse and global sea level rise. This thesis infers many possible relationships between ice-ocean interaction and surface processes that should be priorities of future basal channel research, which will assist in the modeling the impacts of channel growth on Antarctic ice shelves.

References

Alley, R. B., Horgan, H. J., Joughin, I., Cuffey, K. M., Dupont, T. K., Parizek, B. R., Anandakrishnan, S. & Bassis, J. (2008). A simple law for ice-shelf calving. *Science*, 322(5906), 1344-1344.

Alley, K. E., Scambos, T. A., Siegfried, M. R., & Fricker, H. A. (2016). Impacts of warm water on Antarctic ice shelf stability through basal channel formation. *Nature Geoscience*, 9(4), 290-293.

Arcone, S. A. (2009). Glaciers and ice sheets. In *Ground penetrating radar theory and applications*, (Vol 1, pp. 361-392). Kidlington, Oxford: Elsevier Science.

Annan, A. P. (2009). Electromagnetic principles of ground penetrating radar. In *Ground penetrating radar theory and applications* (Vol. 1, pp. 1-37). Kidlington, Oxford: Elsevier Science.

Baroni, C., Frezzotti, M., Giraudi, C., & Orombelli, G. (1991). Ice flow and surficial velocity inferred from satellite image and air photo analysis of Larsen Ice tongue, Hells Gate and Nansen ice shelves (Northern Victoria Land, Antarctica). *Memorie Della Societa'Geologica Italiana, 46*, 69-80.

Bassis, J. N. (2011). The statistical physics of iceberg calving and the emergence of universal calving laws. *Journal of Glaciology,* 57(201), 3-16.

Bassis, J. N., & Ma, Y. (2015). Evolution of basal crevasses links ice shelf stability to ocean forcing. *Earth and Planetary Science Letters*, 409, 203-211.

Benn, D. I., & Evans, D. J. (2014). *Glaciers & Glaciation* (Second ed.). London: Routledge.

Benn, D. I., Warren, C. R., & Mottram, R. H. (2007). Calving processes and the dynamics of calving glaciers. *Earth-Science Reviews*, 82(3), 143-179.

Bell, R. E., Chu, W., Kingslake, J., Das, I., Tedesco, M., Tinto, K. J., Zappa C. J., Frezzotti, M., Boghosia, A., & Lee, W. S. (2017). Antarctic ice shelf potentially stabilized by export of meltwater in surface river. *Nature*, 544(7650), 344-348.

Bindschadler, R., Choi, H., Wichlacz, A., Bingham, R., Bohlander, J., Brunt, K., Corr, H., Drews., R., Fricker, H., Hall, M., Hindmarsh, R., Kohler, J., Padman, L., Rack, W., Rotchky, G., Urbini, S., Vornberger, P.,Young, N. (2011). Getting around Antarctica: New high-resolution mappings of the grounded and freely-floating boundaries of the Antarctic ice sheet created for the International Polar Year. *The Cryosphere*, 5(3), 569-588. doi:10.5194/tc-5-569-2011

Blewitt, G., Hammond, W. C., & Kreemer, C. (2018). Harnessing the GPS data explosion for interdisciplinary science, *Eos, 99,* Doi:10.1029/2018EO104623.

Blindow, N. (1994). The central part of the Filchner-Ronne Ice Shelf, Antarctica: internal structures revealed by 40MHz monopulse RES. *Annals of Glaciology,* 20, 365-371.

Budillon, G., & Spezie, G. (2000). Thermohaline structure and variability in the Terra Nova Bay polynya, Ross Sea. *Antarctic Science*, 12(4), 493-508.

Cappelletti, A., Picco, P., & Peluso, T. (2010). Upper ocean layer dynamics and response to atmospheric forcing in the Terra Nova Bay polynya, Antarctica. *Antarctic Science*, 22(3), 319-329.

Carter, S. P., D. D. Blankenship, M. E. Peters, D. A. Young, J. W. Holt, and D. L. Morse (2007), Radar-based subglacial lake classification in Antarctica, *Geochemistry. Geophysics. Geosystems.,* 8, Q03016, doi:10.1029/2006GC001408.

Cuffey, K. M., & Paterson, W. S. B. (2010). *The Physics of Glaciers*. Kidlington, Oxford: Academic Press.

DeConto, R. M., & Pollard, D. (2016). Contribution of Antarctica to past and future sea-level rise. *Nature*, 531(7596), 591-597.

Dierckx, M., & Tison, J. L. (2013). Marine-ice deformation experiments: an empirical validation of creep parametres. *Geophysical Research Letters*, 40(1), 134-138.

Dow, C. F., Lee, W. S., Greenbaum, J. S., Greene, C. A., Blankenship, D. D., Poinar, K., Forest, A., Young, D., & Zappa, C. J. (2018). Basal channels drive active surface hydrology and transverse ice shelf fracture. *Science Advances*, 4(6), eaao7212.

Dowdeswell, J. A., & Jeffries, M. O. (2017). Arctic ice shelves: An introduction. In Arctic ice shelves and ice islands (pp. 3-21). *Springer*, Dordrecht.

Drews, R. (2015). Evolution of ice shelf channels in Antarctic ice shelves. *The Cryosphere*, 9(3), 1169-1181.

Dupont, T. K., & Alley, R. B. (2005). Assessment of the importance of ice-shelf buttressing to ice-sheet flow. *Geophysical Research Letters*, 32(4).

Dutrieux, P., Stewart, C., Jenkins, A., Nicholls, K. W., Corr, H. F., Rignot, E., & Steffen, K. (2014). Basal terraces on melting ice shelves. *Geophysical Research Letters*, 41(15), 5506-5513.

Dutrieux, P., Vaughan, D. G., Corr, H. F., Jenkins, A., Holland, P. R., Joughin, I., & Fleming, A. H. (2013). Pine Island glacier ice shelf melt distributed at kilometre scales. *The Cryosphere*, 7(5), 1543.

Dutrieux, P., De Rydt, J., Jenkins, A., Holland, P. R., Ha, H. K., Lee, S. H., ... & Schröder, M. (2014). Strong sensitivity of Pine Island ice shelf melting to climatic variability. *Science*, 343(6167), 174-178.

Fahnestock, M., T. Scambos, T. Moon, A. Gardner, T. Haran, and M. Klinger. (2015). Rapid large-area mapping of ice flow using Landsat 8, *Remote Sensing of Environment*. 185. 84-94. DOI: 10.1016/j.rse.2015.11.023

Favier, L., Gagliardini, O., Durand, G., & Zwinger, T. (2012). A three-dimensional full Stokes model of the grounding line dynamics: effect of a pinning point beneath the ice shelf. *The Cryosphere*, 6, 101-112.

Förste, C., Schmidt, R., Stubenvoll, R., Flechtner, F., Meyer, U., König, R., ... & Loyer, S. (2008). The GeoForschungsZentrum Potsdam/Groupe de Recherche de Geodesie Spatiale satellite-only and combined gravity field models: EIGEN-GL04S1 and EIGEN-GL04C. *Journal of Geodesy*, 82(6), 331-346.

Frezzotti, M. (1997). Ice front fluctuation, iceberg calving flux and mass balance of Victoria Land glaciers. *Antarctic Science*, 9(1), 61-73.

Frezzotti, M., Tabacco, I. E., & Zirizzotti, A. (2000). Ice discharge of eastern Dome C drainage area, Antarctica, determined from airborne radar survey and satellite image analysis. *Journal of Glaciology*, 46(153), 253-264.

Fricker, H. A., Coleman, R., Padman, L., Scambos, T. A., Bohlander, J., & Brunt, K. M. (2009). Mapping the grounding zone of the Amery Ice Shelf, East Antarctica using InSAR, MODIS and ICESat. *Antarctic Science*, 21(05), 515-532.

Fujita, S., Matsuoka, T., Ishida, T., Matsuoka, K., & Mae, S. (2000). A summary of the complex dielectric permittivity of ice in the megahertz range and its applications for radar sounding of polar ice sheets. *In Physics of Ice Core Records* (p. 185-212). Hokkaido University Press.

Fürst, J., Durand, G., Gillet-Chaulet, F., Merino, N., Tavard, L., Mouginot, J., ... & Gagliardini, O. (2015). Assimilation of Antarctic velocity observations provides evidence for uncharted pinning points. *The Cryosphere*, 9(4), 1427-1443.

Fürst, J. J., Durand, G., Gillet-Chaulet, F., Tavard, L., Rankl, M., Braun, M., & Gagliardini, O. (2016). The safety band of Antarctic ice shelves. *Nature Climate Change*, 6(5), 479-482.

Gladish, C. V., Holland, D. M., Holland, P. R., & Price, S. F. (2012). Ice shelf basal channels in a coupled ice/ocean model. *Journal of Glaciology*, 58(212), 1227-1244.

Greenbaum, J. S., Blankenship, D. D., Young, D. A., Richter, T. G., Roberts, J. L., Aitken, A. R. A., Legresy, B., Schroeder, D.M.., Warner, R.C.., Van Ommen, T.D., & Siegert, M. J. (2015). Ocean access to a cavity beneath Totten Glacier in East Antarctica. *Nature Geoscience*, 8(4), 294-298.

Greene, C. A., Gwyther, D. E., & Blankenship, D. D. (2017) Antarctic mapping tools form. *Computers & Geosciences*. 104 pp.151-157. DOI:10.1016/j.cageo.2016.08.003

Griggs, J. A., & Bamber, J. L. (2011). Antarctic ice shelf thickness from satellite radar altimetry. *Journal of Glaciology*, 57(203), 485-498.

Hellmer, H., & Beckmann, A. (1998). The influence of ice shelves on the Weddell Sea. *Forum for Research into Ice Shelf Processes Report*, 12, 40-44.

Holland, D. M. (2002). Computing marine-ice thickness at an ice shelf base. *Journal of Glaciology*, 48(160), 9-19.

Holland, D. M., & Jenkins, A. (1999). Modeling thermodynamic ice–ocean interactions at the base of an ice shelf. *Journal of Physical Oceanography*, 29(8), 1787-1800.

Holland, P. R., Jenkins, A., & Holland, D. M. (2008). The response of ice shelf basal melting to variations in ocean temperature. *Journal of Climate*, 21(11), 2558-2572.

Holland, P. R., Corr, H. F., Vaughan, D. G., Jenkins, A., & Skvarca, P. (2009). Marine ice in Larsen ice shelf. *Geophysical Research Letters*, 36(11).

Holt, J., Hyder, P., Ashworth, M., Harle, J., Hewitt, H. T., Liu, H., New, A.L., Pickles, S., Porter, A., Popova, E., Allen, J,I., Siddorn, J., & Wood, Richard. (2017). Prospects for improving the representation of coastal and shelf seas in global ocean models. *Geoscientific Model Development*, 10, 499-523.

Hogg, A. E., & Gudmundsson, G. H. (2017). Impacts of the Larsen-C Ice Shelf calving event. *Nature Climate Change*, 7(8), 540.

Jansen, D., Luckman, A., Kulessa, B., Holland, P. R., & King, E. C. (2013). Marine-ice formation in a suture zone on the Larsen C Ice Shelf and its influence on ice shelf dynamics. *Journal of Geophysical Research: Earth Surface*, 118(3), 1628-1640.

Jenkins, A. (1991). A one-dimensional model of ice shelf-ocean interaction. *Journal of Geophysical Research*: *Oceans*, 96(C11), 20671-20677.

Jenkins, A. (2011). Convection-driven melting near the grounding lines of ice shelves and tidewater glaciers. *Journal of Physical Oceanography*, 41(12), 2279-2294.

Joughin, I., Smith, B. E., & Medley, B. (2014). Marine-ice sheet collapse potentially under way for the Thwaites Glacier Basin, West Antarctica. *Science*, 344(6185), 735-738.

Khazendar, A., Rignot, E., & Larour, E. (2009). Roles of marine-ice, rheology, and fracture in the flow and stability of the Brunt/Stancomb-Wills Ice Shelf. *Journal of Geophysical Research: Earth Surface*, 114(F4).

Khazendar, A., Tison, J. L., Stenni, B., Dini, M., & Bondesan, A. (2001). Significant marine-ice accumulation in the ablation zone beneath an Antarctic ice shelf. *Journal of Glaciology*, 47(158), 359-368.

Kouba, J., & Héroux, P. (2001). Precise point positioning using IGS orbit and clock products. *GPS Solutions*, 5(2), 12-28.

Kulessa, B., Jansen, D., Luckman, A. J., King, E. C., & Sammonds, P. R. (2014). Marine-ice regulates the future stability of a large Antarctic ice shelf. *Nature Communications*, 5, 3707.

Kurtz, D. D., & Bromwich, D. H. (1983). Satellite observed behavior of the Terra Nova Bay polynya. *Journal of Geophysical Research: Oceans*, 88(C14), 9717-9722.

Le Brocq, A. M., Ross, N., Griggs, J. A., Bingham, R. G., Corr, H. F., Ferraccioli, F., Jenkins, A., Jordam, T.A., Payne, A.J., Rippin, D.M., & Siegert, M. J. (2013). Evidence from ice shelves for channelized meltwater flow beneath the Antarctic Ice Sheet. *Nature Geoscience*, 6(11), 945-948.

Lewis, E. L., & Perkin, R. G. (1986). Ice pumps and their rates. *Journal of Geophysical Research Letters: Oceans*, 91(C10), 11756-11762.

Lindzey, L., Quartini, E., Buhl, D., Blankenship, D., Richter, T., Greenbaum, J., & Young, D. (2017). KRT1/LGV1 Season Field Report. Austin, Texas. University of Texas Institute for Geophysics.

Luckman, A., Jansen, D., Kulessa, B., King, E., Sammonds, P., & Benn, D. I. (2012). Basal crevasses in Larsen C Ice Shelf and implications for their global abundance. *The Cryosphere*, 6(1), 113-123.

Mankoff, K. D., Jacobs, S. S., Tulaczyk, S. M., & Stammerjohn, S. E. (2012). The role of Pine Island Glacier ice shelf basal channels in deep-water upwelling, polynyas and ocean circulation in Pine Island Bay, Antarctica. *Annals of Glaciology*, 53(60), 123-128.

Manzella, G. M. R., Meloni, R., & Picco, P. (1999). Current, temperature and salinity observations in the Terra Nova Bay polynya area. *Oceanography of the Ross Sea Antarctica* (pp. 165-173). Springer, Milano.

Massom, R. A., Giles, A. B., Warner, R. C., Fricker, H. A., Legresy, B., Hyland, G., Lescarmontier, L.,& Young, N. (2015). External influences on the Mertz Glacier Tongue (East Antarctica) in the decade leading up to its calving in 2010. *Journal of Geophysical Research: Earth Surface*, 120(3), 490-506.

Millero, F. J. (1978). Freezing point of sea water. *Eighth report of the joint panel of oceanographic tables and standards. United Nations Educational, Scientific and Cultural Organization Techical papers in marine sciences*, 28; 29-35.

Millgate, T., Holland, P. R., Jenkins, A., & Johnson, H. L. (2013). The effect of basal channels on oceanic ice-shelf melting. *Journal of Geophysical Research: Oceans*, 118(12), 6951-6964.

Moore, J. C., Reid, A. P., & Kipfstuhl, J. (1994). Microstructure and electrical properties of marine-ice and its relationship to meteoric ice and sea ice. *Journal of Geophysical Research: Oceans*, 99(C3), 5171-5180.

Neal, A. (2004). Ground-penetrating radar and its use in sedimentology: principles, problems and progress. *Earth-Science Reviews*, 66(3-4), 261-330.

Nick, F. M., Van der Veen, C. J., Vieli, A., & Benn, D. I. (2010). A physically based calving model applied to marine outlet glaciers and implications for the glacier dynamics. *Journal of Glaciology*, 56(199), 781-794.

Nurser, A. J. G., & Bacon, S. (2014). The Rossby radius in the Arctic Ocean. *Ocean Science*, 10(6), 967-975.

Olhoeft, G. R. (1998). Electrical, magnetic and geometric properties that determine ground penetrating radar performance. *In Proceedings of GPR* , 98, 177-182.

Padman, L., Fricker, H. A., Coleman, R., Howard, S., & Erofeeva, L. (2002). A new tide model for the Antarctic ice shelves and seas. *Annals of Glaciology*, 34, 247-254.

Paolo, F. S., Fricker, H. A., & Padman, L. (2015). Volume loss from Antarctic ice shelves is accelerating. *Science*, 348(6232), 327-331.

Pearce, J., & Mittleman, D. (2002). Defining the Fresnel zone for broadband radiation. *Physical Reviews E*, 66(5), 056602.

Pollard, D., DeConto, R. M., & Alley, R. B. (2015). Potential Antarctic Ice Sheet retreat driven by hydrofracturing and ice cliff failure. *Earth and Planetary Science Letters*, 412, 112-121.

Pritchard, H. D., Ligtenberg, S. R. M., Fricker, H. A., Vaughan, D. G., Van den Broeke, M. R., & Padman, L. (2012). Antarctic ice-sheet loss driven by basal melting of ice shelves. *Nature*, 484(7395), 502-505.

Rignot, E., & Jacobs, S. S. (2002). Rapid bottom melting widespread near Antarctic ice sheet grounding lines. *Science*, 296(5575), 2020-2023.

Rignot, E., & Steffen, K. (2008). Channelized bottom melting and stability of floating ice shelves. *Geophysical Research Letters*, 35(2).

Rignot, E., Jacobs, S., Mouginot, J., & Scheuchl, B. (2013). Ice shelf melting around Antarctica. *Science*, 341(6143), 266-270.

Robinson, N. J., Williams, M. J., Stevens, C. L., Langhorne, P. J., & Haskell, T. G. (2014). Evolution of a supercooled ice shelf water plume with an actively growing subice platelet matrix. *Journal of Geophysical Research: Oceans*, 119(6), 3425-3446.

Scambos, T. A., Bohlander, J. A., Shuman, C. U., & Skvarca, P. (2004). Glacier acceleration and thinning after ice shelf collapse in the Larsen B embayment, Antarctica. *Geophysical Research Letters*, 31(18).

Scambos, T. A., Berthier, E., Haran, T., Shuman, C. A., Cook, A. J., Ligtenberg, S., & Bohlander, J. (2014). Detailed ice loss pattern in the northern Antarctic Peninsula: widespread decline driven by ice front retreats. *The Cryosphere*, 8(6), 2135-2145.

Scambos, T., M. Fahnestock, T. Moon, A. Gardner, and M. Klinger. (2016). Global Land Ice Velocity Extraction from Landsat 8 (GoLIVE), Version 1. Boulder, Colorado USA. NSIDC: *National Snow and Ice Data Center*. DOI: 10.7265/N5ZP442B.

Sergienko, O. V. (2013). Basal channels on ice shelves. *Journal of Geophysical Research: Earth Surface*, 118(3), 1342-1355.

Shepherd, A., Wingham, D., & Rignot, E. (2004). Warm ocean is eroding West Antarctic ice sheet. *Geophysical Research Letters*, 31(23). DOI: 10.1029/2004GL021106

Souchez, R., Meneghel, M., Tison, J. L., Lorrain, R., Ronveaux, D., Baroni, C., Lozej, A., Tobacco, I., & Jouzel, J. (1991). Ice composition evidence of marine-ice transfer along the bottom of a small Antarctic ice shelf. *Geophysical Research Letters*, 18(5), 849-852.

Stanton, T. P., Shaw, W. J., Truffer, M., Corr, H. F. J., Peters, L. E., Riverman, K. L., Holland., D.M., & Anandakrishnan, S. (2013). Channelized ice melting in the ocean boundary layer beneath Pine Island Glacier, Antarctica. *Science*, 341(6151), 1236-1239.

Steenson, B. O. (1951). Radar methods for the exploration of glaciers (Doctoral dissertation, California Institute of Technology, Passedena, Electrical Engineering).

Stevens, C., Lee, W. S., Fusco, G., Yun, S., Grant, B., Robinson, N., & Hwang, C. Y. (2017). The influence of the Drygalski Ice Tongue on the local ocean. *Annals of Glaciology*, 58(74), 51-59.

Taylor, J. (1997). *Introduction to error analysis, the study of uncertainties in physical measurements*. New York, New York: University Science Books.

Tison, J. L., Ronveaux, D., & Lorrain, R. D. (1993). Low salinity frazil ice generation at the base of a small Antarctic ice shelf. *Antarctic science*, 5(3), 309-322.

Tison, J. L., Khazendar, A., & Roulin, E. (2001). A two-phase approach to the simulation of the combined isotope/salinity signal of marine-ice. *Journal of Geophysical Research: Oceans*, 106(C12), 31387-31401.

Trusel, L. D., Frey, K. E., Das, S. B., Munneke, P. K., & Broeke, M. R. (2013). Satellite-based estimates of Antarctic surface meltwater fluxes. *Geophysical Research Letters*, 40(23), 6148-6153.

Trusel, L. D., Frey, K. E., Das, S. B., Karnauskas, K. B., Munneke, P. K., Van Meijgaard, E., & Van Den Broeke, M. R. (2015). Divergent trajectories of Antarctic surface melt under two twenty-first-century climate scenarios. *Nature Geoscience*. 8, 927–932

Van der Veen, C. J. (1998). Fracture mechanics approach to penetration of bottom crevasses on glaciers. *Cold Regions Science and Technology*, 27(3), 213-223.

Vaughan, D. G., Corr, H. F., Bindschadler, R. A., Dutrieux, P., Gudmundsson, G. H., Jenkins, A., Newman, T., Vornberger, P., & Wingham, D. J. (2012). Subglacial melt channels and fracture in the floating part of Pine Island Glacier, Antarctica. *Journal of Geophysical Research: Earth Surface*, 117(F3).

Waite, A. H., & Schmidt, S. J. (1962). Gross errors in height indication from pulsed radar altimeters operating over thick ice or snow. *Proceedings of the Institute of Radio Engineers*, 50(6), 1515-1520.

Weertman, J. (1973). Can a water-filled crevasse reach the bottom surface of a glacier. *International Association of Hydrological Sciences*,95, 139-145.

Weertman, J. (1974). Stability of the junction of an ice sheet and an ice shelf. *Journal of Glaciology*, 13(67), 3-11.

Williams, M. J. M., Warner, R. C., & Budd, W. F. (1998). The effects of ocean warming on melting and ocean circulation under the Amery Ice Shelf, East Antarctica. *Annals of Glaciology*, 27(1), 75-80

Williams, M. J. M., Warner, R. C., & Budd, W. F. (2002). Sensitivity of the Amery Ice Shelf, Antarctica, to changes in the climate of the Southern Ocean. *Journal of Climate*, 15(19), 2740-2757.

Woodward, J., & Burke, M. J. (2007). Applications of ground-penetrating radar to glacial and frozen materials. *Journal of Environmental and Engineering Geophysics*, 12(1), 69-85.

Young, N. W., & Hyland, G. (2002). Velocity and strain rates derived from InSAR analysis over the Amery Ice Shelf, East Antarctica. *Annals of Glaciology*, 34, 228-234.